Ultra Wideband Channel Measurement and Transmit Reference Pulse Cluster Receiver Prototype Implementation

by

Shuai He
B.Sc., Shanghai Jiao Tong University, 2007

A Dissertation Submitted in Partial Fulfillment of the
Requirements for the Degree of

MASTER OF APPLIED SCIENCE

in the Department of Electrical and Computer Engineering

University of Victoria

Ultra Wideband Channel Measurement and Transmit Reference Pulse Cluster Receiver Prototype Implementation

by

Shuai He
B.Sc., Shanghai Jiao Tong University, 2007

Supervisory Committee

Dr. Xiaodai Dong, Supervisor
(Department of Electrical and Computer Engineering)

Dr. Michael McGuire, Member
(Department of Electrical and Computer Engineering)

Supervisory Committee

Dr. Xiaodai Dong, Supervisor
(Department of Electrical and Computer Engineering)

Dr. Michael McGuire, Member
(Department of Electrical and Computer Engineering)

ABSTRACT

Ultra wideband (UWB) systems have the potential for extremely high data rate transmission, accurate ranging and positioning. In order to build systems that realize all the potential of UWB, it is first required to understand UWB propagation and the channel properties arising from the propagation. One of the key objectives of this thesis is to explore the characteristics of the UWB indoor channel. Through extensive time domain measurement, the channel reciprocity, spatial correlation, body shadow effect and temporal variation are investigated. Firstly, the existence of channel reciprocity is verified in both baseband and bandpass channels (from 4 GHz to 8 GHz), and channel reciprocity is demonstrated to be frequency independent and distance independent. Secondly, the spatial correlation is investigated on a two dimensional grid, and has been found to follow the trend of a two dimensional Bessel function as spatial distance increases. Thirdly, the interference of the received power and RMS delay spread due to body shadow effect is studied, indicating that the UWB system is highly robust to body shadowing as compared to narrowband systems. Finally, extensive measurements of the UWB channel's temporal variation in a modern office building under diversified sets of conditions are conducted. A real time measurement is highly robust to body shadowing as compared to narrowband systems. Finally, extensive measurements of the UWB channel's temporal variation in a modern office building under diversified sets of conditions are conducted. A real time measurement campaign involving mobile scatterers was performed in a typical office environment, hallway environment and lobby environment, to investigate the signal strength fluctuation, temporal correlation and Doppler spread. The analysis of the measurement results provide useful information for UWB system design, transceiver implementation and performance evaluation. The other goal of the thesis is to demonstrate the implementation of the transmitted reference pulse cluster (TRPC) receiver prototype. This prototype modulates data with binary phase shift keyed pulses, communicates over a wireless link using UWB antennas and a wideband direct conversion front-end, and samples the auto-correlation output of the received signal for demodulation. Commercial off the shelf components are used to build the receiver, and design considerations are introduced for each part of the receiver in detail.

Contents

List of Tables

List of Figures

ACKNOWLEDGEMENTS

I would like to express my deepest gratitude to my supervisor, Dr. Xiaodai Dong for her ample support, immense knowledge, strong motivation and valuable guidance. I could not have imagined having a better advisor and mentor for my graduate study.

Besides my advisor, I would like to thank the rest of my thesis committee, Dr. Michael McGuire and Dr. Jianping Pan, for their encouragement and insightful comments.

I would give my sincere thanks to Ted, Yuzhe, Zhonghua, Lebing, Zhuangzhuang, Ruonan and all the other colleagues in our group for their valuable discussion and priceless help.

I also wish to thank Nichao, Weixiao, Shiyu, Lidong and Zewei, who bring so much fun and warm help, and make my life rich and colorful.

Special thanks to Moneca, Vicky, Paul, Lynne, Mary-Anne and Monique, for the constant help from them.

Last and the most important, I would appreciate my family, especially my parents, for their priceless care and love, for their endless support and for their invaluable encouragement. My loving thanks to my wife, for her tender love and care.

He Shuai

DEDICATION

To my beloved wife Ren Puxian and my parents.

Chapter 1

Introduction

According to the Federal Communications Commission (FCC) and Industry Canada, any wireless communication technology that produces signals with a bandwidth wider than 500 MHz or a fractional bandwidth greater than 0.2 is considered as ultra wideband (UWB). UWB communication systems have an unprecedented opportunity to impact communication systems. The enormous bandwidth available, the potential for high data rates, small size and low processing power along with low implementation cost all present a unique opportunity for UWB to become a widely adopted radio solution for short range communication systems [1].

In this chapter, a brief overview of the UWB technology is first presented, followed by two important issues: UWB channel modeling and UWB receiver design. The UWB channel is significantly different from the narrowband wireless channels in terms of the time resolution and fading statistics. Moreover, as with any other communications system, it is the channel that determines the ultimate (information capacity) performance limits, as well as the practical receiver structure. Therefore, a brief overview of the UWB channel modeling is presented in Section 1.2. In Section 1.3, the fundamentals of the UWB receiver designs are described. Both Coherent and non-coherent receiver structures are addressed, and the low complexity transmitted reference receiver scheme is highlighted. Finally, the organization of this thesis is explained at the end of the chapter.

1.1 Brief Overview of Ultra Wideband Communication

The most distinctive feature of the UWB system is the large absolute bandwidth, which in accordance with the FCC definition is more than 500 MHz. Such large absolute bandwidth can provide a large spreading factor which is defined as the ratio of the signal bandwidth to the symbol rate. In low data rate applications, the spreading factor can reach as high as 10^4 to 10^6. Such large spreading factor results in a very small power spectral density which is necessary to meet the FCC limits on the transmission power. The FCC regulation limits the radiation power of indoor communication UWB systems to less than -41.3 dBm/MHz within 3.1-10.6 GHz [2], while the newly published Canadian UWB regulation limits the equivalent isotropically radiated power (EIRP) to -70 dBm/MHz in the frequency range of 1.61-4.75 GHz and -41.3 dBm/MHz from 4.75 GHz to 10.6 GHz [3]. Such strict restrictions avoid interference to legacy (narrowband) systems. Operating under these regulation will not disturb the narrowband system at all and can assure the narrowband systems work properly. Besides that, the large absolute bandwidth makes UWB signals similar to noise, which makes them difficult to intercept [4].

Another distinctive feature of UWB is the employment of ultra short pulses. Suppose a narrowband system has a throughput of 1 Mbps bit rate, then the signal width is approximately 1000 ns. To differentiate the multipath in such situation, the length difference between the two paths should be more than 1000 ns $\times 3 \times 10^8 = 300$ m.

On the other hand, a typical UWB system has a pulse width of about 1 ns, thus the multipath can be distinguished if the two path difference is only more than 1 ns $\times 3 \times 10^8 = 0.3$ m. As a result, the UWB system has a high resistance to fading. In conventional narrowband systems, the received signal strength undergoes fluctuations, caused by multipath components (MPC), i.e., echoes from different scatters and reflectors and signals caused by diffractions, which interfere with each other constructively or destructively, depending on the exact location of transmitter, receiver and scatters [5]. A UWB transceiver receives a signal with a large absolute bandwidth, and can thus resolve many of those MPCs. The receiver can make sure that all those components add up in an optimum manner, giving rise to a smaller probability of deep fades. A simulated IEEE 802.15.3a indoor UWB channel realization is shown in Fig. 1.1. From Fig. 1.1, we could observe that almost every single multipath can be resolved due to the narrow pulses used.

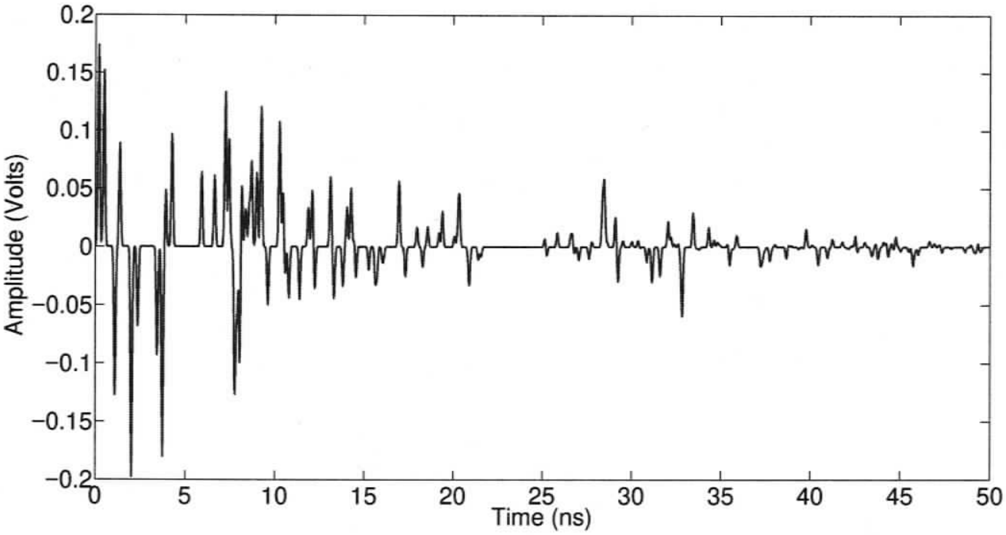

Figure 1.1: A realization of IEEE 802.15.3a channel model.

One of the most important benefits of the UWB communication system is the ability of pulses to easily penetrate walls, doors, partitions, and other objects in the home and office environment. Lower frequency radio waves are able to pass through walls, doors, and windows because the wavelength is much longer than the physical dimensions of the material that it is passing through. On the other hand, higher frequency waves will have more of their energy reflected from walls and doors since the wavelength is much shorter. UWB pulses are composed of a large range of frequencies. Thus, the low-frequency components can more easily penetrate walls, while the high-frequency components give strongly reflected signals.

Although a UWB signal has a number of advantages, it also gives rise to challenges. From a hardware point of view, the accuracy of the local oscillators and timing circuits must be very high. When the absolute bandwidth is 1 GHz, a timing jitter of 1 ns can have catastrophic consequences. Another consequence of the high time resolution is that a large number of components need to be received and processed. For example, the number of fingers in a Rake receiver required to collect 90 % of the available energy can easily reach several tens or even hundreds [6].

1.2 UWB Channel Modeling

A realistic radio channel model that provides insight into the radio wave propagation mechanisms is essential for the system simulation and successful deployment of wireless systems. If an accurate channel model is available, it is possible to design receiver (Rx) algorithms that achieve good performance by exploiting the properties of the channel. Therefore, a good understanding of the propagation mechanisms and effects is the key subject for the development of a realistic channel model.

The type of channel model that is desired depends critically on the carrier frequency, bandwidth, the type of environment, and the system under consideration. For example, different types of channel models are needed for indoor and outdoor environments, and for narrowband, wideband and UWB systems. The UWB channel modeling has been the subject of extensive research in recent years [7, 8, 9, 10]. Several new standards are developed for UWB technology such as IEEE 802.15.3a and IEEE 802.15.4a. The former standard is capable of providing high data rate for short-range applications (i.e., up to 110 Mbps at 10 m and 480 Mbps at shorter distances), while the latter standard aims to provide low data rate for longer range applications (i.e., approximately 1 Mbps at up to 30 m) with high-precision ranging and location capability [11, 12]. The emergence of UWB technology for both short-range high-rate and long-range low-rate communication systems implies that understanding the characteristics of the UWB propagation channel is essential. Given the wideband nature of UWB signals (i.e., up to tens of GHz of frequency bandwidth), the conventional channel models developed for narrowband transmissions are inadequate for UWB transmission. This implies that more UWB channel measurements are required in order to gain profound knowledge of the UWB channel behaviors.

In a wireless system, the transmitted signal interacts with the physical environment in a complex manner. The signal arriving at the Rx is, in general, a summation of both direct LOS and several multipath components (MPCs). Multipath occurs due to the three basic multipath propagation mechanisms, namely, reflection, diffraction, and scattering of the transmitted signal. All three of these phenomena cause radio signal distortions and give rise to signal fades, as well as additional signal propagation losses in a wireless communication system. The relative importance of these propagation mechanisms depends on the particular environment.

One of the most important aspects of the wireless channel is fading, which refers to the fluctuation in the envelope of a transmitted radio signal. The UWB channel can be modeled by large scale fading, medium scale fading or shadowing and small scale fading. The definition of the three fading types are:

1. Large scale fading: averaged over time and a sufficiently large spatial area, the gradual loss of the received signal power with transmitter-receiver separation distance is referred to as large scale fading.

2. Medium scale fading or shadowing: the random variation of the signal due to the peculiarities of the particular environment surrounding the transmitter and the receiver. Shadowing happens at a shorter time scale compared to large scale fading, but longer than small scale fading.

3. Small scale fading: the signal fluctuates over very small distances which is in the order of several wavelength, due to constructive or destructive superposition of the unresolvable multipath.

For compliance with the traditional pathloss analysis, the pathloss coefficient can be expressed as [6]

$$L(d) = \int \overline{L}(d) \cdot \overline{L}(f) d(f/f_0) \tag{1.1}$$

where f_0 is the reference frequency. Eq.(1.1) suggests the pathloss is dependent on the distance d and the frequency f. The distance dependent pathloss can be written as [6]

$$\overline{L}(d) \propto -10n \cdot \log_{10}(\frac{d}{d_0}) \tag{1.2}$$

where d_0 is the reference distance, and the path loss coefficient, n, depends on the communication environment. Typical values of n are 2 for free space transmission, 2.7-3.5 for urban area cellular radio and 1.6-1.8 for in building line of sight transmission.

Due to the fact that diffraction, material penetration and other effects are frequency dependent, the pathloss exponent could change with frequency. Analytically, the frequency dependence of UWB propagation channel has been observed to obey in dB [13]:

$$\overline{L}(f) \propto -20\chi \cdot \log_{10}(\frac{f}{f_0}) \tag{1.3}$$

where f_0 is the reference frequency and χ is the frequency decay coefficient.

The random variation of the received power averaged over a small spatial area is referred to as shadowing and denoted by S, which accounts for signal strength loss due to absorption or blockage by the local surrounding media. It is a random effect between the pathloss behavior and small-scale fading. Excluding small-scale fading, the total loss in power due to pathloss and shadowing can be expressed in dB as

$$PL(d) = [L(d_0) - 10n \log_{10} \frac{d}{d_0}] + S \tag{1.4}$$

where $L(d_0)$ is the average pathloss in dB at reference location d_0.

While the statistical properties of the large-scale characteristics are necessary for proper link budget design, the statistical properties of the small-scale characteristics are needed for efficient receiver design. Specifically, understanding small-scale fading and signal correlation over a small area aids in the evaluation of the receiver, multiple access technique and multiple antenna applications.

The main goal of small-scale channel models is to statistically characterize the amplitudes, delays and polarities of the multipath components of the channel. The impulse response (in complex baseband) of the SV (Saleh-Valenzuela) model is given by [14]

$$h(t) = \sum_{l=1}^{L} \sum_{k=1}^{K} \alpha_{k,l} \exp(j\phi_{k,l}) \delta(t - T_l - \tau_{k,l}) \tag{1.5}$$

where T_l denotes the delay of the l^{th} cluster, $\tau_{k,l}$ denotes the delay of the k^{th} channel tap of the l^{th} cluster relative to T_l, $\alpha_{k,l}$ and $\phi_{k,l}$ denote the magnitude and phase of the k^{th} channel tap in the l^{th} cluster, respectively. The total number of clusters in the channel power delay profile (PDP) L is a random variable follows a Poisson distribution. That is

$$prob(L = l) = \frac{\bar{L}^l \exp(-\bar{L})}{l!} \tag{1.6}$$

where $\bar{L}$ is the expectation of L. The cluster arrival time T_l is defined as a Poisson process, i.e., the time difference of adjacent clusters follows exponential distribution, which can be written as

$$p(T_l|T_{l-1}) = \Lambda \exp[-\Lambda(T_l - T_{l-1})], \quad l > 0, \tag{1.7}$$

where Λ is the cluster arrival rate. On the other hand, the channel bin arrival time $\tau_{k,l}$ is defined as the mixture of two Poisson processes, which is

$$p(\tau_{k,l}|\tau_{(k-l),l}) = \beta\lambda_1 \exp[-\lambda_1(\tau_{k,l} - \tau_{k-1,l})] + (1-\beta)\lambda_2 \exp[-\lambda_2(\tau_{k,l} - \tau_{k-1,l})], \quad k > 0 \tag{1.8}$$

where β is called the mixture probability whose value varies over different channel environments, λ_1 and λ_2 are the ray arrival rates.

The tap gain $\alpha_{k,l}$ follows Nakagami distribution. Its probability density function can be written as

$$p_{\alpha_{k,l}}(\alpha) = \frac{2}{\Gamma(m)}\Big(\frac{m}{\Omega_{k,l}}\Big)^m \alpha^{2m-1} \exp\Big(-\frac{m}{\Omega_{k,l}}\alpha^2\Big) \tag{1.9}$$

where $m \leq 1/2$ is the Nakagami factor, $\Gamma(m)$ is Gamma function and Ω is the mean square value of α. The Nakagami factor is modeled as a log-normal distributed random variable whose logarithm has a mean m_0 and standard deviation $\hat{m}_0$. The mean power of the channel taps $\Omega_{k,l}$ follows the exponential function in each cluster.

That is,

$$\Omega_{k,l} = \frac{\Omega_l \exp(-\tau_{k,l}/\gamma_l)}{\gamma_l[(1-\beta)\lambda_1 + \beta\lambda_2 + 1]} \tag{1.10}$$

where γ_l is the intra-cluster decay time constant which is linearly dependant on the cluster arrival time, and Ω_l denotes the total channel tap power within the l^{th} cluster.

Besides specific statistical characterization of the multipath parameters, the channel can also be characterized by coarse statistics such as mean excess delay and RMS delay spread that describe the time-dispersive properties of the channel. These are useful as single-number descriptions of the channel to estimate the performance and potential for inter-symbol interference. The mean excess delay of the channel $h(\tau)$ is defined as

$$\tau_m = \frac{\sum_k \beta_k^2 \tau_k}{\sum_k \beta_k^2} \tag{1.11}$$

and the RMS delay spread of $h(\tau)$ is defined as

$$\tau_{RMS} = \sqrt{\frac{\sum_k \beta_k^2 \tau_k^2}{\sum_k \beta_k^2} - \tau_m^2} \tag{1.12}$$

1.3 The UWB Receiver Design

High capacity, high data rate, simple, power efficient, and low cost UWB transceiver design is a challenging task. Due to the fine time resolution of the UWB signals, the received waveform contains tens or hundreds of resolvable multipaths. Moreover, given the total constant transmitted power, the power in each of these multipath components will be very low. Therefore, capturing the energy of each resolvable MPC is extremely difficult. Generally, there are two different kinds of receiver schemes, namely, coherent and noncoherent receiver. Fully coherent receivers like optimal matched filtering, typically employed by rake reception, perform well but at the expense of extremely high computational and hardware complexity. In general, the coherent receiver requires the knowledge of the channel state information (CSI), such as the amplitude, phase and delay of each MPC, the distortion of the pulse shape, and the delay spread of the channel. However, the estimation of the CSI is exceedingly difficult and complicated. In order to capture a considerable portion of the signal energy scattered in the MPC, the receiver should be able to sample at a minimum of hundreds of MHz to even several GHz samples per second, or requires an impractically large number of Rake fingers. Because of these issues, the fully coherent receiver design can become rather difficult, and, if care is not taken, fully coherent reception might lead to very poor overall system design. Therefore, receivers that relax these requirements are preferable.

As an alternative, noncoherent (or lightly coherent) receiver designs in UWB relax the amount of information that needs to be estimated accurately for the detection of the transmitted bits. Some of the noncoherent receiver designs include the transmitted reference (TR) based detector, energy detector, and differential detector. These techniques do not require channel estimation and pulse shape estimation, and allow capture of a large amount of the received energy. Besides, their timing estimation is easier and these receivers' performance are more immune to timing mismatch [15]. They represent, however, sub-optimal solutions, compared to fully coherent receivers, because of the adoption of noisy signals as reference waveforms for the demodulation process.

A generic UWB receiver structure is shown in Fig. 1.2. Depending on the implementation, the received signal can be sampled in various places. Two possible sampling points, before the multiplier and after the integrator, are shown in the figure. Sampling after the integrator allows a low sampling rate with analog front end circuitry. Sampling before the multiplier allows all digital, flexible, and is used in software-defined radio receiver designs [16].

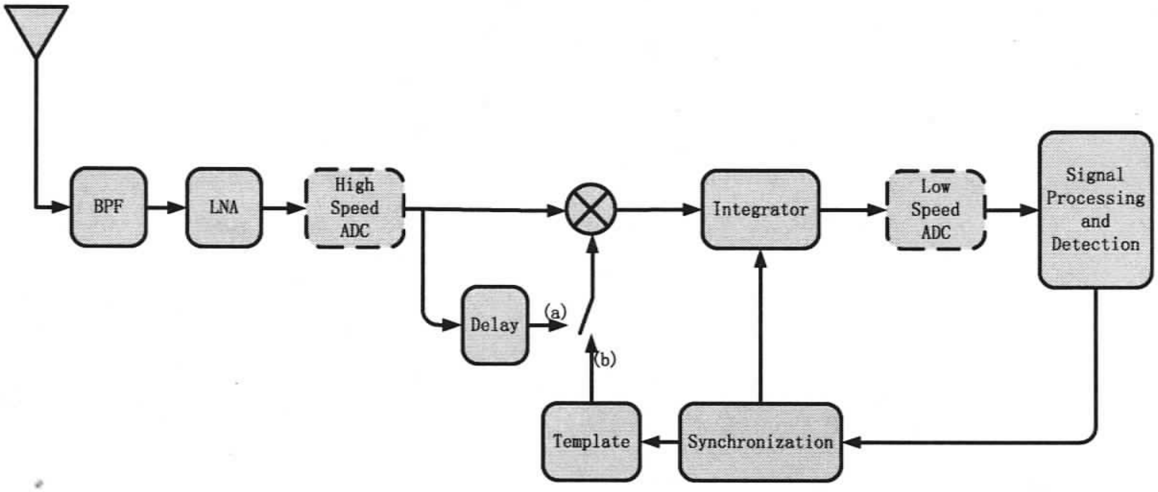

Figure 1.2: (a) Non-coherent receiver structure (b) Coherent receiver structure [15]

In the coherent receiver structure, the received signal is synchronously correlated with a local template, which is estimated based on the received signal by transmitting some data aided or non-data aided sequences. The coherent receiver structure is shown in Fig. 1.2(b). Alternatively, the received signal could correlate with itself or some reference template, which leads to the noncoherent receiver structure, as shown in Fig. 1.2(a). If the delay is zero, this will end up being an energy detector, where the multiplier can be used as a square device. While if the delay is the time difference between two consecutive differential coded symbols, it turns out to be a differential detector. Finally, if the delay is the time difference between the reference and data-bearing signals, it can be regarded as the TR detector. This thesis will focus on the TR based receiver implementation given in Chapter 4.

1.3.1 Transmitted Reference Receiver

The interest in the TR scheme in UWB transceiver design has grown recently. Hoctor and Tomlinson first proposed a UWB TR system with a simple receiver structure to capture all of the energy available in a UWB multipath channel [17]. The principle in the TR UWB scheme is to transmit a reference waveform before each data-modulated waveform for the purpose of determining the current multipath channel response. It should be noted that the delay between the reference waveform and data-modulated waveform should be less than the channel coherence time in order to assure the reference and data-bearing waveform are subject to the same channel response. Therefore, the receiver correlates the data signal with the reference to use all the energy of the data signal without requiring additional channel estimation and Rake reception. Thus, in an environment with sufficiently high and dense multipaths, the TR scheme can capture more energy than a selective RAKE receiver, while in sparse channels and in channels that have few multipaths, the conventional TR-based schemes are less desirable compared with the high-performance RAKE and correlator receivers. As a result, TR communication possesses some advantages when transmitting through an unknown channel, which severely distorts the transmitted waveforms. The UWB TR receiver structure is shown in Fig. 1.3.

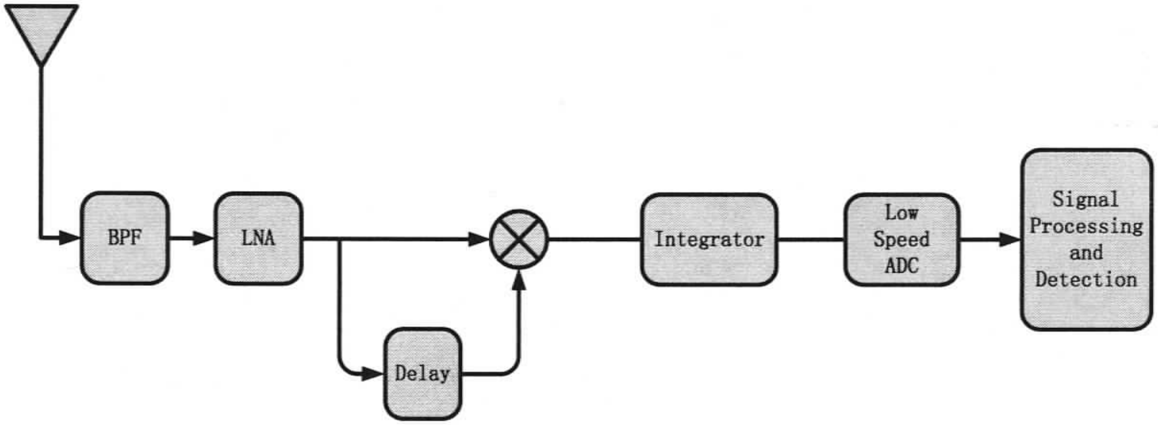

Figure 1.3: UWB TR receiver structure

Compared to the fully coherent receivers, the TR scheme is able to capture the energy from all multipath components of the received signal with a simple receiver structure. However, this simple receiver structure has one major drawback, namely the transmitted reference signal used as a correlator template is noisy. Therefore, the bit error rate (BER) performance of the coherent receiver outperforms the noncoherent TR scheme. This problem can be avoided by averaging the reference pulses to obtain a clean template. However, averaging using analog circuitry is not a straightforward task, since there is no way to store an analog waveform for post processing. Although multiple delay lines can be used to achieve the task, the attenuation of different length of delay lines is distinct. In addition, for low data rate applications, the long delay lines are hard to achieve physically. Moreover, during the averaging over multiple reference pulses, the channel variation should be taken into account unless the channel is time-invariant over these reference pulses.

Even though the TR scheme is often considered as a noncoherent scheme that avoids the estimation of pulse shape and other channel parameters, one can also interpret it as a semi-coherent scheme where the reference pulses are used to estimate the channel parameters. The delay, amplitude, and even the pulse shape of each resolvable multipath of the template is identical with the data-bearing received symbols. Essentially, the channel is estimated using these reference pulses.

One of the most striking features of the TR scheme is that the timing requirement is less stringent compared with a local correlator receiver. Note that the local template type of receivers try to match the timing of the received pulse exactly with the template. However, in the TR scheme, there is no need for a fine timing estimate of all the multipath components. This has both advantages and disadvantages. The advantage is simpler timing and more immunity to timing errors. The disadvantage is that, without the fine timing of each individual multipath, both the noise and signal over a window (whether there is a multipath component or not) are included in the non-ideal noisy template. This is one of the reasons why TR schemes do not provide good performance, as more noise than an ideal matched filtering is received. In essence, the TR scheme assumes that everything is useful over the integration window.

In reality, some samples contain energy, and some contain noise. If one integrates all of them, than the integrator is not collecting the energies optimally. One way to solve this problem is to control the integrator. If the locations of multipath components are known, then the energies only from these received samples where the multipath components are located need to be collected. Then, this will end up being a RAKE reception. As a result, one can make a TR scheme work as well as a RAKE receiver if additional parameters about the channel are known [16].

1.4 Agenda

This thesis mainly focuses on indoor UWB channel measurement and the implementation of the TRPC receiver prototype. Based on comprehensive indoor measurements, channel reciprocity, spatial characteristic, body shadow effect and temporal variation of the UWB channel are investigated. In addition, a detailed description of the procedure to implement the TRPC receiver prototype is also presented.

Chapter 2 describes three very important characteristics of the UWB indoor channel, that is, the channel reciprocity, spatial characteristics and body shadow effects. A time domain measurement scheme that employs an arbitrary waveform generator and a pulse generator is used to perform comprehensive measurements in different environments. The channel reciprocity is first addressed, and is verified to exist in UWB channels. The spatial correlation is then analyzed, and the trend of the correlation coefficient turns to follow a two dimensional Bessel function when the antenna array spacing increases. Finally, the effect of body shadowing is investigated in order to estimate its effect on the system's link budget and its influence towards the CIR.

Chapter 3 focuses on the study of temporal variations of the UWB channels. Due to people's movement, the channel impulse response may change over time in the form of appearing or disappearing multipaths, disturbing the pulse shape, changing the multipath strength and extending or shortening of the delay spread. These effects will certainly influence the signal strength, time correlation, RMS delay and Doppler spread. Therefore, in this chapter, all of these effects are taken into consideration, and are analyzed.

Chapter 4 gives a detailed description of the implementation of the UWB transmitted reference pulse cluster (TRPC) receiver prototype. The system model of the TRPC scheme is first presented. Then based on the unique structure of the TRPC scheme, a system level prototype of the TRPC receiver is implemented. This prototype makes use of the BPSK modulation scheme, providing a data rate from 1 Mbps to 4 Mbps.

Chapter 5 concludes the thesis and suggests future research topics.

Chapter 2

The Temporal and Spatial Characteristics of the Ultra Wideband Channel

The UWB propagation channel can have a significant impact on system design and performance evaluation. In an indoor environment, the UWB system suffers from very severe multipath effect, but fortunately, due to the intrinsic capability of high temporal resolution of UWB impulse, almost every single path arriving at the Rx at a certain delay bin can be resolved. This implies that multipath arrivals will undergo less fading compared to the conventional narrowband system. Although UWB channel measurements have been performed and parameters such as path loss, delay spread, small scale fading, cluster and ray arrivals, etc., have been characterized in a large number of articals [7]-[10] (and the references therein), empirical evaluation is still lacking for application-oriented characterization, e.g., reciprocity, spatial correlation, and body shadow effect (BSE). Ultimately, these propagation characteristics of UWB signals will have a significant impact on the application-oriented UWB system design.

2.1 Channel Measurement Scenario and Setup

We deploy two different measurement setups for the work herein, one with the arbitrary waveform generator (AWG) and the other with a pulse generator. For the AWG setup, a baseband pulse is generated by Tektronix AWG7052 and then output to the Agilent E8267D vector signal generator (VSG) for RF modulation at a variable carrier frequency within $3-10$ GHz. Both the Tx and Rx use Electrometric EM-6865 biconical, omni-directional antennas with vertical polarization. At the receiver side, the received signal is first amplified by a low-noise-amplifier before being sampled by the Agilent 81004A high speed digital sampling oscilloscope (DSO). Pulse generator based setup is identical to the AWG based setup, except that the Tx side employs a pulse generator. For the better understanding of the UWB channel characteristics, two pulse generators with different center frequencies and bandwidth are used: a Hyberlabs HL9200 and a Avtech AVE2 pulse generator. The HL9200 pulse generator has a 3 dB bandwidth from 380 MHz to 4 GHz and center frequency (the peak frequency component) of 1.2 GHz, while AVE2 has a bandwidth of 4 GHz and centered at 5 GHz. The overall setup is synchronized by the AWG trigger output. Both the AWG and pulse generator based setups are shown in Fig. 2.1.

Over 64 measurements are averaged by the DSO prior to signal processing offline. To collect a large amount of data and eliminate the operator's presence in the propagation environment, we use the general purpose interface bus (GPIB) for remote control.

All the measurements were conducted in the Wireless and Networking Research Laboratory at the University of Victoria. The layout of the measurement environment is shown in Fig. 2.2. The lab is made out of general construction materials such as glass, metal, wood and concrete. As shown in Fig. 2.2, we perform the measurement in a variety of scenarios, including both line-of-sight (LOS) and non-line-of-sight (NLOS)

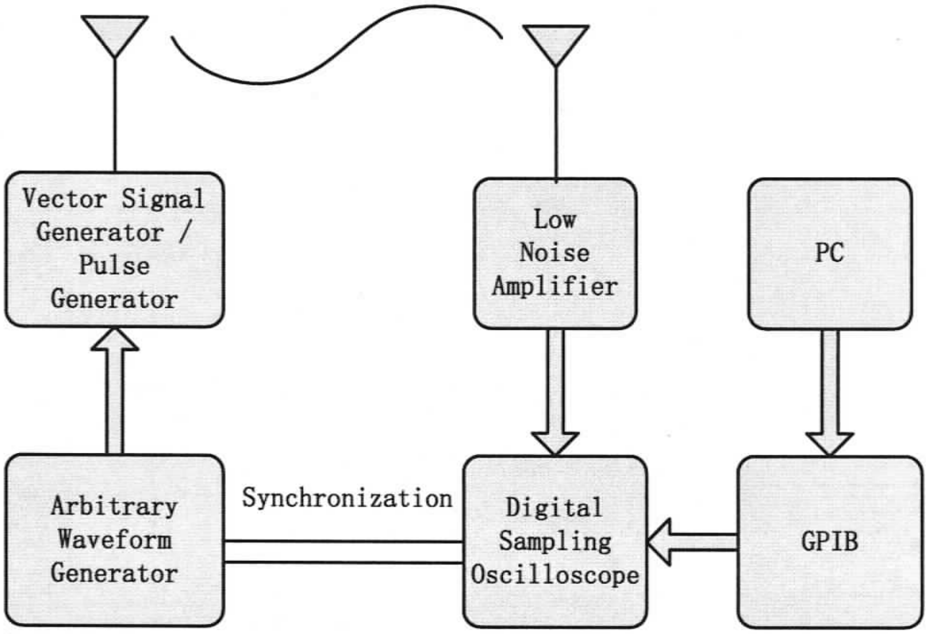

Figure 2.1: The AWG and pulse generator based setup.

propagation.

2.2 Ultra Wideband Reciprocity and Time Reversal

2.2.1 Ultra Wideband Reciprocity

The channel reciprocity, or a more intuitive name, channel symmetry, is a property that demonstrates how similar is the CIR of the forward link and the reverse link. The channel reciprocity is of great importance for reducing the complexity of the UWB receiver. In this section, some initial reciprocity verification has been obtained using the time domain UWB radio pulses.

The UWB indoor channel reciprocity measurement is conducted with Scenarios 1 to Scenarios 4. Both the pulse generator and AWG based setups are employed

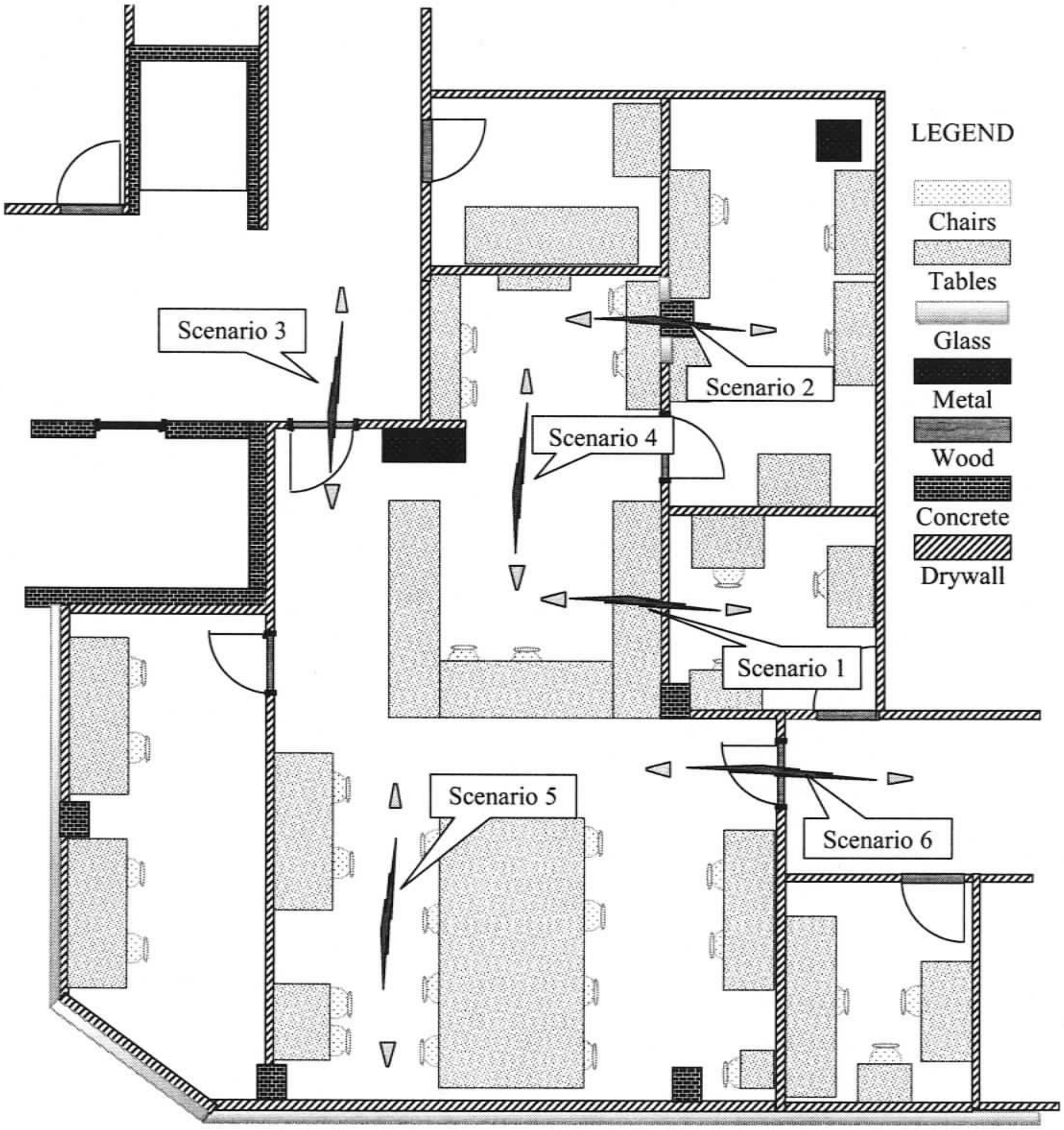

Figure 2.2: The channel measurement scenarios layout.

for baseband and RF reciprocity measurement respectively. For AWG based setup, a 2 ns root raised cosine signal with a roll-off factor of 0.25 is used, and the center frequency set by VSG is varied from 4 GHz to 8 GHz, in order to evaluate the frequency dependency of the reciprocity. The reciprocity measurement is performed by exchanging the function of the Tx and Rx antennas, i.e., keep the antenna stable, and switch the Tx cable and the Rx cables. An empirical measurement result is shown in Fig. 2.3, which clearly shows that the forward link and the reverse link are almost identical, and verifies the existence of the reciprocity in UWB indoor channels.

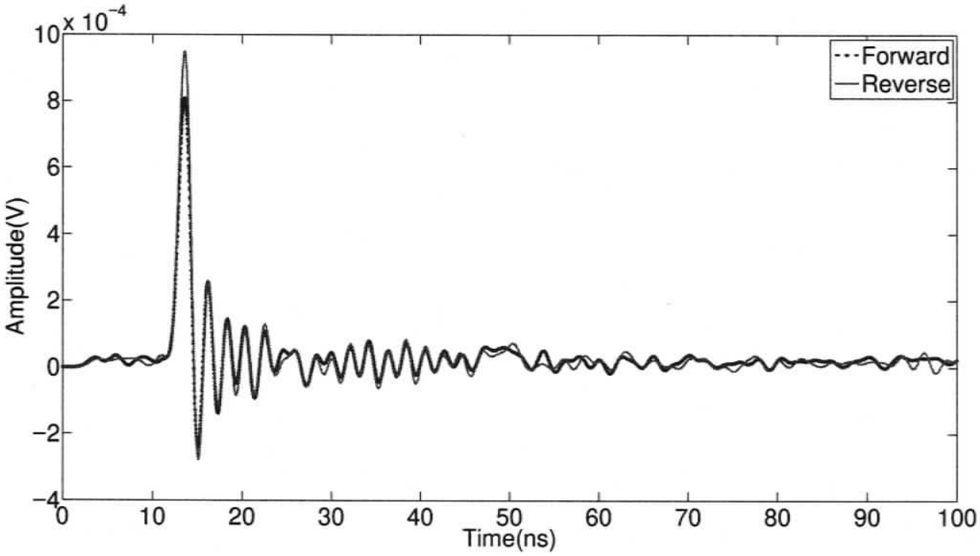

Figure 2.3: The forward and the reverse link of the channel.

To efficiently evaluate the similarity between the forward link and the reverse link, a correlation coefficient is defined as

$$\mu_{rec} = \frac{\int r_1(t) r_2(t) dt}{\sqrt{\int r_1^2(t) dt}\sqrt{\int r_2^2(t) dt}} \tag{2.1}$$

where $r_1(t)$ and $r_1(t)$ are the received signal from the forward link and reverse link respectively. Since the radio channel we have measured is wide sense stationary, the statistical average can be simplified by time average, and the time average is achieved by using the averaging function of the DSO.

Table 2.1 indicates the reciprocity of baseband UWB channels under four different scenarios. As it appears from the table, all of the correlation coefficients are larger than 95%, indicating the highly correlated forward link and reverse link. Fig. 2.4 and Fig. 2.5 demonstrate the UWB channel reciprocity with a carrier under both LOS and NLOS environments respectively. Although the carrier frequency is shifted

Table 2.1: The reciprocity of baseband UWB channels

	Distance	LOS/NLOS	Correlation
Scenario 1	3.5 m	NLOS	0.9615
Scenario 2	3 m	NLOS	0.9766
Scenario 3	3 m	NLOS	0.9817
Scenario 4	5 m	LOS	0.9887

from 4 GHz to 8 GHz and the distance is increased from 2 meters to 8 meters, the forward and reverse links are always highly correlated, indicating the forward and reverse channel are symmetrical. The correlation coefficient is not 1, due to DSO's internal jittering and interference from other communication systems and noise.

All the measurement results demonstrate that the reciprocity exists in the baseband and RF passband, LOS and NLOS indoor UWB channels, and more importantly, it appears to be distance independent and frequency independent. With the confirmed UWB channel reciprocity, the complexity of the receiver side can be shifted to the transmitter side by using a time reversal technique, which can simplify the design of UWB receiver and hence extend the sensor nodes' or mobile terminals' battery endurance.

2.2.2 Time Reversal

As mentioned before, the most important application of the channel reciprocity is time reversal. Time reversal [18] has been studied for many years. It was initially investigated in the field of acoustics and more recently in the field of electromagnetics. Time-reversal is a technique to focus spatially and compress temporally broadband signals in rich scattering environments. In a time reversal scheme, the time-reversed complex conjugate of the channel impulse response (CIR) of any transmit-receive link is used as a prefilter at the transmitter. The time-reversed waves back propagate in the channel by retracing their paths and focus in space and time at the source, the

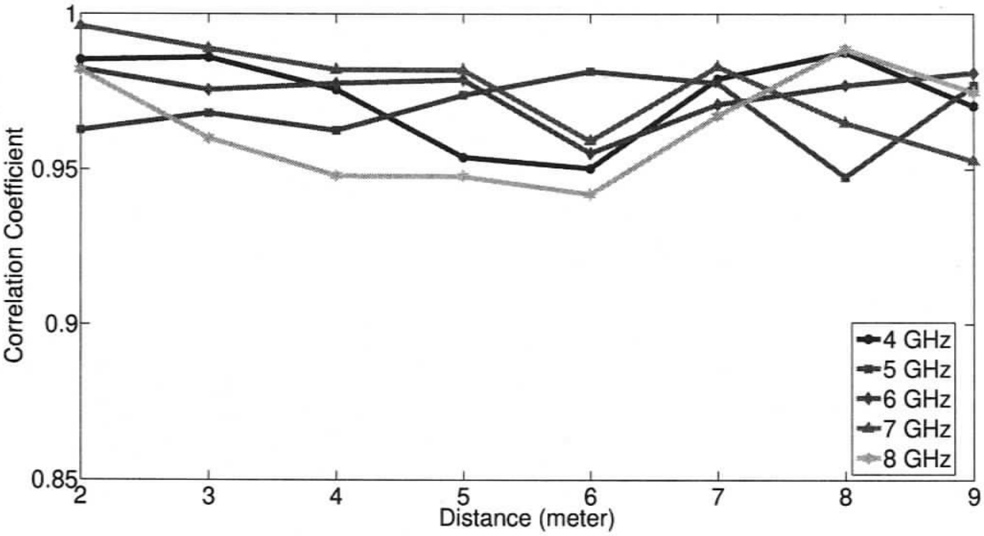

Figure 2.4: The reciprocity of the LOS UWB channel

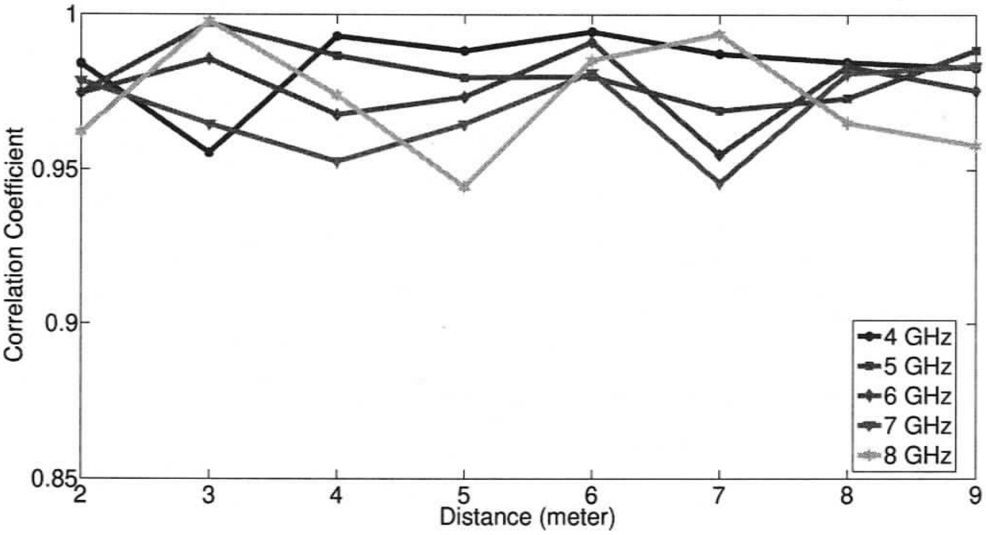

Figure 2.5: The reciprocity of the NLOS UWB channel

intended receiver [19].

Several advantages come with this technique. Due to the temporal focusing, the effective delay spread of the channel is dramatically reduced and thus intersymbol interference (ISI) is also reduced dramatically. This leads to a potential higher data rate as well as a reduction in the equalization task at the receiver by reducing the effective channel length. Due to the same reason, the complex task of estimating a large number of taps at the receiver is also greatly reduced, which implies low cost low complexity receivers. Furthermore, due to the considerable focusing gain, better signal to noise ratio or equally higher data rate can be achieved. It is also possible to increase the communication range by keeping FCC spectral mask limit for UWB communication. Due to spatial focusing, the co-channel interference in a multi-cell system is reduced. This implies a low probability of intercept by another receiver located nearby.

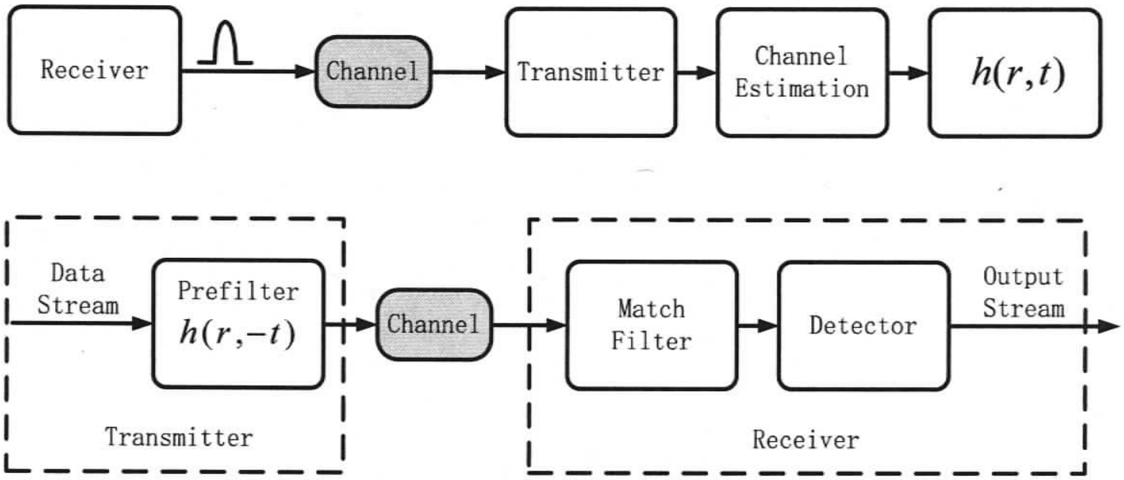

Figure 2.6: The time reversal system architecture.

In a time reversal scheme, the intended receiver sends a training sequence or a narrow pulse to the transmitter. The transmitter time-reverses the estimated CIR, convolves it with the signal message that is now sent to the receiver. The emitted time reversed waves propagates through the channel retracing their former paths and this leads to a focus of power in space and time at the receiver.

2.3 Ultra Wideband Spatial Characteristic

Multiple-input multiple-output (MIMO) technology, exploiting physical or virtual antenna arrays, has the potential to substantially enhance the data-rates achievable by UWB [20], catering to high-end applications such as wireless multimedia transmission or sensor networks with high spatial density. An understanding of the UWB spatial channel, and its correlation characteristics in particular, is thus of paramount importance for future UWB wireless communications.

Traditionally, multiple antennas have been used to increase diversity to combat channel fading. Each pair of transmit and receive antennas provides a signal channel path from the transmitter to the receiver. By sending signals that carry the same information through different paths, multiple independently faded replicas of the data symbol can be obtained at the receiver end, and proper combining algorithms could be applied for optimal reception. Therefore, more reliable connection is achieved.

Multiple antennas can also be used to increase the channel capacity. Essentially, if the channel path between individual transmit-receive antenna pairs fade independently, the channel matrix is well conditioned with high probability, in which case multiple parallel spatial channels are created. By transmitting independent information streams in parallel through the spatial channels, the data rate can be increased. This effect is also called spatial multiplexing [21].

The spatial correlation in the multipath channel is a critical factor in the performance of a MIMO system. The fading correlation between the array elements should be sufficiently low for a MIMO system to offer any performance enhancement [22]. High correlation between multiple signal streams can reduce the channel matrix rank; a perfectly correlated channel has unit rank with a single effective degree of freedom. Any potential diversity or spatial multiplexing advantage is then lost, and the performance reduces to that of a single-input single-output (SISO) system. The spatial correlation can also provide information on how frequently the channel estimation should be performed with the change of spatial position.

The correlation properties of narrowband MIMO channels are well understood. From Jake's model, in a Rayleigh fading channel with rich, isotropic scattering, the envelope correlation, ρ, is related to the antenna spacing, d, and carrier, f, through a zeroth order Bessel function of the first kind shown in Fig. 2.7, i.e. [23]

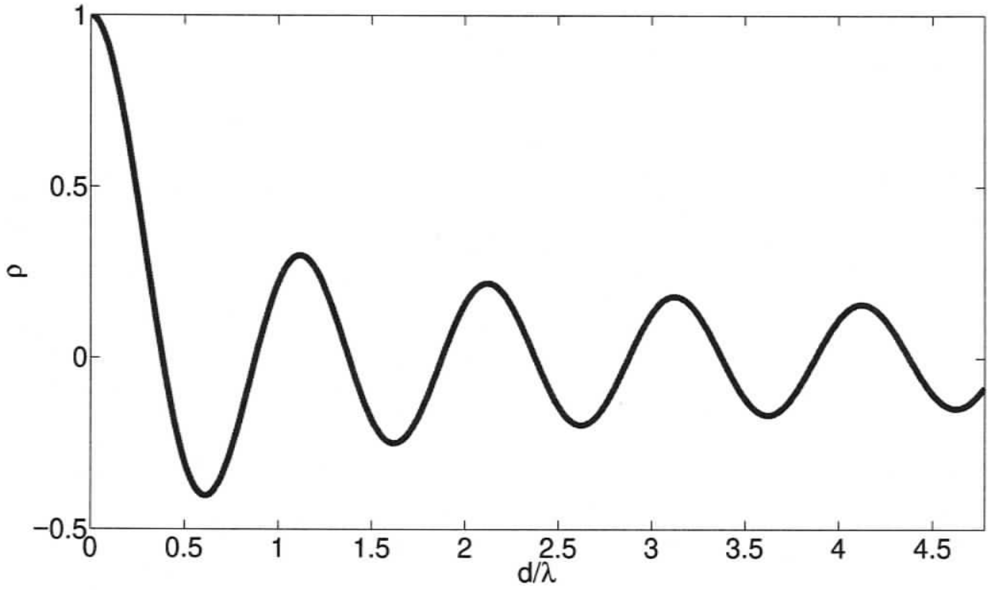

Figure 2.7: The zeroth order Bessel function of the first kind versus λ

$$\rho(d, f) = J_0(\frac{2\pi d}{\lambda}) \tag{2.2}$$

where $\lambda = c/f$ is the wavelength and c is the speed of light. A half-wavelength spacing is therefore considered an ideal choice for minimizing the correlation without greatly increasing the physical dimensions of the array. However, when the scattering is sparse and non-isotropic, ρ does not fall quite so rapidly with d. The coherence distance, D_c, then increases, and a much larger d may be required to achieve sufficient decorrelation. Although the scattering environments are not identical among different places, the half-wavelength rule nevertheless provides a simple rule of thumb for array design. If the channel is asymptotically isotropic in the horizontal plane, the correlation becomes a two dimensional Bessel function of d with circularly symmetric contours about the point of reference [24].

The spatial correlation coefficient can be computed as:

$$\rho_{(x,y)} = \frac{|s_{ref}(t) \cdot s_{(x,y)}(t)|}{\sqrt{\int s_{ref}^2(t)dt} \cdot \sqrt{\int s_{(x,y)}^2(t)dt}} \tag{2.3}$$

where $s_{ref}(t)$ is the received signal at the reference position and $s_{(x,y)}(t)$ is the received signal at coordinate (x, y). Since the channel is ergodic, we use time average function of the DSO to compute the statistical average.

The characterization of spatial correlation is conducted with Scenarios 1,2,4,5 and 6. The experiments are performed with a fixed transmit antenna while allowing the receive antenna to move on a square grid of measurement points. The measurement points must be spaced $\Delta x = \lambda/2$ or more apart, where λ is the wavelength of the pulse, to allow the measurement points experiencing independent fading [10]. Thus we choose $\Delta x = 20$ cm for HL9200 pulse generator and $\Delta x = 3$ cm for AVE2 pulse generator. Due to spacing restrict, the measurement grid for HL9200 pulse generator is 5×5, with a spacing of 20 cm between two adjacent measurement points, while the grid for AVE2 is 45×45 with a spacing of only 3 cm. At each position, 10 sets of data are recorded and averaged to remove the noise effect.

Fig. 2.8 and Fig. 2.9 show the spatial correlation results in a contour format for NLOS Scenario 1 and LOS Scenario 4 using HL9200 pulse generator. The value on the contour indicates the correlation coefficient between the current position and the reference position, which we have assigned to be at the center of the grid with a coordinator $(3, 3)$. The figure indicates that the position near the reference always has a high degree of correlation, while those further away from the reference tend to be less correlated as expected. However, the spatial correlation starts to oscillate a bit as the distance is further away. That is, some positions show higher correlation than certain nearby positions.

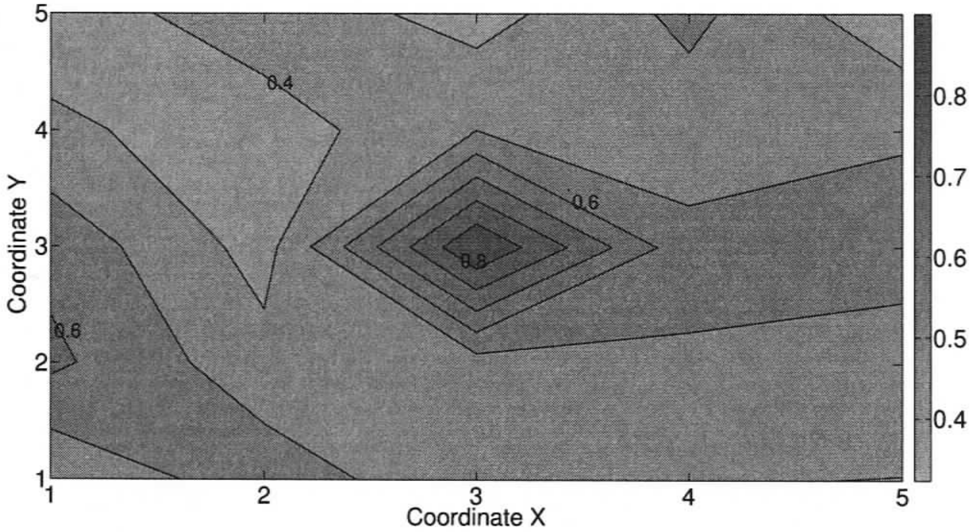

Figure 2.8: Spatial correlation of Scenario 4 (LOS)

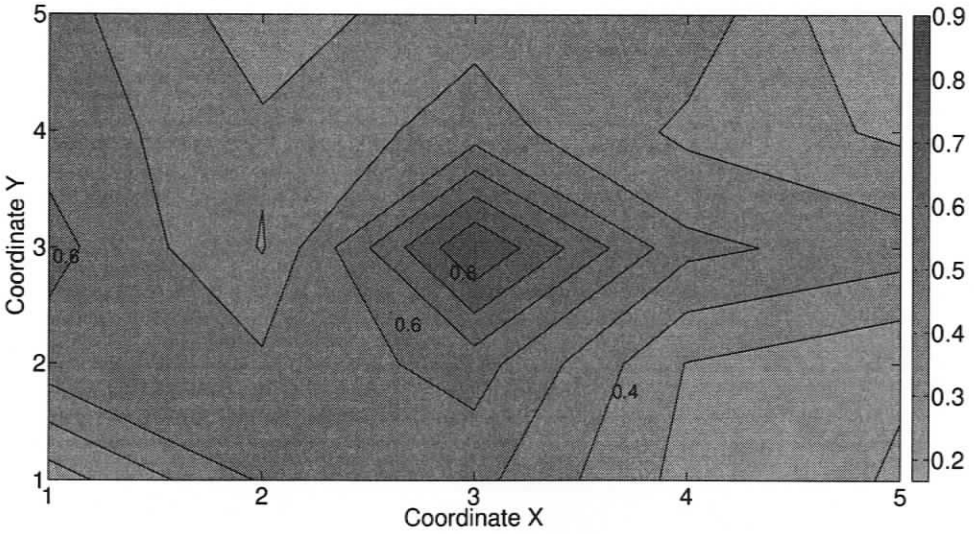

Figure 2.9: Spatial correlation of Scenario 1 (NLOS)

With regard to the AVE2 pulse generator, the wavelength corresponding to the center frequency is only 6 cm, which is much smaller than the HL9200 pulse generator. The measurement point spacing is only 3 cm in this case, hence much more measurements can be achieved. The corresponding spatial correlation contours are shown in Fig. 2.10 and Fig. 2.11. Compared with Fig. 2.8 and Fig. 2.9, the two dimensional oscillating feature is more evident. Hence, in a specified area, the further apart the antennas the better is not always accurate. It is explicitly shown from Fig. 2.8 to Fig. 2.11, the spatial correlation drops fast and monotonically within a small area that centered at the reference point with a radius of about one λ. Outside this area, the correlation parameter begins to oscillate. The decaying oscillatory response of ρ is as expected becomes a two dimensional quasi Bessel function of distance with contours circularly symmetric about the point of reference. However, the environment of our measurement campaign is not isotropic, so partial decaying and oscillatory behavior is observed from Fig. 2.8 to Fig. 2.11. Hence, to efficiently make use of space for MIMO antenna array lay out, it is wise to space antenna array with a distance of one λ to get a relatively low correlation in order to achieve the diversity gain, and at the same time, the antenna array size is minimized.

Another important thing to be noted is that, for different portion of the received signal, the spatial correlation calculated are in sharp contrast to each other. We could observe from Fig. 2.12 to Fig. 2.14 that the dominant multipath components, which are likely to be contained in the initial portion of the CIR, are highly correlated, whereas the subsequent diffuse multipath shows very little correlation. The observation can be explained as follows. The first arriving paths are most likely from the LOS path and a single dominant reflection, and tend to be more prominent in the received signal. While subsequent multipath may undergo multiple reflections which are distance away and independent of each other. Since those reflectors are more

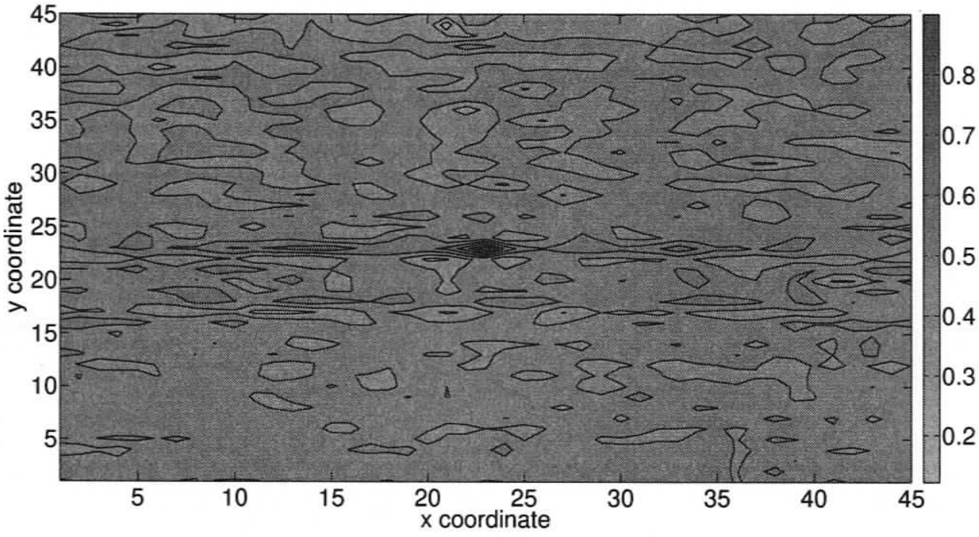

Figure 2.10: Spatial correlation of Scenario 4 (LOS)

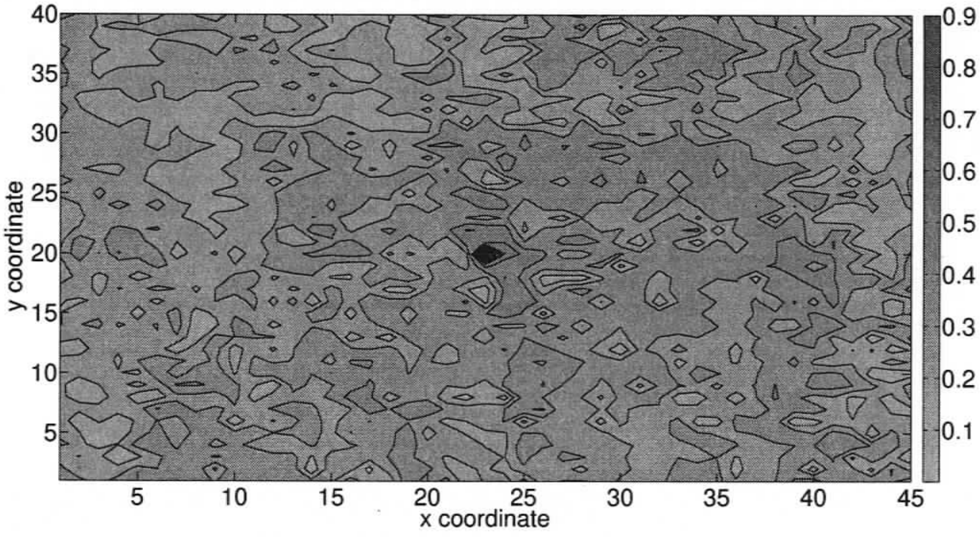

Figure 2.11: Spatial correlation of Scenario 6 (NLOS)

evenly distributed around the Tx and Rx, paths are received from all directions. This result has important implications for indoor multi-antenna applications: low spatial correlation is observed when we consider the entire received signal. However, if the receiver captures only the early, dominant components, a much larger antenna separation is required to obtain low spatial correlation.

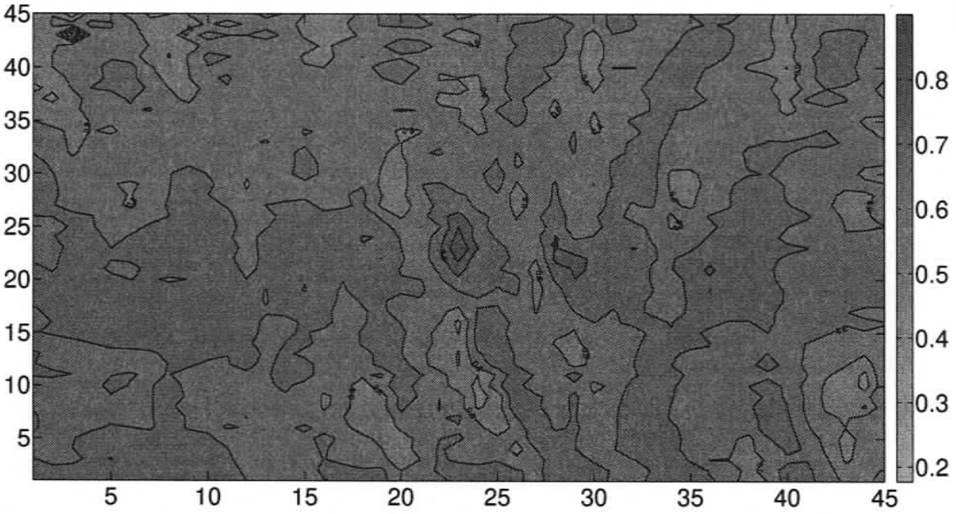

Figure 2.12: (a) Spatial correlation within the first 10 ns (LOS)

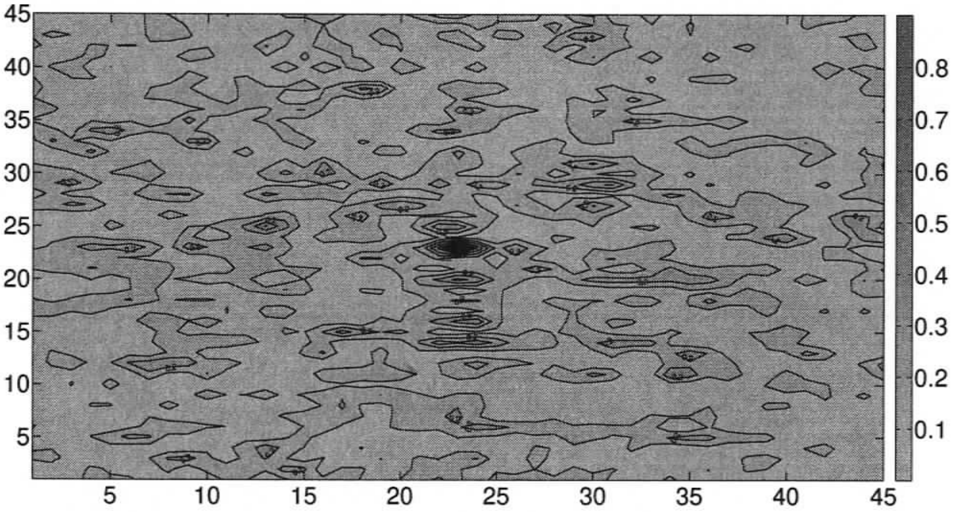

Figure 2.13: (b) Spatial correlation after 10 ns (LOS)

Similar results can be found in the literature. In [24], the coherence distance, D_c, defined as the distance within which $\rho \geq 0.5$, is approximately 4 cm for most full-band UWB channels. The center frequency used in [24] is 6.85 GHz and the corresponding wavelength is 4.38 cm. Therefore, one wavelength spacing is in agreement with our measurements. Besides, due to the large angular spreads of the UWB indoor chan-

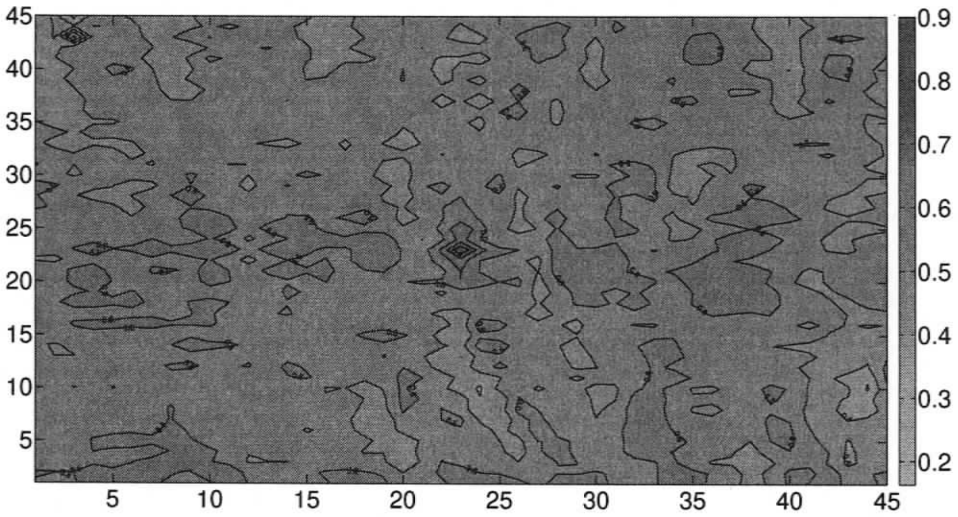

Figure 2.14: (c) Spatial correlation over the whole signal (LOS)

nel, their correlation results appear to follow a pattern resembling a Bessel function of distance as well. In [25], the correlation between different parts of the received signal is investigated. It is shown that the first delays are strongly correlated while the subsequent delays are much less correlated in LOS scenarios. For the NLOS scenario, the same phenomenon can still be observed. However, the first delays are less correlated compared to the LOS case. In addition, the average coherence distance at the magnitude of 0.7 is measured to be around $\lambda/2$ and $\lambda/2.5$ for LOS and NLOS respectively.

2.4 Ultra Wideband Body Shadow Effect

Human body shadowing is a significant propagation effect in indoor environments. The changes seen in the received signal as a result of the body shadow effect is that a few multipath rays appear, disappear or slowly change their shapes and strengths. These changes will affect the received energy and the channel delay spread. Moreover, in contrast to current outdoor cellular systems, the transmission power and the elevation of base stations is much lower in an indoor environment. Thus, the propagation loss by body shadowing greatly affects the received signal strength even when considering a multipath environment where several rays contribute to the received power. UWB communication systems are designed to operate at a very low transmission power, thus the human body shadowing is of great importance to the system link budget estimation. To make sure the system can work properly and stably, sufficient link margin should be kept to accommodate body shadow interference.

We characterize the shadowing effect caused by the human body through a series of measurements between the Tx and Rx antennas in Scenario 5 with a person standing in a known position but on an expanded 14 × 5 grid shown in Fig. 2.15. The distance between two adjacent measuring points is 30 cm and between the two antennas is 4.5 m. HL9200 pulse generator is employed in this measurement campaign.

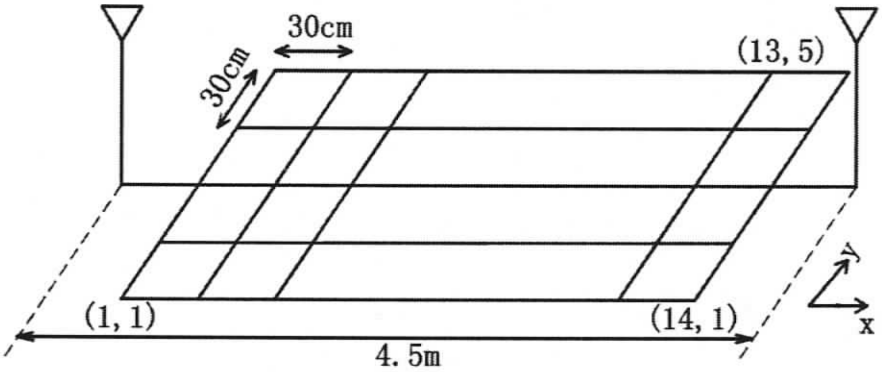

Figure 2.15: The grid for body shadow effect measurements.

Based on Fresnel Zone theory, LOS is not only the visual path between transmitter and receiver, but also contains 60 percentage of the first Fresnel Zone in each point between the two antennae. Thus, the NLOS communication is the case that the obstacle covers more than 40 percentage of first Fersnel Zone in the specific point.

The radius of the First Fresnel Zone is defined as

$$F_1 = \sqrt{\frac{\lambda d_1 d_2}{d_1 + d_2}}, \tag{2.4}$$

where F_1 is the the first Fresnel Zone radius in meters, d_1 is the distance of middle point from the transmitter antenna in meters, d_2 is the distance of the middle point from the receiver antenna in meters, and λ is the wavelength of the signal transmitted.

As Fig. 2.16 shows, the shape of Fresnel Zone between two antennas is like a eclipse that the maximum cross section is appeared in the middle-distance of the two antennas. The radius of this specific maximized region is given by

$$b = \sqrt{\lambda d/4}, \tag{2.5}$$

whereas in our measurements, the wavelength is 25 cm, the distance d is equal to 4.5 meters, and hence $b = 0.53$ m.

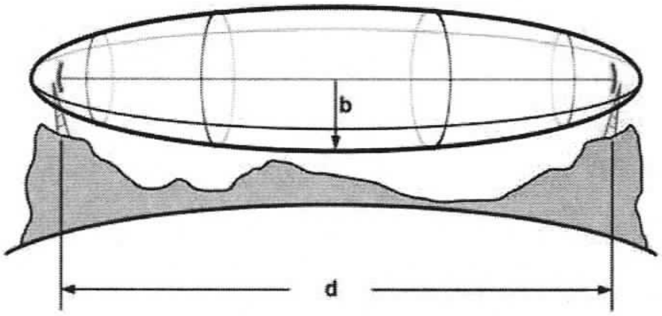

Figure 2.16: Elliptic shape of Fresnel Zone.

2.4.1 Body Shadow Effect on Energy Fluctuation

Fig. 2.17 shows the body shadow effect by plotting the normalized power coefficient in a contour form. The x-axis and y-axis represent the blocking position on the expanded 14×5 grid. The value on the contour is the normalized power coefficient calculated as

$$\rho_P(x, y) = \frac{\int_0^T r^2(t, x, y)dt}{\int_0^T r_0^2(t)dt} \tag{2.6}$$

where $T = 100$ ns is the length of the CIR recorded by the oscilloscope, and this time is long enough to include all the significant multipaths, $r_0(t)$ is the received signal when nobody is standing between the transmit and receive antennas, and $r(t, x, y)$ is the received signal when a person is standing on the grid coordinate (x, y).

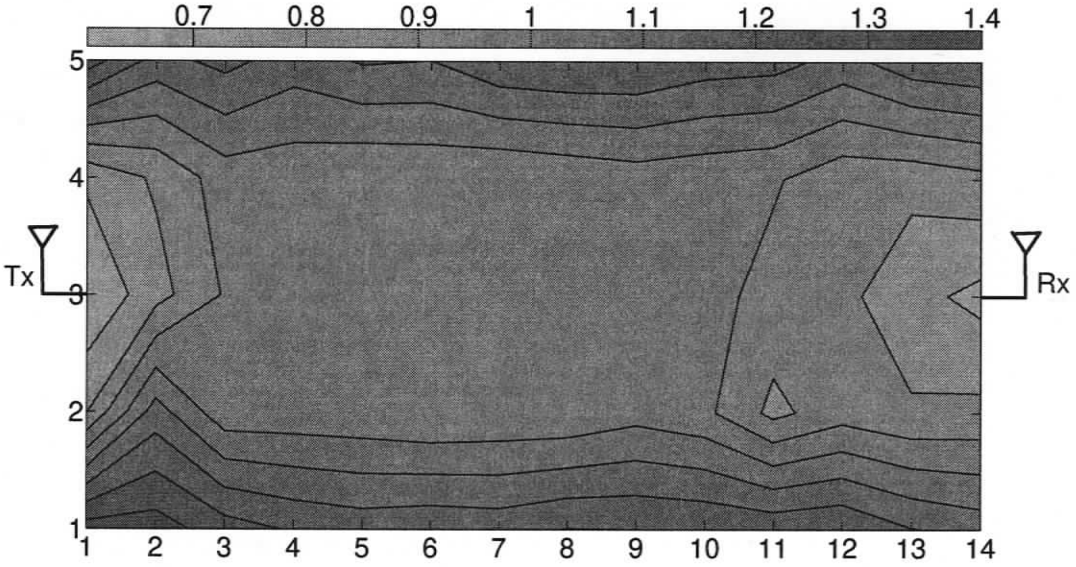

Figure 2.17: Normalized power coefficient in the presence of body block shadow effect.

Fig. 2.17 demonstrates the energy fluctuation due to people's blockage. It is worth noting that when a person stands in the middle of the LOS path, the energy attenuation is only less than 10%. The reason is that some of the emitted wave can diffract over the human body and reach the Rx antenna. Meanwhile, a number of multipaths reflected from the walls, ceiling and surrounding furnitures contribute to the received energy. If a person standing on the two sides of the direct path, the received energy is even larger than nobody in the vicinity of the transmission path. That is because the human body can act as an obstruction as well as a scatterer at the same time. When a person stands on the two sides, the body acts more like a scatterer than an obstruction, and as a result, the received signal strength is even higher, and vice versa. However, when the people is very close to the transmitter or receiver, a large angle of emitting area is obstructed, and almost 30% of the energy is lost.

From Fig. 2.17 and the analysis above, we can find out that the degree of attenuation is position dependent, and intuitively, the nearer towards the antenna, the more attenuation is generated. As long as the dominant LOS path is not blocked, the received signal energy is even higher than people absence in the transmission environment. Therefore, the above results imply that for non-coherent energy detector UWB receiver, the body shadow effect will not affect the performance much. However, due to pulse shape distortion and multipath variation, the CIR may change dramatically, resulting in a performance degradation for coherent receivers if the channel is not estimated in time. To combat the body shadow effect, the channel estimation should be performed as the channel changes.

As mentioned before, the impulse UWB signal has very fine temporal resolution, thus the majority of the multipaths are resolved from the received signal. This property not only gives the UWB system high resistance to small scale fading, but also allows the system to combat body shadow effect. Compared to narrowband systems, the power attenuation of impulse UWB caused by body shadow effect is much less. Fig. 2.18 shows the cumulative distribution function (CDF) of the received signal over 14×5 grid at various measurement locations, including indoor office environment, cafeteria environment and hall way environment. The received signal power over the entire measurement grid does not vary by more then 2 dB. This result is typical of UWB signals and is in dramatic contrast to body shadow effect observed in narrowband signals. However, it must be noted that most practical receivers cannot capture the entire received signal energy due to limitations in computational complexity, thus tempering this benefit to some degree.

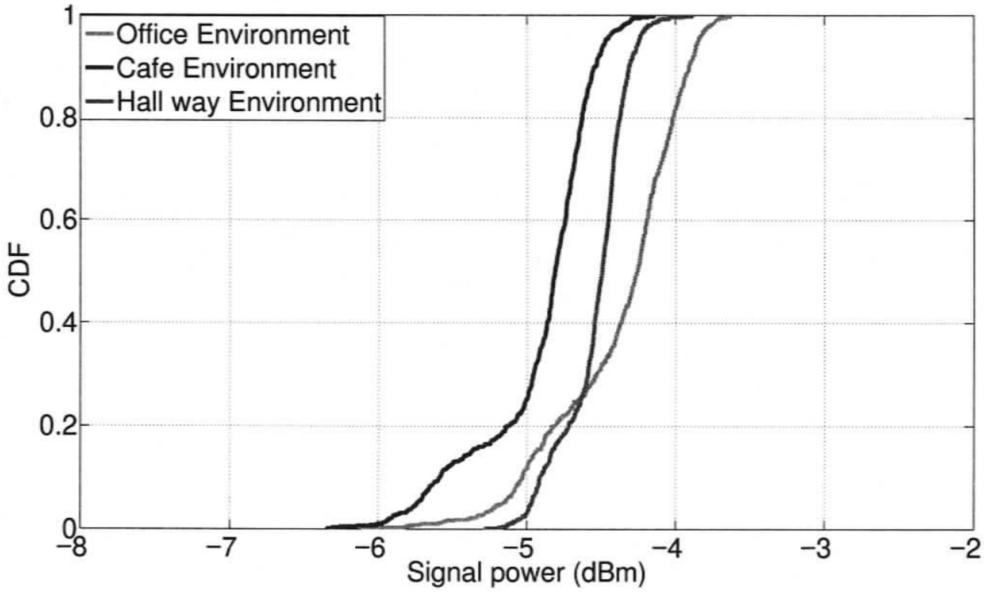

Figure 2.18: The CDF of the power attenuation in the presence of body shadow effect.

2.4.2 Body Shadow Effect on Shadowing Distribution

Shadowing, as the name suggests, refers to the fading where a large obstruction such as a hill or large building obscures the main signal path between the transmitter and the receiver in mobile communications. The amplitude change caused by shadowing is often modeled using a log-normal (Gaussian with dB power) distribution with a standard deviation according to the log-distance path loss model. Similarly, we could also define shadowing fading in indoor UWB communications, which is a random variable caused by furnitures or human blockage. We investigated the distribution of the energy fluctuation caused by human shadowing in different scenarios, including dense multipath hallway environment (LOS), sparse multipath lobby environment (LOS), and furnished indoor office environment (LOS & NLOS). For each scenario, 750 CIR which are affected by human body shadow effect are recorded in order to study the distribution of the shadowing fading. The cumulative distribution function (CDF) for hallway and indoor office (LOS) scenarios are shown in Fig. 2.19 and Fig. 2.20. From these figures we could observe that the Gaussian distribution fits the empirical data very well.

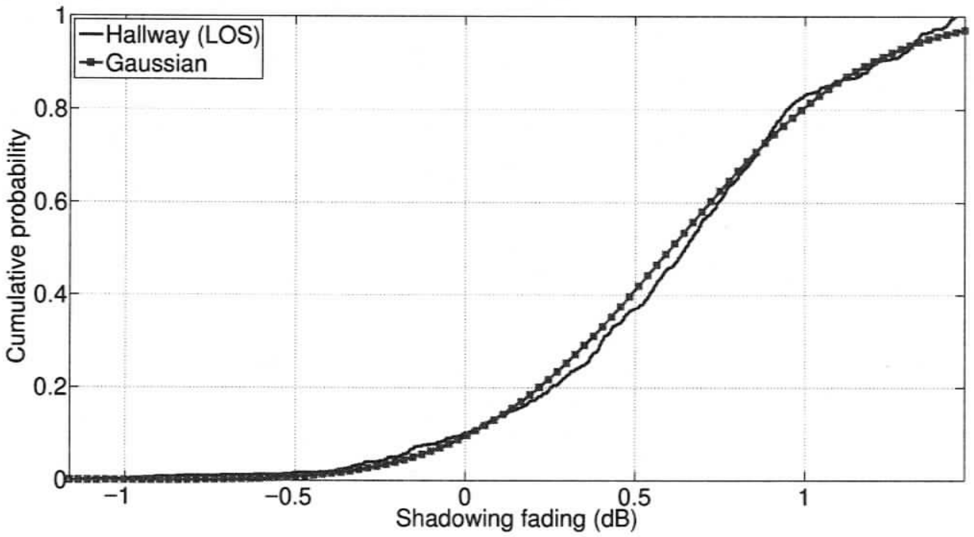

Figure 2.19: The CDF for hallway scenario.

2.4.3 Body Shadow Effect on RMS delay spread

The RMS delay spread (τ_{RMS}) is the square root of the second central moment of a power delay profile. τ_{RMS} is a good measure of the multipath spread; it gives an indication of the potential severeness for inter symbol interference (ISI). Strong multipaths with long delays contribute significantly to τ_{RMS}. When designing com-

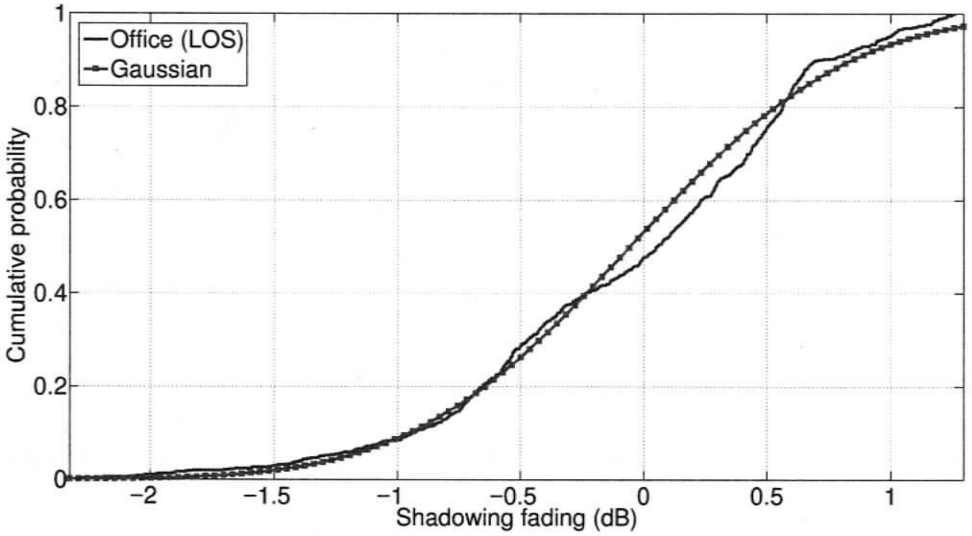

Figure 2.20: The CDF for office (LOS) scenario.

munication systems, the RMS delay gives a measure of performance degradation in the system, caused by ISI. Thus a common rule of thumb, adopted while designing a communication system to operate at a certain data rate with negligible performance degradation, is to use a symbol period much greater than the average RMS delay spread. Typically, the symbol period used is about five times greater than the average RMS delay spread of the radio channel [26]. However, in high data rate applications, the ISI can be mitigated by using equalization technique.

Fig. 2.21 shows the CDF of the RMS delay in the dense multipath hallway environment and Fig. 2.22 is in the sparse multipath lobby environment. The red dashed line in the figure is the RMS delay without people's shadowing effect. From Fig. 2.21 we can see more than 60% of the CIR has a longer RMS delay spread than without people's shadowing. The increase of the RMS delay is likely due to the dominant LOS path is blocked sometimes, which makes the subsequent multipaths with long delays more significant. The variation of the RMS delay is about 15.5 – 20 ns in hallway environment and 17 – 22 ns in Lobby environment, hence, for both the two

scenarios, the variation of the RMS delay is about 5 ns, which likely resulted from the disappearance of the paths due to blockage and appearance of the new paths due to reflection off people. However, since the size of the measurement environment is limited, the body shadowing does not affect the RMS delay value much.

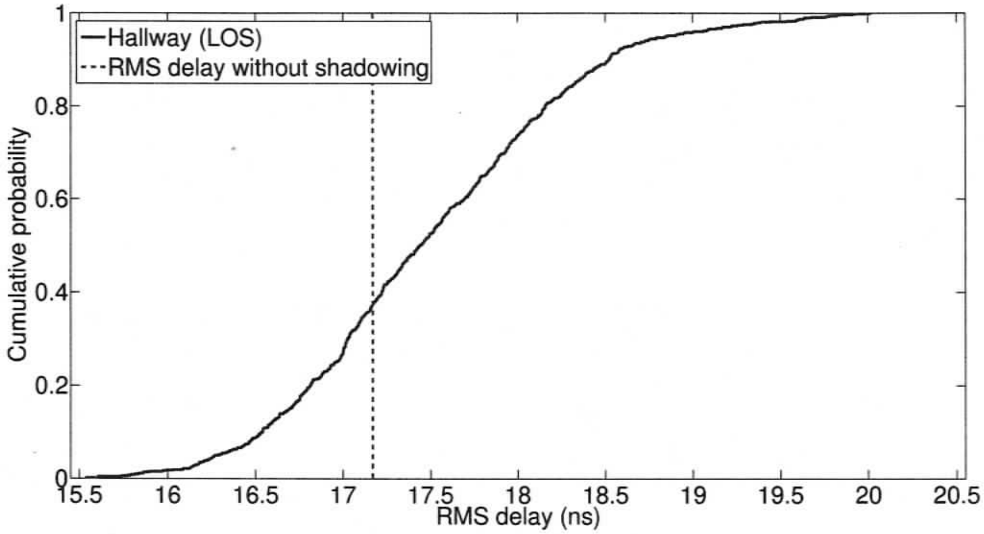

Figure 2.21: The CDF of RMS delay in hallway environment with human shadowing.

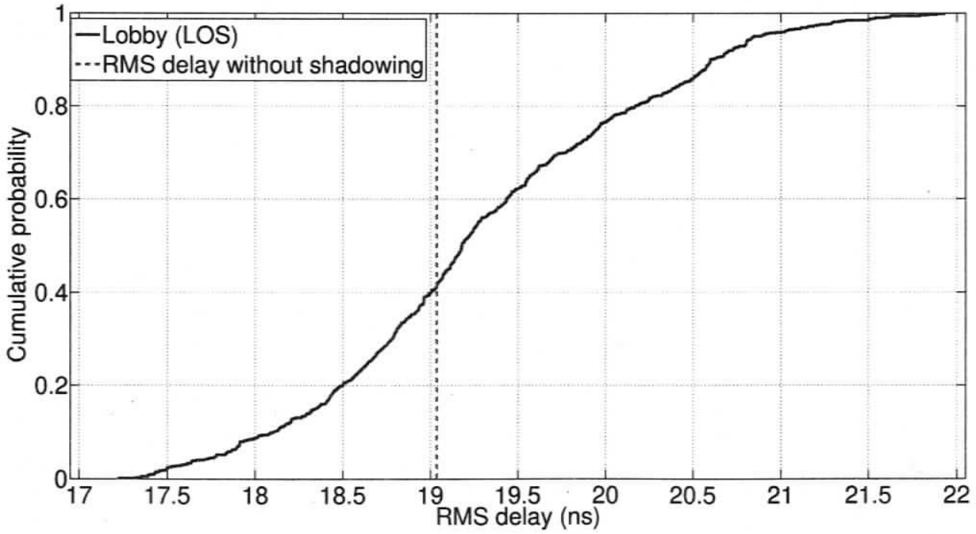

Figure 2.22: The CDF of RMS delay in lobby environment with human shadowing.

Other human body blockage measurement results can be found in the literature. In [27], the average power loss due to human blockage is about 4.5 dB and the RMS delay spread change on average is 6.9 ns. While in [28], the average power loss of the output signal is 4.89 dB. All these results imply that in the UWB radio link, the human blockage will not interfere the signal power much. However, at least 5 dB link margin should be kept for the system design, because of the low transmission power for UWB systems as regulated by FCC.

2.5 Summary

In this chapter, a variety of properties of indoor UWB channels have been investigated based on time domain measurements. Firstly, through pulse generator based and AWG based measurements, we have found that reciprocity holds in both the baseband and the RF passband. From the results of the measurements in different scenarios, we claim that the reciprocity exists in both LOS and NLOS channels, and is also distance and frequency independent. Secondly, we have performed the spatial correlation measurement on a 2D grid and observed that as the distance between Tx and Rx increases, the trend is that the correlation coefficients decays and oscillates correspondingly. Moreover, an antenna spacing distance of one wavelength is a good choice for low spatial correlation and small array size. Thirdly, body shadow effect has been measured, and the results have demonstrated that the degree of attenuation depends on the position of the obstruction, especially the angular position and the distance from the antenna. Moreover, the shadowing effect is found to fit a Gaussian distribution, and the energy fluctuation is relatively low compared to narrowband systems. The RMS delay spread is changed by the body shadow effect, but the variation is within 5 ns.

Chapter 3

The Temporal Variation of Indoor Ultra-wideband Channel

The development of efficient UWB systems for high-rate wireless links requires an accurate knowledge of the radio propagation mechanisms. Thus, much effort has been put into the measuring and modeling the UWB channels. However, the issue of temporal variations in the UWB propagation channel has been scarcely investigated so far. This chapter presents a study of the time variance of a UWB channel induced by the motion of people, and several important properties of the temporal variation of a channel are examined.

The wireless channels undergo dynamic shadowing and fading, so it is essential to have detailed knowledge of radio propagation in time varying environments for designing efficient transceivers. There are two kinds of temporal variations in the indoor radio propagation channel: (1) variations due to moving transmitter or receiver in a static environment. Examples of this kind of variation are very common, such as mobile terminals and portable computers; (2) variations due to moving people when both Tx and Rx are stationary, e.g., a Wi-Fi user in a cafeteria where there are constantly people moving around [29]. In general, human body scattering and shadowing is a significant propagation issue in indoor communications, where the human body constitutes a reflector or obstacle for electromagnetic waves [30]. Therefore, it is of interest to assess the impact of the movement of people on UWB indoor channel propagation characteristics, and consequently, on the transceiver design of the UWB systems.

The temporal variation of the indoor narrowband and wideband channels has been investigated in some previous work. A comparison of time varying indoor radio propagation characteristics at 910 MHz and 1.75 GHz was reported in [31] and the statistics of short time variations of indoor radio channels at 910 MHz was investigated in [32]. Extensive measurements and analysis of indoor time varying channels reported by Hashemi [29] were based on continuous wave (CW) technique with carrier frequency of 1100 MHz. Influence of human motion on indoor channels was investigated by Marinier et. al. at 30.1 GHz near the border between SHF and EHF bands [33]. The temporal variation of UWB propagation channels has also been investigated by Pagani and Pajusco, using both time and frequency domain measurements and analysis [34, 35, 36].

In this work, extensive measurements of the UWB channel's temporal variation in a modern office environment under diversified sets of conditions are conducted. A real time measurement campaign involving moving scatterers was performed in typical office environments, hall way environments and lobby environments. Compared to the previously reported UWB time varying channel measurements, our work investigates a much wider bandwidth and more diversified environments. The direction and position of the movement are controlled in the measurements. The analysis of the measurement results provides detailed information about energy fluctuation, time correlation coefficient and Doppler power spectrum.

3.1 Measurement Setup and Scenarios

The experimental observation of time variations in a UWB radio link requires the deployment of equipment capable of sounding dynamic channels [31]. Thus frequency domain measurements employing a vector network analyzer (VNA) are not proper for time varying channel measurement, since the VNA takes several seconds to perform one measurement. An intuitive and efficient way of recording the CIR is to emit an ultra short UWB pulse, and record the received signal by a DSO for post signal processing. Due to the internal jittering of the DSO, the received signal may not align in time, and 1-2 samples (25-50 ps) time shifts occur. This can cause dramatic performance degradation for correlation analysis, due to the stringent timing of the ultra short pulses. Therefore, before processing any received signal, signal alignment should be done in advance. We use Hyperlabs HL9200 pulse generator to periodically generate a ultra short pulse with a rise time of only 50 ps, and a pulse width of 70 ps. In order to capture these short pulses, an Agilent DSO81004A DSO with a sampling rate of 40 Gsamples/s is employed. Both Tx and Rx use Electrometric EM-6865 biconical, omni directional antennas with vertical polarization.

To capture the dynamic change of the indoor UWB channel, it is necessary to record a long time period with a relatively high repetition rate, and at the same, hold the high sampling rate as well to meet the Nyquist sampling necessity. Thanks to a technique called "segmented memory" provided by Agilent, the DSO can store information only during the active bursts or pulses; they store no information during the inactive periods. Since the valuable memory is not used during the inactive periods, we can capture more of the critical signal activity. Using segmented memory, we capture the CIR every 1 ms for 4.096 s, which consists of 4096 sets of CIR. In each set, a 100 ns long signal window sampled at 40 Gsamples/s is stored, which captures the majority of the significant multipaths in a typical indoor environment.

Measurements were carried out in the Engineering Office Wing at the University of Victoria. Three typical scenarios including dense multipath hallway environment, sparse multipath lobby environment, and furnished modest multipath office environment were chosen to perform the temporal variation measurements. The antenna separation distance is 8 meters. By maintaining both the Tx and Rx antenna at fixed positions, we investigate two ways of motion: one is to cross the LOS path perpendicularly from a set of positions; the other is to walk along the LOS path in parallel from several positions. The measurement scenario is depicted in Fig. 3.1. We use label C_n $(n = 1, 2, ..., 15)$ to denote the position of crossing the LOS path, where C_1 is the nearest position to the Rx antenna, and C_{15} is the nearest position to the Tx antenna. To denote parallel path, we use label P_n $(n = 1, 2, ..., 5)$, where P_1 is the outermost trace and P_3 coincides with the LOS path. The distance between adjacent routes is 50 cm, whether crossing the LOS path or parallel to the LOS path.

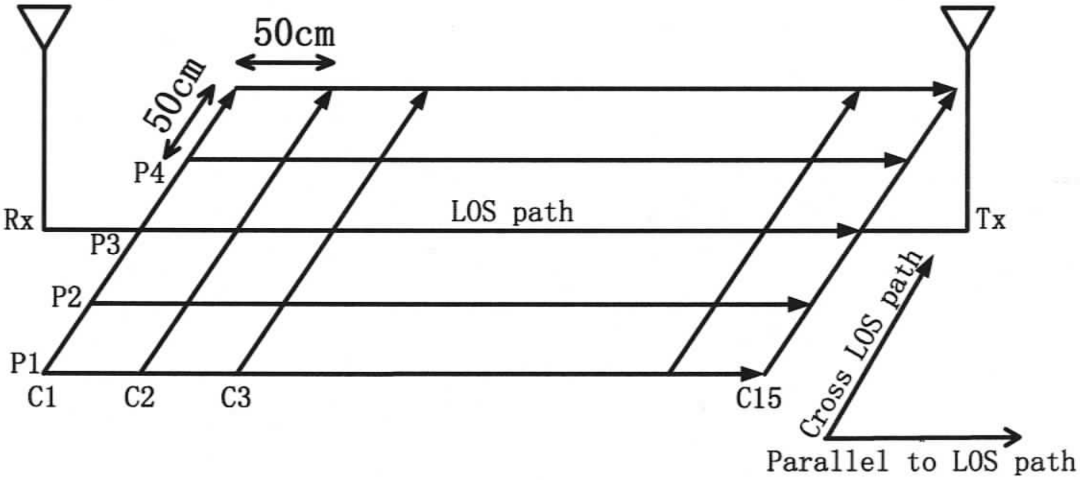

Figure 3.1: Measurement scenarios.

In each measurement, a controlled manner of walking is recorded every 1 ms for a total of 4.096 seconds (which is the maximum time within the DSO's capability). During each recording, care was taken to eliminate other peoples' unwanted movement by performing the measurement around midnight.

3.2 Measurement Results and Analysis

In real life situations the indoor UWB channel may undergo time varying fading and shadowing phenomenon. People's motion in the vicinity of the transceiver can distort the emitted signal. Fig. 3.2 illustrates a set of empirical channel impulse responses separated 300 ms apart. It should be noted that although the LOS path (the direct path) are blocked and attenuated by the human body, the reflected and scattered multipaths remain approximately the same over short times. Besides, not only obstruction by bodies but also reflection onto them may contribute to the total signal strength and therefore to the overall propagation characteristics. In this section, the temporal fading phenomenon are analyzed and the major results are presented.

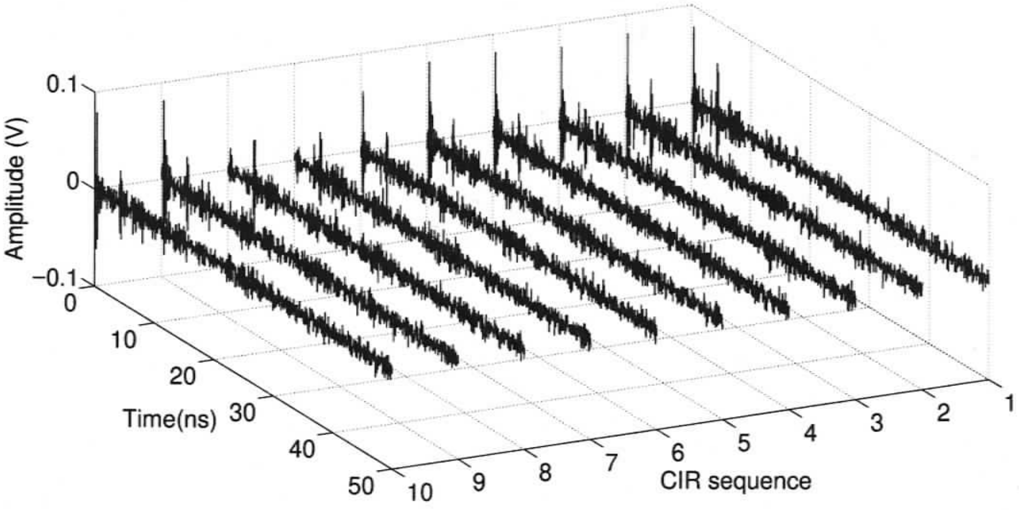

Figure 3.2: Sequences of temporal adjacent impulse response profiles.

3.2.1 Energy Fluctuation

Fig. 3.3 and Fig. 3.4 display the energy fluctuation induced by people's motion along route C_2 and C_8 in the hallway environment respectively. From these figures we can observe that when a person travels far from the LOS path, the received signal is composed of the dominant LOS component and the specular reflected rays from the human body and furnitures around. Thus the signal strength would fluctuate a little bit due to people's movement that could block some existed multipaths as well as generate some new multipaths. As a person blocks the LOS path, the received signal is composed of the specular reflected rays from the furnitures around and the diffracted rays from the human body. Consequently, the received signal strength is in a wave trough, and the energy is attenuated by about 2 dB for route C_2 and only 0.5 dB for route C_8. Moreover, one may notice that when a person approaches or leaves the LOS path, there is an obvious energy increasing of about 0.5 dB, which is possibly because an additional reflection is generated by the human body. Similar phenomenon is reported in [34] where a real-time measurement was performed in the 4-5 GHz band.

While from Fig. 3.5 and Fig. 3.6, we could observe that as a person moves parallel to the LOS path, the received signal is induced by the unblocked LOS component and the specular reflected rays from the moving human body and furnitures around. Thus the signal strength fluctuations around the mean value are small due to the fact that a strong dominating LOS path exists. Obviously, the parallel movement impairs the received signal much less than the movement of crossing the LOS path.

Fig. 3.7 vividly demonstrates the variation of the received energy due to the movement of the surrounding people. The measurement scenario of Fig. 3.7 is in the office environment, and a person walks cross the LOS path with a constant velocity from position C_1 to C_{15}. The most distinct part of this figure is the blue strip in the middle,

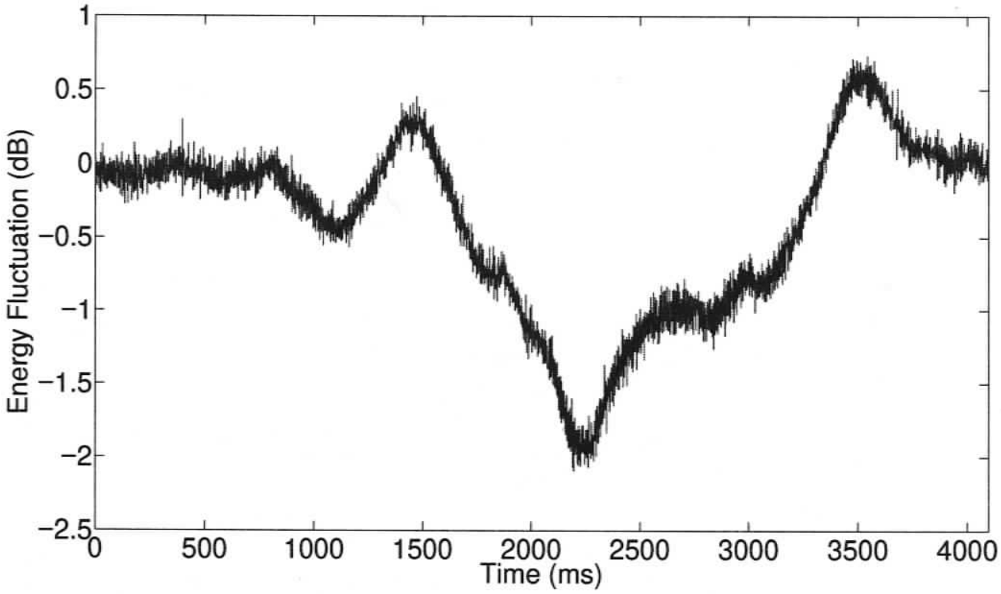

Figure 3.3: Cross the LOS path at position C_2.

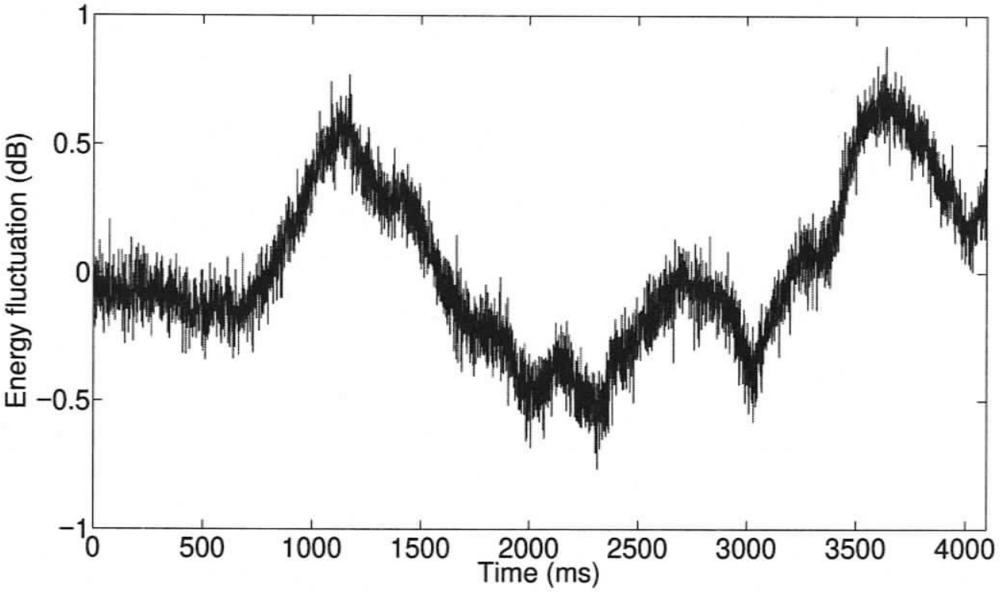

Figure 3.4: Cross the LOS path at position C_8.

which has a relatively low energy due to the block of the dominant LOS path. To be worthy of notice is that when a person walks from position C_1 or C_{15}, which corresponds to the Rx area or Tx area, the received energy reaches its lowest value because

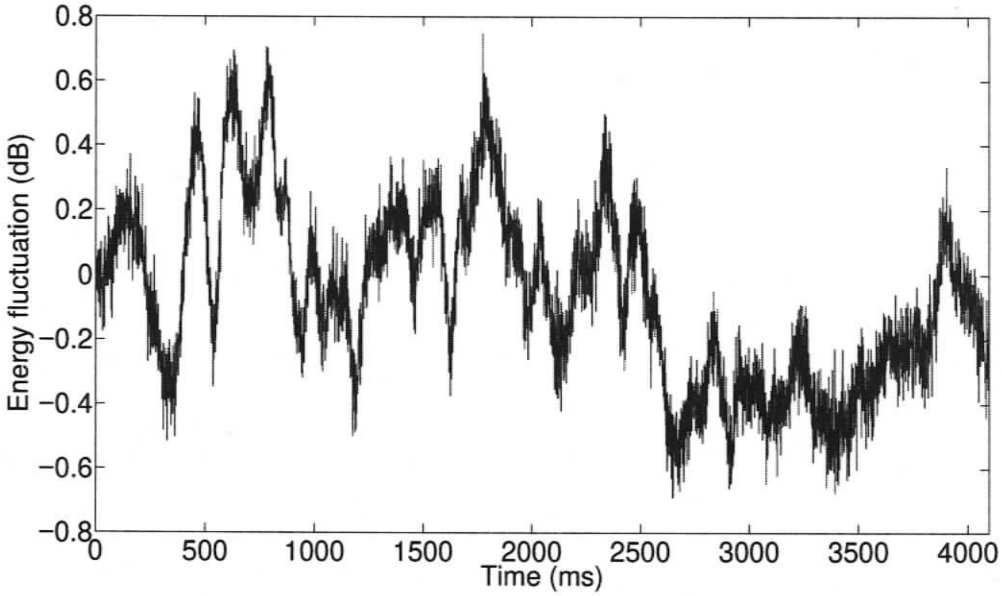

Figure 3.5: Parallel to the LOS path at position P_1.

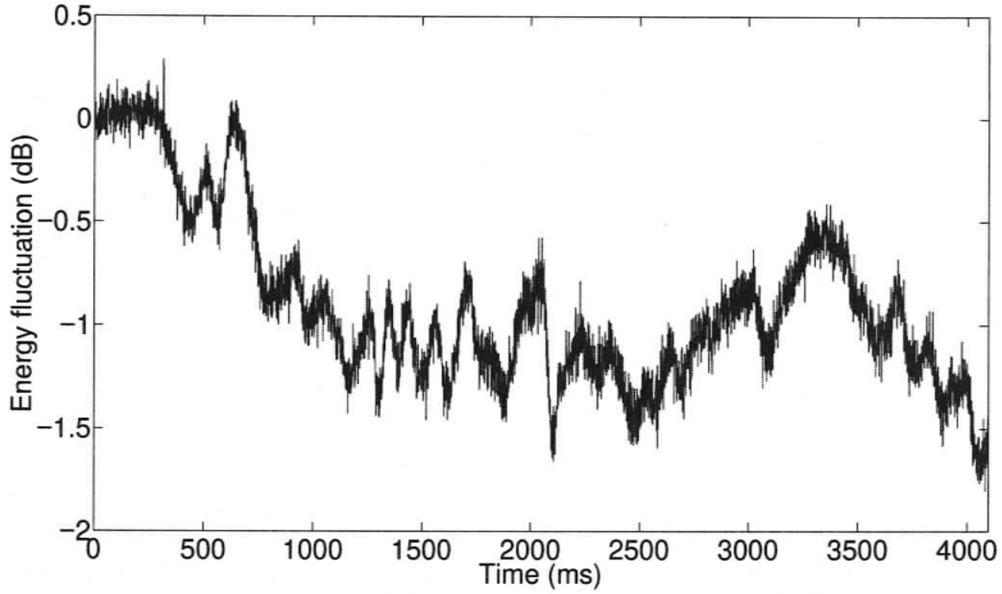

Figure 3.6: Parallel to the LOS path at position P_4.

a large portion of the emitted signal is blocked. On the two sides of the blue ribbon, the contour is almost symmetric. An interesting phenomenon is the red part of the contour denoting a higher received signal energy, and it appears when the person is very near the LOS path. The reason of this phenomenon is probably because additional propagation paths are generated by the people. Another phenomenon to be noted is that the movement in the vicinity of the Rx (around C_1 to C_3) generates less energy attenuation compared with the movement in the vicinity of the Tx (around C_{13} to C_{15}), which implies the Tx side is more vulnerable to temporal variation than the Rx side.

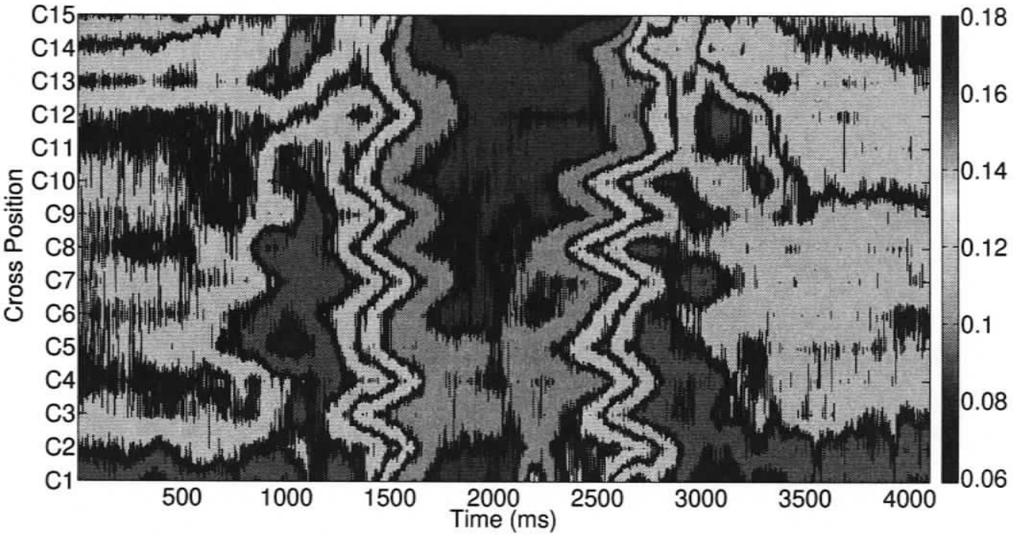

Figure 3.7: Received signal energy in the presence of human movement (cross the LOS path).

Fig. 3.8 demonstrates the variation of the received signal energy due to parallel walking. A dark blue strip is shown in the middle of the contour indicating low received energy, since the LOS path is blocked all the way when a person walks on the route of P_4. On the two sides of the dark blue ribbon, the received energy is relatively high and only little fluctuation can be observed during the 4096 ms recording time.

Table 3.1 summarizes the maximum energy fluctuation along the crossing position from C_1 to C_{15}. The dynamic energy fluctuation is calculated by subtracting the minimum value from the maximum value for each data record. It can be observed from Table 3.1 that changes in the dynamic range of fluctuation are more obvious for

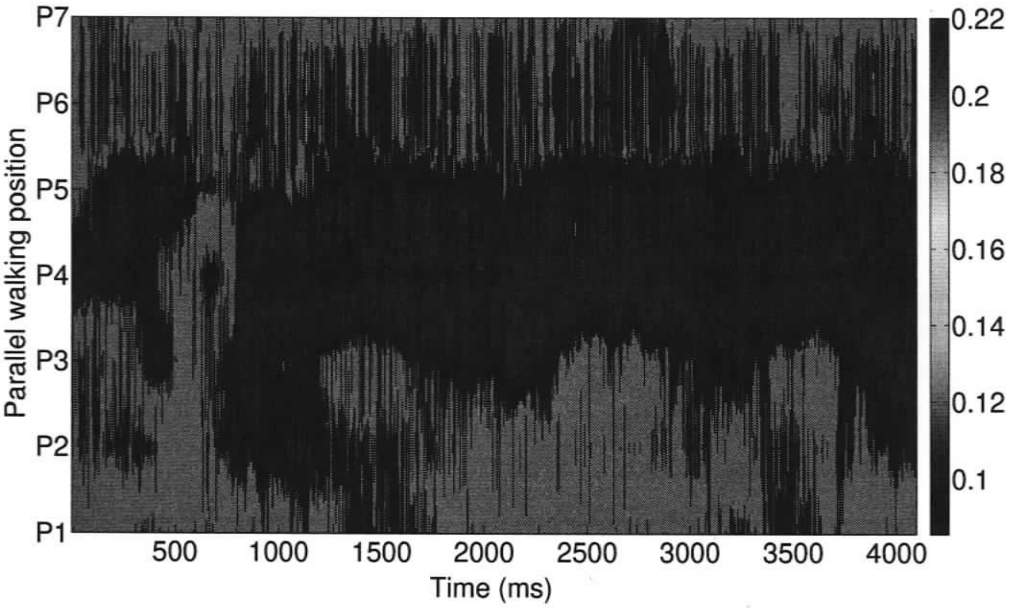

Figure 3.8: Received signal energy in the presence of human movement (parallel to the LOS path).

motion in the vicinity of the antennas, as compared to motion in the middle of the Tx-Rx antenna separation. Moreover, no deep fades exceeding 7 dB have been observed over all the measurements. In contrast to narrowband communication channels, in which the energy attenuation induced by people's motion can reach as high as 30 dB [29][33], the energy attenuation for UWB systems is relatively low. That can be explained by the unique characteristic of the UWB signals: the very fine time resolution that can resolve different reflection path, hence, although some paths are blocked by the human body, other paths can reach the receiver successfully. While for the narrowband signals, the multipath components have a time resolution that is less than the inverse of the signal bandwidth, so the received signal will undergo fast variations due to the constructive and destructive combining of the non-resolvable multipath components.

In addition, also note that the energy fluctuation in office and lobby environments is higher than in the hallway environment. Due to the relatively sparse multipaths

Table 3.1: Statistical parameters of the temporal variation data of crossing route

		C_1	C_2	C_3	C_4	C_5	C_6	C_7
Office	Fluctuation	6.77	5.16	3.98	3.13	3.60	3.32	2.60
	Correlation	0.71	0.76	0.77	0.81	0.80	0.82	0.82
	f_{RMS}	14.00	13.63	1.42	1.74	9.22	2.45	10.13
Hallway	Fluctuation	4.00	2.83	1.86	1.52	1.60	1.60	1.49
	Correlation	0.70	0.75	0.76	0.83	0.82	0.80	0.79
	f_{RMS}	9.46	12.89	13.59	11.58	13.49	2.42	2.47
Lobby	Fluctuation	6.33	5.40	5.00	4.52	4.05	3.69	3.56
	Correlation	0.67	0.75	0.71	0.78	0.81	0.79	0.82
	f_{RMS}	13.21	14.92	7.10	11.40	12.39	7.36	13.25

		C_8	C_9	C_{10}	C_{11}	C_{12}	C_{13}	C_{14}	C_{15}
Office	Fluctuation	2.63	2.43	2.93	2.80	3.23	3.27	3.91	4.75
	Correlation	0.83	0.83	0.83	0.82	0.80	0.77	0.74	0.71
	f_{RMS}	8.02	6.89	7.14	13.14	14.21	3.68	11.10	12.97
Hallway	Fluctuation	1.64	1.41	1.92	1.39	1.49	1.82	2.26	2.67
	Correlation	0.85	0.81	0.83	0.82	0.78	0.78	0.73	0.68
	f_{RMS}	2.69	11.51	13.22	13.81	6.43	8.82	11.61	12.37
Lobby	Fluctuation	4.10	4.07	4.10	4.21	4.32	4.52	5.54	6.79
	Correlation	0.81	0.79	0.80	0.79	0.76	0.75	0.73	0.72
	f_{RMS}	3.08	5.45	12.27	8.42	4.10	4.92	2.31	10.83

in the office and lobby environments, the dominant LOS component constitutes the majority of the received signal energy, while the subsequent multipath components only contribute a small fraction. Therefore, as long as the LOS path is blocked by a moving person, the signal strength would drop significantly. On the other hand, in dense multipath hallway environments, the non-direct multipaths contribute to the majority of the received signal energy. Thus even if the LOS path is blocked, the signal strength does not change much.

Table 3.2 presents the statistical parameters of the temporal variation from route P_1 to P_5 of three different scenarios. In contrast to the crossing movements, the energy attenuation induced by the parallel movements does not fluctuate much. One exception is when a person moves along the LOS path on position P_3. In this case, the

Table 3.2: Statistical parameters of the temporal variation data of parallel route

		P_1	P_2	P_3	P_4	P_5
Office	Fluctuation	1.32	1.89	6.52	2.41	1.84
	Correlation	0.86	0.84	0.75	0.81	0.85
	f_{RMS}	10.36	5.36	1.78	7.12	8.11
Hallway	Fluctuation	1.43	1.39	2.43	2.09	1.60
	Correlation	0.83	0.81	0.76	0.80	0.83
	f_{RMS}	12.69	11.85	7.13	10.80	13.30
lobby	Fluctuation	1.22	1.42	5.25	1.69	1.13
	Correlation	0.85	0.81	0.72	0.80	0.86
	f_{RMS}	12.91	4.42	11.12	8.92	11.35

dominant LOS component is always blocked by the human body, thus more energy is attenuated compared to the situation where an LOS path exists.

Similar results have been observed in [34], where the measurement was conducted in a UWB radio link. The attenuation of the mean power of about 8 dB is yielded by one person passing through the LOS path, while for 12 people crossing the LOS path case, the maximum attenuation of the mean power can be as high as about 15 dB. In [37], the short time variations in the indoor radio channel are studied by performing wideband measurements at 910 MHz. The range of power fluctuations are 7.3 dB to 9 dB for the LOS experiments, and 5.3 dB to 5.9 dB for the NLOS experiments. Compared to the narrowband CW measurement conducted by Hashemi [29], one person can cause about 30 dB power loss, and more people can increase the level crossing rates.

3.2.2 Temporal Correlation

The temporal correlation coefficient function $\rho(\Delta t)$ for amplitude fading at sample time separated by Δt seconds can be estimated using the following equation [33]

$$\rho(\Delta t) = \sum_{i=0}^{N-1} \frac{\rho_i(\Delta t)}{N} \tag{3.1}$$

where

$$\rho_i(\Delta t) = \frac{\overline{E[a_i(t)a_i(t+\Delta t)]} - \overline{E[a_i(t)]E[a_i(t+\Delta t)]}}{\sqrt{\overline{E[a_i(t)^2]} - \overline{E^2[a_i(t)]}}\sqrt{\overline{E[a_i(t+\Delta t)^2]} - \overline{E^2[a_i(t+\Delta t)]}}}. \tag{3.2}$$

in which $a_i(t)$ is the received signal waveform at time instant t, and $\overline{(\cdot)}$ denotes time averaging. N is the total number of segments, each of which has duration T. In the experiment, T is equal to 100 ns, which is sufficient to capture the majority of the significant multipaths. Note that $a_i(t) = a(t + iT_0)$, where T_0 is the repetition time of the recorded pulse. Here we set $T_0 = 1$ ms to capture the dynamic change of the UWB indoor channel.

From Fig. 3.9 and Fig. 3.10, we can observe that for the situation of crossing and parallel to the LOS path, the correlation coefficient is above 80%, which is much larger than their narrowband counterpart [29, 33] that can drop to 20%. Due to the large number of the resolvable multipaths of UWB signals, people's motion can only block and distort part of the multipaths, while others are not affected or suffer negligible influence. Therefore, in a time varing channel, UWB systems may outperform narrowband systems, which are more susceptible to the movement of persons.

The time correlation coefficient of $\rho(\Delta t)$ for $\Delta t = 2s$ are tabulated in Table 3.1 and Table 3.2. Observed from Table 3.1, the correlation coefficient is mostly higher than 60%, which indicates a high resistance to people's motion interference. It is worth noting that the correlation coefficient in the vicinity of the Tx and Rx antennas is about 10% less than the coefficient when the people are equal distant from both antennas. That is because when a person moves in the vicinity of the antenna, a relatively large portion of the emitted rays is blocked compared to the situation where a person is in the middle of the two antennas. Thus larger influence is induced by peoples' motion in the vicinity of the Tx and Rx antennas.

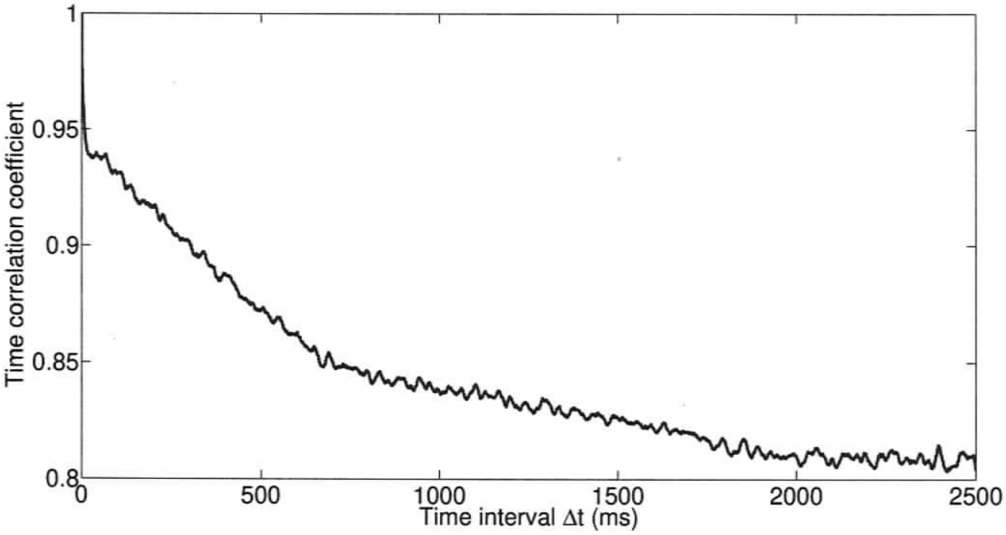

Figure 3.9: Cross the LOS path at position C_5.

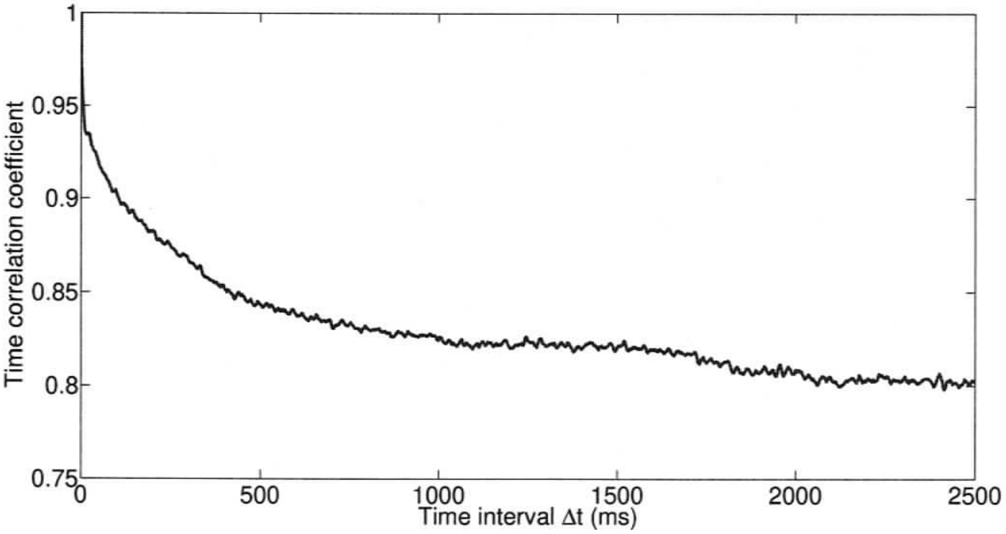

Figure 3.10: Parallel to the LOS path at position P_2.

For parallel walking, the moving people mostly play a role of a moving scatterer and reflector to generate extra multipaths, which results in a distorted received signal. Mothion nearer to the center LOS path, generates stronger reflected multipaths. Therefore, as observed in Table 3.2, the correlation coefficient drops as the parallel walking route approaches the center LOS path, especially on route P_3 where the LOS path is blocked all the time.

3.2.3 Doppler Power Spectrum

The maximum Doppler shift is related to the velocity of movement v_m and the signal's center frequency f_c by

$$f_d = \frac{2v_m f_c}{c} \tag{3.3}$$

where c is the speed of light. In an indoor environment, a person walking at 2 m/s may produce a Doppler shift of 20 Hz for a 1.5 GHz center frequency transmission systems. However, this value was not observed in the measurements described here, because the antenna's position are fixed and the only channel variation is generated by the moving scatterers.

The Doppler power spectrum represents the strength of the Doppler shift at various frequencies caused by movements of the terminals or the objects close to them. It is the Fourier transform of the autocorrelation function which defines how the channel impulse response decorrelates over time. Therefore, we may use Fourier analysis to generate the power spectrum of the received signal amplitude, and this power spectrum is the Doppler power spectrum of the channel. Fig. 3.11 and Fig. 3.12 show an example of the measured channel fluctuation waveform and the corresponding Doppler power spectrum.

The width of the Doppler power spectrum is referred to as the Doppler spread B_D of the channel and provides a measure of the fading rate of the channel. It is the range of frequencies μ over which the Doppler power spectrum $S_d(\mu)$ is nonzero. However, for real measurements, $S_d(\mu)$ is never zero, so a threshold at -30 dB is

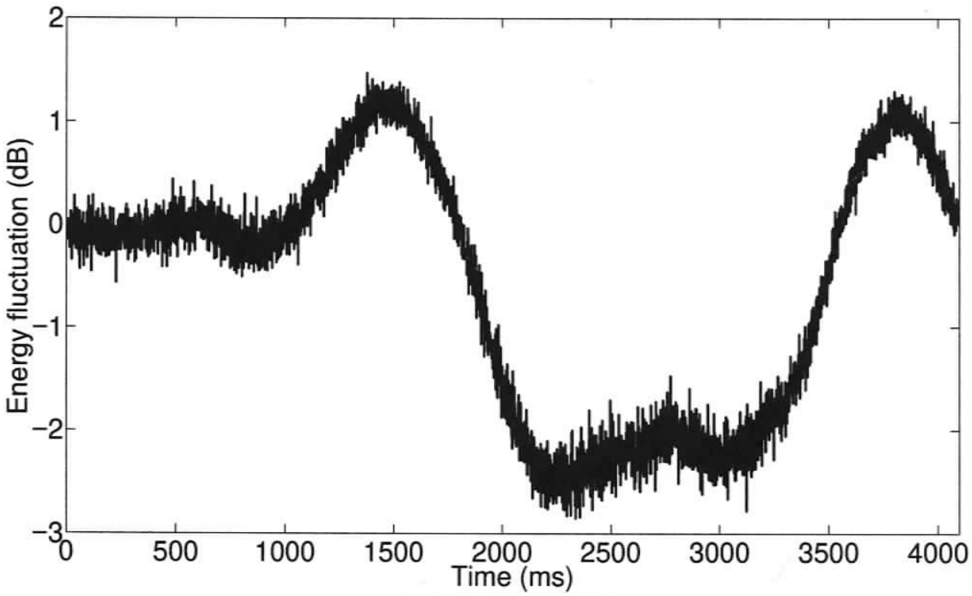

Figure 3.11: Measured channel fluctuation waveform.

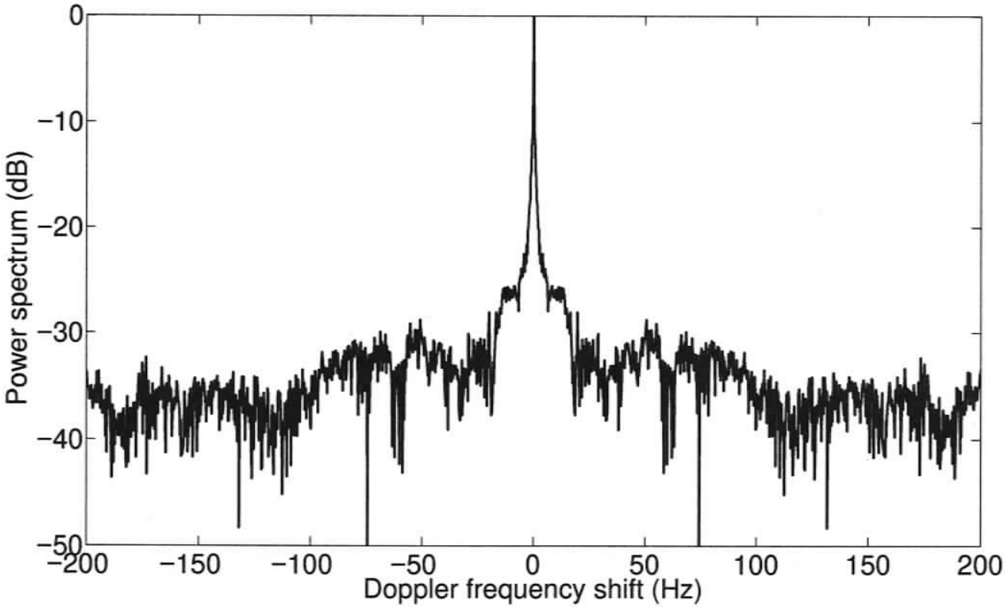

Figure 3.12: The corresponding Doppler power spectrum.

used to determine B_D and to mitigate the effect of noise. In a manner similar to the treatment of delay spread, the second central moment of the Doppler spread function, the RMS Doppler spread, is sometimes used as a measure of the fading rate in a channel, which is given by

$$f_{RMS} = \left[\frac{\int (\mu - \mu_a)^2 \cdot S_d(\mu) \cdot d\mu}{\int S_d(\mu) \cdot d\mu} \right]^{1/2} \tag{3.4}$$

where

$$\mu_a = \frac{\int \mu \cdot S_d(\mu) \cdot d\mu}{\int S_d(\mu) \cdot d\mu}. \tag{3.5}$$

Table 3.1 and Table 3.2 summarize the RMS Doppler bandwidth of all environments. Examined from both Tables, the Doppler spread is no more than 15 Hz, which is fairly small. Due to the Fourier transform relationship between the correlation function and Doppler power spectrum, the Doppler spread B_D is inversely proportional to the channel coherence time T_c, and therefore, a small value of B_D also indicates the high correlation of the UWB temporal variation channel.

3.3 Summary

This chapter presented a comprehensive measurement campaign and analysis of indoor time varying UWB channels. The time domain channel sounding measurements of the dynamic channel induced by moving people have been performed in a variety of environment in a modern office building. A pulse generator which has a 50 ps rise time and 70 ps pulse width was employed to sound the indoor dynamic channels. These experiments were conducted to determine the temporal characteristics of the signal received at a fixed location from a fixed transmitter, and the results are intended for use in the design of fixed indoor UWB systems. First of all, the analysis of the measurement results has revealed that the signal strength attenuation induced by the motion of the people is much smaller than the attenuation in a narrowband system. Hence, in a time varying indoor environment, the narrowband systems are more susceptible to people's motion than the UWB systems. In addition, the analysis of the time correlation coefficient has shown that even if people move in the vicinity of the transceiver, the correlation coefficient remains a very high value, i.e., mostly above 60% compared with the narrowband's below 20%. Finally, a frequency domain analysis of the Doppler spectrum and Doppler spread have been presented. The results of the temporal variation reported in this chapter can be used in the design of the indoor UWB systems, and are especially useful for high data rate UWB communications applications where both Tx and Rx antennas are stationary with people moving around.

Chapter 4

Ultra Wideband Transmitted Reference Pulse Cluster Receiver Prototype Implementation

UWB receivers can generally be categorized into two different types of demodulation schemes: coherent receivers and non-coherent receivers. Coherent scheme needs precise timing synchronization as well as accurate channel estimation, which is quite complex, while non-coherent scheme is much simpler but has to sacrifice performance. Trade-offs must be made in the receiver design in order to balance complexity with performance. Impulse radio UWB systems undergo ample multipath due to the inherent high time resolution. However, to fully take advantage of the multipath components to gain diversity and robustness, a highly complex coherent receiver is needed. Not only stringent synchronization and accurate channel estimation are needed, an ultra-fast analog to digital converter (ADC) and very high performance digital signal processor are required as well.

Alternative receiver structures based on non-coherent techniques have become increasingly popular. Non-coherent receivers are able to recover the energy spread in the multipath channel without requiring channel estimation. One of the existing non-coherent schemes is the delay-hopped transmitted reference (DHTR) system [17]. The receiver correlates the reference pulse with a delayed information bearing pulse to achieve multipath energy without estimating the channel. However, this conventional TR system has two major drawbacks: one is the long delay line which is physically unrealizable, and the other is the 3 dB power loss caused by transmitting non-data-bearing reference pulses.

A new transmitted reference pulse cluster (TRPC) structure is proposed to avoid the implementation constraint of long delay lines that conventional TR systems have to face and can also outperform the conventional TR significantly [38]. Unlike conventional TR, TRPC placed reference pulse and data modulated pulse back to back, which is called a dual pulse. Then several dual pulses are placed together without space between them to compose a pulse cluster. This chapter focuses on the implementation issue of the TRPC receiver.

4.1 Overview of the TRPC scheme

A TR scheme may be implemented by transmitting pairs of identical pulses (called doublets) separated by a time interval T_d, known to both the receiver and the transmitter. The transmitted data is encoded by the relative phase of two pulses. More than one doublet may be associated with each information bit, as long as all the associated doublets have the same time interval T_d between pulses and the same relative polarity of pulses. This would be advantageous if the peak power of the individual pulses at the receiver is near or below the noise floor. In this case, multiple doublets can be integrated to improve the signal-to-noise ratio. The transceiver structure of the TR system is depicted in Fig. 4.1.

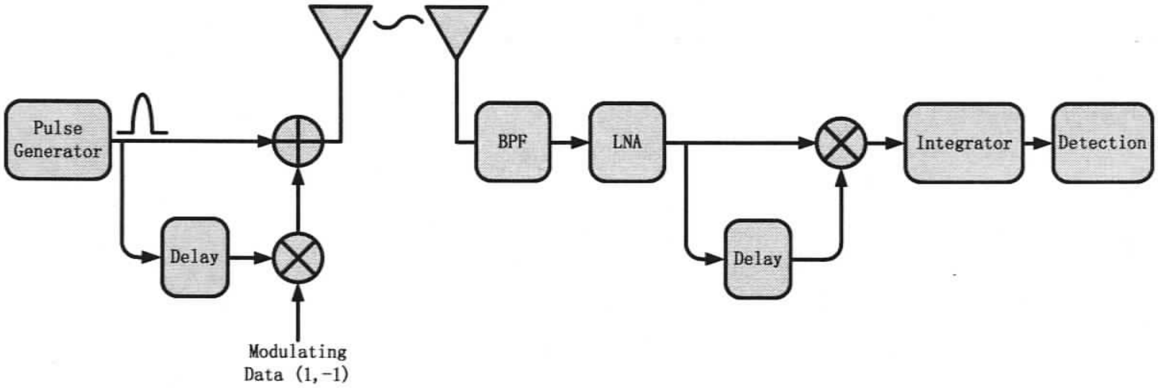

Figure 4.1: The structure of TR transceiver [17].

To meet the implementation constraint posed by conventional TR delay lines and to overcome the 3 dB energy loss due to the transmission of a reference pulse, a new transmitted reference pulse cluster (TRPC) structure where the reference and data pulses are closely packed is proposed. The structure of the pulse cluster is shown in Fig. 4.2 [38].

Mathematically, the TRPC signal is represented by [38]

$$\begin{aligned}\hat{s}(t) &= \sqrt{\frac{E_b}{2N_f}} \sum_{m=-\infty}^{\infty} \sum_{i=0}^{N_f-1} [g(t-mT_s-2iT_d)+b_m g(t-mT_s-(2i+1)T_d)] \\ &= \sqrt{\frac{E_b}{2N_f}} \sum_{m=-\infty}^{\infty} s_{b_m}(t-mT_s) \qquad (4.1)\end{aligned}$$

where E_b is the average energy per bit, N_f is the number of repeated dual pulse pairs in one cluster, $g(t)$ is the composite pulse with duration T_p resulting from the convolution of the transmitter pulse $g_{tr}(t)$ and the receiver filter matched to $g_{tr}(t)$, T_s is the symbol duration determined by the bit rate, $b_m \in \{+1,-1\}$ is the m-th bipolar information bit, and $s_{b_m}(t)=\sum_{i=0}^{N_f-1} g(t-2iT_d)+b_m\sum_{i=0}^{N_f-1} g(t-(2i+1)T_d)$. The delay T_d between the reference pulse and data pulse can be set as short as T_p, or

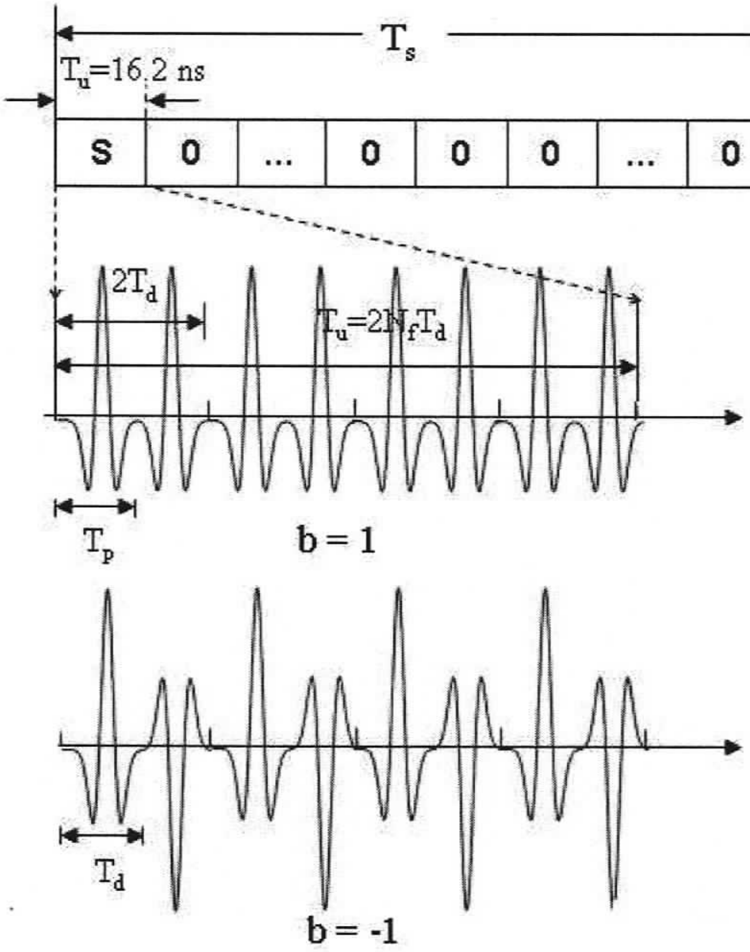

Figure 4.2: The structure of TR pulse cluster [38].

$T_p \leq T_d < 10$ ns.

Unlike the conventional TR that loses 3 dB in signal power due to the transmission of the non-information bearing reference pulse, the reference pulses in TRPC are used with the data pulses in the previous pairs to collect energy for data detection, in addition to the energy collected as in the conventional TR. This is illustrated in Fig. 4.3. In this figure, a "-1" pulse cluster is transmitted, where $N_f = 4$. The solid pulses denote the reference pulses and the dashed pulses denote the data pulses. The energy of each pulse is $E_b/2N_f$. At the receiver, the received signal is autocorrelated with its T_d delayed copy. Assuming an additive white Gaussian noise (AWGN) channel, the overall energy collected for data detection in TRPC is given by [38]

$$E_{\text{TRPC}} = (2N_f - 1) \cdot \frac{E_b}{2N_f} \approx E_b. \tag{4.2}$$

Whereas in the conventional TR system, energy is only collected for the correlation between the data pulses and reference pulses within the pairs, as illustrated by the four blank rectangles in Fig. 4.3. That is [38],

$$E_{\text{conventionalTR}} = N_f \cdot \frac{E_b}{2N_f} = \frac{1}{2}E_b. \tag{4.3}$$

This is one of the reasons that TRPC has superior performance.

Moreover, the TRPC structure has the following additional advantages:

1. ISI free and possible multiple-access

   Given low data rate transmission such as 1 Mbps in 802.15.4a channels, the pulse cluster only occupies a small portion of the symbol duration, so it can minimize the occurrence of ISI. And for the same reason, we can divide symbol duration into multiple time slots for different users.

2. Simple detector

   In the conventional TR system, the correlation between the pulse pairs is carried out frame by frame and then added up. But in the TRPC system, since all the frames are close to each other, the receiver only need to compute one sum.

3. Noise reduction due to short integration interval

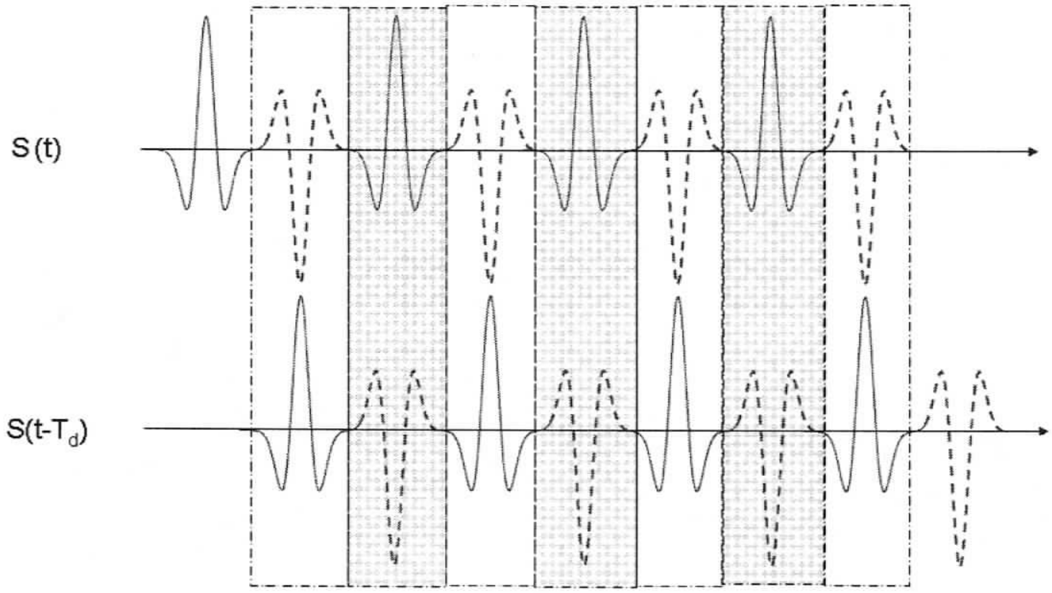

Figure 4.3: Energy collection of the TRPC receiver [38].

The integration length of the autocorrelation detector in TRPC is the cluster width plus the significant channel portion. On the other hand, integration performed in the conventional TR in each frame is over the pulse width plus the significant channel portion, and it is done with several frames. The effective integration length in the conventional TR is much longer than that in TRPC. Due to the short integration interval, the noise component included in the TRPC detection is much smaller, leading to substantial performance improvement over the conventional TR, especially when the system signal-to-noise ratio is not very high.

4.2 TRPC Receiver System Overview

To validate all the advantageous features that TRPC-UWB system can offer, we build a TRPC receiver prototype that can work stably and robustly. Commercial off-the-shelf components are used in our design for simplicity. A data rate from 1 Mbps to 4 Mbps is achieved.

4.2.1 Received Signal Model

Due to UWB spectrum regulations, the transmitted signal is up-converted to the frequency range within 3.1 GHz to 10.6 GHz, in order not to interfere with low frequency wireless services, such as GSM and WiFi. A transmitted I/Q modulated waveform is given by

$$s_T(t) = \hat{s}(t) \cdot \cos(2\pi f_c t) + \hat{s}(t) \cdot \sin(2\pi f_c t) \tag{4.4}$$

where f_c is the carrier frequency. Therefore, the received signal can be written as

$$\begin{aligned} r(t) &= s_T(t) \otimes h(t) + n(t) \\ &= h_L(t) \otimes \hat{s}(t) \cdot \cos(2\pi f_c t) + h_L(t) \otimes \hat{s}(t) \cdot \sin(2\pi f_c t) + n(t) \\ &= g(t) \cdot \cos(2\pi f_c t) + g(t) \cdot \sin(2\pi f_c t) + n(t) \end{aligned} \tag{4.5}$$

where

$$n(t) = n_c(t)\cos(2\pi f_c t) - n_s(t)\sin(2\pi f_c t). \tag{4.6}$$

In which $h_L(t)$ is the equivalent lowpass CIR, $\otimes$ denotes convolution, $g(t) = h_L(t) \otimes \hat{s}(t)$ and $n_c(t)$ and $n_s(t)$ are the inphase and quadrature part of the Gaussian noise $n(t)$ respectively.

The first step of the reception procedure is to down-convert the received signal to base band by mixing with a local oscillating signal. Usually, a phase mismatch exists between the transmitter clock and the receiver clock. Without loss of generality, the phase difference is denoted as θ and is considered in our design. Then the I/Q down-converted signal can be expressed as

$$\begin{aligned} r_I(t) &= r(t) \cdot \cos(2\pi f_c t + \theta) \\ &= [g(t) \cdot \cos(2\pi f_c t) + g(t) \cdot \sin(2\pi f_c t)] \cdot \cos(2\pi f_c t + \theta) + n(t)\cos(2\pi f_c t + \theta) \\ &= \frac{1}{2} g(t) \cdot [\cos\theta - \sin\theta + \cos(4\pi f_c t + \theta) + \sin(4\pi f_c t + \theta)] \\ &+ \frac{1}{2} n_c(t) \cdot [\cos(4\pi f_c t + \theta) + \cos\theta] - \frac{1}{2} n_s(t) \cdot [\sin(4\pi f_c t + \theta) - \sin\theta] \end{aligned} \tag{4.7}$$

$$\begin{aligned}
r_Q(t) &= r(t)\cdot\sin(2\pi f_c t+\theta) \\
&= [g(t)\cdot\cos(2\pi f_c t)+g(t)\cdot\sin(2\pi f_c t)]\cdot\sin(2\pi f_c t+\theta)+n(t)\sin(2\pi f_c t+\theta) \\
&= \frac{1}{2}g(t)\cdot[\cos\theta+\sin\theta-\cos(4\pi f_c t+\theta)+\sin(4\pi f_c t+\theta)] \\
&+ \frac{1}{2}n_c(t)\cdot[\sin(4\pi f_c t+\theta)+\sin\theta]-\frac{1}{2}n_s(t)\cdot[\cos\theta-\cos(4\pi f_c t+\theta)]. \qquad (4.8)
\end{aligned}$$

The I/Q demodulator has internal lowpass filter build in. Therefore, the high frequency components in the above equations are removed, and the lowpass filtered signal can be represented as

$$r_{I_{LPF}}(t)=\frac{1}{2}g(t)(\cos\theta-\sin\theta)+n_I(t) \qquad (4.9)$$

$$r_{Q_{LPF}}(t)=\frac{1}{2}g(t)(\cos\theta+\sin\theta)+n_Q(t) \qquad (4.10)$$

where $n_I(t)=\frac{1}{2}[n_c(t)\cos\theta+n_s(t)\sin\theta]$, and $n_Q(t)=\frac{1}{2}[n_c(t)\sin\theta-n_s(t)\cos\theta]$.

Then, we multiply each of the I and Q output by its delayed copy as every transmitted reference system does. The output signals are given by

$$\begin{aligned}
r_{I_{DM}}(t) &= r_{I_{LPF}}(t)\cdot r_{I_{LPF}}(t-T_d)=\frac{1}{4}g(t)\cdot g(t-T_d)\cdot(1-\sin 2\theta)+n_I(t)\cdot n_I(t-T_d) \\
&+ \frac{1}{2}(\cos\theta-\sin\theta)\cdot[g(t)\cdot n_I(t-T_d)+g(t-T_d)\cdot n_I(t)] \qquad (4.11)
\end{aligned}$$

$$\begin{aligned}
r_{Q_{DM}}(t) &= r_{Q_{LPF}}(t)\cdot r_{Q_{LPF}}(t-T_d)=\frac{1}{4}g(t)\cdot g(t-T_d)\cdot(1+\sin 2\theta)+n_Q(t)\cdot n_Q(t-T_d) \\
&+ \frac{1}{2}(\cos\theta-\sin\theta)\cdot[g(t)\cdot n_Q(t-T_d)+g(t-T_d)\cdot n_Q(t)]. \qquad (4.12)
\end{aligned}$$

Then we combine the I and Q output and get

$$\begin{aligned} r_c(t) &= r_{I_{DM}}(t) + r_{Q_{DM}}(t) \\ &= \frac{1}{2}g(t) \cdot g(t - T_d) + n_I(t) \cdot n_I(t - T_d) + n_Q(t) \cdot n_Q(t - T_d) \\ &+ \frac{1}{2}g(t)(\cos\theta - \sin\theta)n_I(t - T_d) + \frac{1}{2}g(t - T_d)(\cos\theta - \sin\theta)n_I(t) \\ &+ \frac{1}{2}g(t)(\cos\theta - \sin\theta)n_Q(t - T_d) + \frac{1}{2}g(t - T_d)(\cos\theta - \sin\theta)n_Q(t). \end{aligned} \tag{4.13}$$

As seen, the phase difference θ is removed by this procedure without the requirement to explicitly estimate and compensate for θ. This is a non-coherent method. The final step is to integrate $r_c(t)$ to perform an auto-correlation receiving scheme. The decision variable (DV) is given by

$$\begin{aligned} D &= \int r_c(t)dt \\ &= \int \frac{1}{2}g(t) \cdot g(t - T_d)dt + \int [n_I(t) \cdot n_I(t - T_d) + n_Q(t) \cdot n_Q(t - T_d)]dt \\ &+ \int \frac{1}{2}g(t)(\cos\theta - \sin\theta)[n_I(t - T_d) + n_Q(t - T_d)]dt \\ &+ \int \frac{1}{2}g(t - T_d)(\cos\theta - \sin\theta)[n_I(t) + n_Q(t)]dt. \end{aligned} \tag{4.14}$$

and the receiver makes a decision on "+1" if $D > 0$ and "-1" if $D < 0$. To be noted is that the noise product has a mean value of 0. However, the noise variance is enlarged in this non-coherent method to cancel θ, compared to coherently estimating and compensating for θ which has higher complexity.

4.2.2 System Implementation

Although this chapter mainly focuses on the TRPC receiver implementation, it is necessary to explain the transmitter setup for a complete system view. The transmitted pulse cluster is generated by Tektronix AWG7052 arbitrary waveform generator, which is capable of sampling at 5 GSample/s. The waveform generated is shown in Fig. 4.4 ("+1" symbol) and Fig. 4.5 ("−1" symbol). Each single pulse occupies 3 ns, and a cluster of 8 pulses, namely 4 dual pulses make up a symbol.

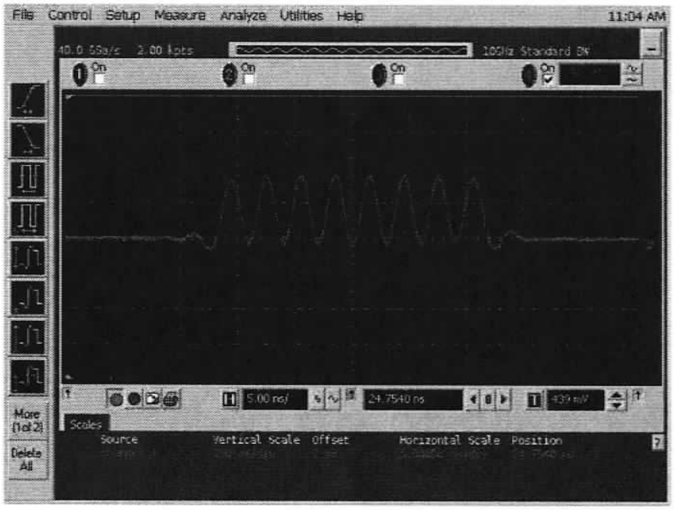

Figure 4.4: The transmitted signal (positive) generated by AWG.

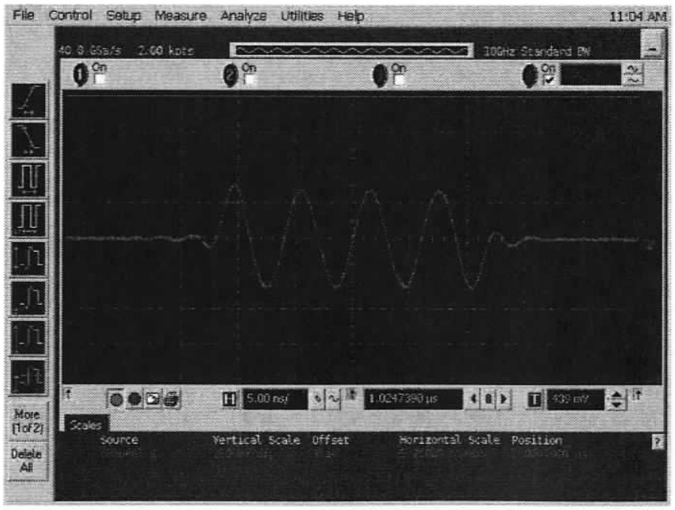

Figure 4.5: The transmitted signal (negative) generated by AWG.

To up-convert the waveform to the regulated UWB spectrum band (3.1 GHz - 10.6 GHz), an Agilent E8267D vector signal generator is used to fulfill the task of I/Q modulation. Finally, the waveform is transmitted by a wideband antenna Electro-Metrics EM-6865.

The block diagram of the TRPC receiver is shown in Fig. 4.6. The front-end amplifier has to have the ability to process the entire bandwidth of the received signal, so good linearity must be achieved throughout the whole bandwidth. In addition, low noise figure is quite important in UWB receiver design due to the low transmission power allowed by regulation. The balance must be handled between the required high gain and low noise figure. A compromise solution is to implement the amplifier in several stages: the first stage is a very low noise figure and low gain amplifier; the subsequent stages can then relax the requirement on noise figure, and high gain can be achieved.

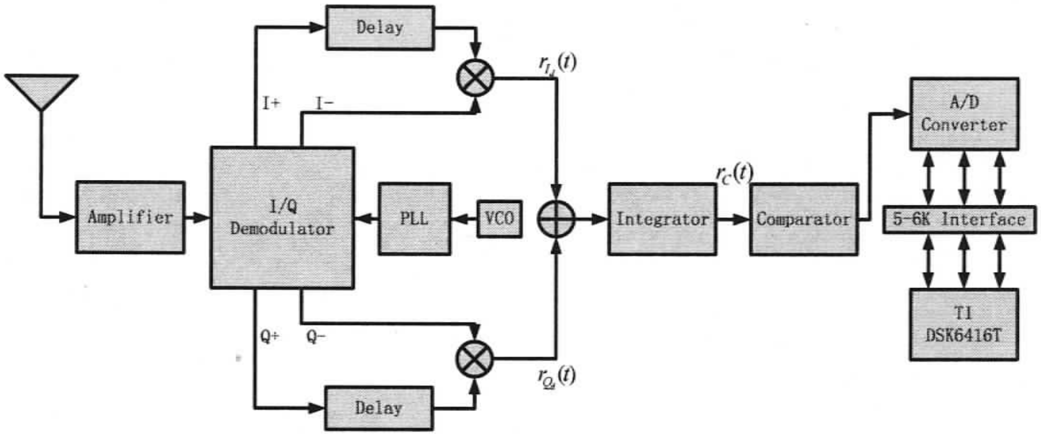

Figure 4.6: The TRPC receiver system block chart.

The I/Q demodulator focuses on two tasks: one is down-conversion and the other is to mitigate the unknown phase mismatch mentioned above. For each of the I and Q channels of the demodulator, there are two outputs, namely positive and negative. The intrinsic nature of a TR receiver is the product of the received signal and its delayed version. We can delay the signal from I-positive and mix it with I-negative, and meanwhile, we delay the signal from Q-positive and mix it with Q-negative. The corresponding signals are given by

$$\begin{aligned} r_{I_d}(t) &= r_I^+(t-T_d) \cdot r_I^-(t) \\ &= -r_{I_{LPF}}(t) \cdot r_{I_{LPF}}(t-T_d) \\ &= -\frac{1}{4}g(t) \cdot g(t-T_d) \cdot (1-\sin 2\theta) - n_I(t) \cdot n_I(t-T_d) \\ &- \frac{1}{2}(\cos\theta - \sin\theta) \cdot [g(t) \cdot n_I(t-T_d) + g(t-T_d) \cdot n_I(t)], and \end{aligned} \tag{4.15}$$

$$\begin{aligned} r_{Q_d}(t) &= r_Q^+(t-T_d) \cdot r_Q^-(t) \\ &= -r_{Q_{LPF}}(t) \cdot r_{Q_{LPF}}(t-T_d) \\ &= -\frac{1}{4}g(t) \cdot g(t-T_d) \cdot (1+\sin 2\theta) - n_Q(t) \cdot n_Q(t-T_d) \\ &- \frac{1}{2}(\cos\theta - \sin\theta) \cdot [g(t) \cdot n_Q(t-T_d) + g(t-T_d) \cdot n_Q(t)]. \end{aligned} \tag{4.16}$$

Afterwards, we combine these two products and integrate over a certain time period. Since we implemented an inverting integrator, the combined signal is given by

$$\begin{aligned} r_C(t) &= -\int (r_{I_d}(t) + r_{Q_d}(t))dt \\ &= \int \frac{1}{2}g(t) \cdot g(t-T_d)dt + \int [n_I(t) \cdot n_I(t-T_d) + n_Q(t) \cdot n_Q(t-T_d)]dt \\ &+ \int \frac{1}{2}g(t)(\cos\theta - \sin\theta)[n_I(t-T_d) + n_Q(t-T_d)]dt \\ &+ \int \frac{1}{2}g(t-T_d)(\cos\theta - \sin\theta)[n_I(t) + n_Q(t)]dt, \end{aligned} \tag{4.17}$$

which is the same as the expression of the DV given by eq. (4.14).

One of the main parts of the TR receiver is the correlator, which correlates the received signal with its delayed copy. The mixer and integrator work together as a correlator.

The most challenging problem of impulse UWB system is the synchronization due to ultra short pulse width and very low duty cycle. One of the widely used method is to sample sufficiently fast, that is, at least 500 Msamples/second. Nevertheless, high sampling rate always comes with low sample resolution, high complexity, high power consumption as well as undue demand on base-band digital signal processor. All of these factors affect the time to market of commercial impulse UWB products. We solve the synchronization problem by using a high speed comparator with programmable hysteresis. As long as the received pulse exceeds a certain threshold, the comparator can output a stable differential positive-referenced emitter-coupled logic (PECL) voltage. In the same way, if the received pulse falls below a certain threshold, the comparator can output an inversed voltage. The internal hysteresis can overcome as much as tens of millivolt noise and interference, and the hysteresis level can be programmed externally.

Finally, the analog front-end's output is simply a square-wave, which can be easily sampled by a low speed analog to digital converter (ADC). Since the symbol rate desired for our TRPC-UWB system is between 1 Mbps to 4 Mbps, a 4 MSPS ADC, Texas Instruments (TI) ADS8422 is employed in our design. The ADC is connected with TI's high performance TMS320C6416T digital signal processor (DSP), which is used to control the ADC and to detect the received symbol in real time.

4.3 Hardware Implementation

The overall system can be separated into 4 parts, which are antenna and amplification, down-conversion, correlation, and detection. The detailed description of each part is shown below.

4.3.1 Antenna and amplification

This part is built with a wideband antenna and a wideband microwave amplifier. A type-N to SMA cable connects the antenna and amplifier together. The antenna we employed in our design is Electro-Metrics EM-6865, which is an omni-directional antenna with vertical polarization and capable of operating as either a transmitting or receiving antenna over the 2 to 18 GHz frequency range. One important thing to be noted is that the polarization of the antenna at both ends of the path must be identical. In a linearly polarized system, a misalignment of polarization of 45 degrees will degrade the signal up to 3 dB and if misaligned 90 degrees the attenuation can be more than 20 dB.

One of the most critical components of the analog front-end is the amplifier, especially for UWB systems. The purpose of the amplifier is to magnify the received signal from the antenna with as little distortion and additional noise as possible. For an applicable UWB amplifier, bandwidth, rise time, noise figure, and gain are the key parameters that should be taken into consideration. The bandwidth of the amplifier should be larger than the bandwidth of the signal to be amplified, otherwise there will be great distortion in the spectrum, resulting in performance degradation. Rise time is a critical parameter for the amplifier, which is defined as the time taken for the output to change from 10% to 90% of its final level when driven by a step input. Apparently, if the rise time of the amplifier is larger than that of the pulse input, it is impossible to deliver an output of amplitude proportional to that of the input value, i.e., the input pulse will be distorted. Therefore, for impulse UWB the selection of the amplifier must meet the rise time requirements. In addition, low noise figure and high gain are always pursued by amplifier manufacturers, but usually cannot be achieved simultaneously. Therefore, a cascade amplifier which is consist of by a set of low noise figure low gain and high gain amplifiers is often employed in practical design.

The amplifier we are using is an Agilent 83017A microwave amplifier, which unfortunately is not a pulse amplifier, but still can work well when a 3 ns width pulse is employed as the input. The 83017A has a passband from 500 MHz to 26.5 GHz, offering a minimum 25 dB gain with maximum noise figure of 8 dB. It features a rise time of 310 ps which is good enough for our implementation.

The waveform captured at the output of the amplifier is shown in Fig. 4.7. It is a I/Q modulated waveform with a carrier of 3.5 GHz, and the sum of I signal and Q signal.

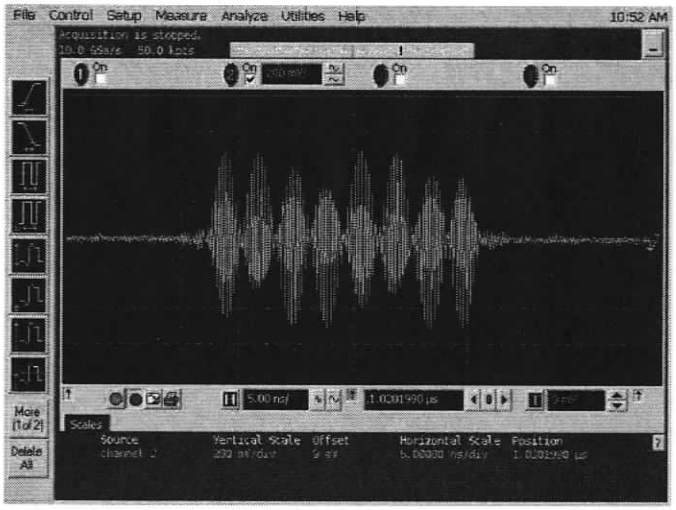

Acquisition is stopped.
10.0 GSa/s 50.0 kpts

Source: channel 2
Vertical Scale: 200 mV/div
Offset: 0 V
Horizontal Scale: 5.00000 ns/div
Position: 1.0201990 µs

Figure 4.7: The waveform captured at the output of the amplifier.

4.3.2 Down-conversion

The major component of the down-conversion part is the I/Q demodulator, which down-converts the input RF signal to baseband I and Q signals. A typical I/Q demodulator diagram is shown in Fig. 4.8. The balun is usually used to convert a single ended signal to a differential signal. The mixer outputs are lowpass filtered to remove the high frequency mixing products.

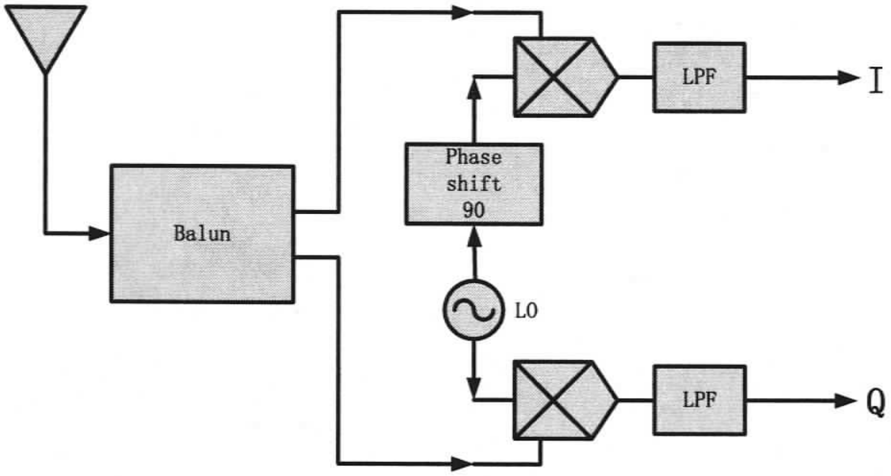

Figure 4.8: The block diagram of I/Q demodulator.

A Hittite HMC597LP4 wideband direct demodulator is used in our design. It is a highly integrated I/Q demodulator that operates of signals from 100 MHz to 4 GHz, with a 15 dB noise figure. The typical application schematic is shown in Fig. 4.9.

As can be seen from Fig. 4.9, a RF signal is fed into the I/Q demodulator through J4. A RF balun allows single ended RF signal to be converted into differential signals which subsequently mixed with a local oscillator (LO) signals. LO signal is generated by a voltage control oscillator (VCO) synthesized by a phase-locked loop (PLL), which will be mentioned later. A dual 45 degree phase shifter splits LO signal into two oscillating signals which have 90 degree phase difference, resulting in in-phase and quadrature outputs. In the end, the down converted I and Q signals are filtered by the low pass filter (LPF) which is realized by a RC circuit.

The stable LO signal is generated by a frequency synthesizer, which is consisted of a PLL, VCO, and LPF. The core of the PLL is a phase/frequency detector (PFD), which compares a feedback frequency with the reference frequency. The PFD's output is filtered and integrated to generate a control voltage that drives an external VCO to

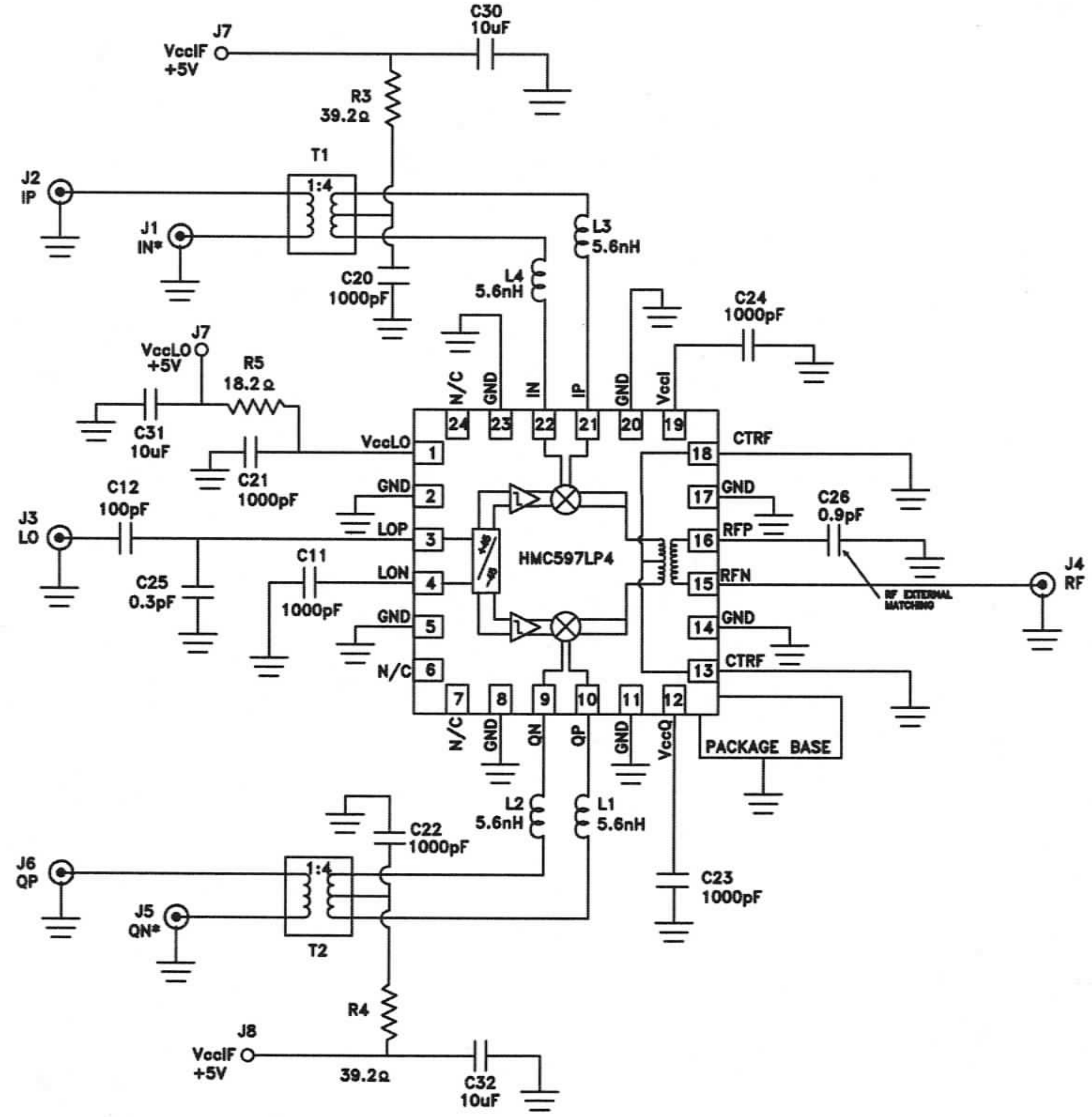

Figure 4.9: HMC597LP4 typical application schematic [39].

increase or decrease the output frequency so as to reduce the PFD's output towards zero. The block diagram of the frequency synthesizer is depicted in Fig. 4.10.

In our design, the frequency synthesizer is built by Analog Device's ADF4108 PLL chip, a well designed three order LPF and a ZX95-3605+ VCO manufactured by Mini-circuit.

The functional block diagram of ADF4108 is shown in Fig. 4.11. A reference

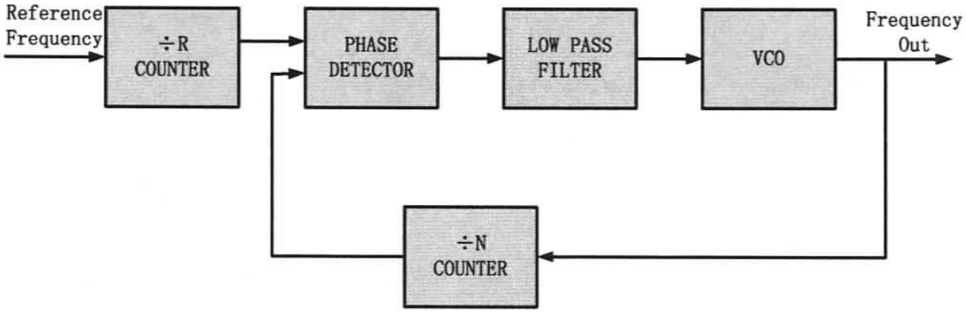

Figure 4.10: Block diagram of the frequency synthesizer.

frequency signal is compared with the signal fed back from the VCO output in the phase frequency detector, resulting in an error signal. This error signal is fed into the charge pump, which output a current that is proportional to the frequency difference between the two inputs when it is in the unlocked state. When the two signal inputs are equal in phase and frequency, the error will be zero and the loop is said to be in a "locked" condition. If we simply look at the error signal, the following equation may be developed. That is [40],

$$e(s) = F_{REF} - \frac{F_0}{N} \tag{4.18}$$

where F_{REF} is the reference frequency, F_0 is the desired output frequency, N is the feedback divider and $e(s)$ is the S transform of the error signal. When

$$e(s) = 0, \tag{4.19}$$

$$F_0 = N \times F_{REF}. \tag{4.20}$$

The output frequency is N times the reference frequency, thus the N counter is determined by the desired output frequency and reference frequency.

From (4.20), the resolution of the output frequency is determined by the reference frequency applied to the phase detector. For example, if 200 KHz spacing is required, then the reference frequency must be 200 KHz. However, getting a stable 200 KHz

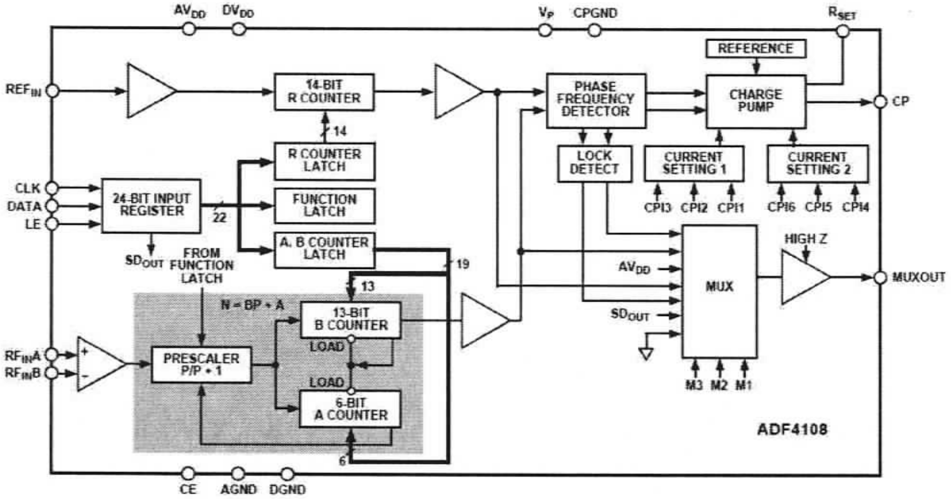

Figure 4.11: Functional block diagram of ADF4108 [41].

frequency source is not easy, since high resolution crystal oscillators always work in the range of 1 MHz to 40 MHz. A sensible approach is to take a good crystal-based high frequency source and divide it down. Thus, for this specified ADF4108 PLL, we use a stable 10 MHz clock signal as a reference, and set the 14-bit R counter to 50, which makes 10 MHz divided by 50 equals 200 KHz.

The signal output from charge pump is current, while the desired tuning signal for VCO is voltage. Therefore, a LPF should be well designed to integrate charge pump current to a tuning voltage. The LPF embedded in the synthesizer is a typical passive three pole loop filter which is always used in low voltage, low operating bandwidth synthesizer applications. The LPF used in our implementation is shown in Fig. 4.12.

4.3.3 Correlation

For a non-coherent TR UWB system, a reference waveform is transmitted before each data-modulated waveform for the purpose of determining the current multipath channel response. Since the reference signal and data signal are transmitted within the

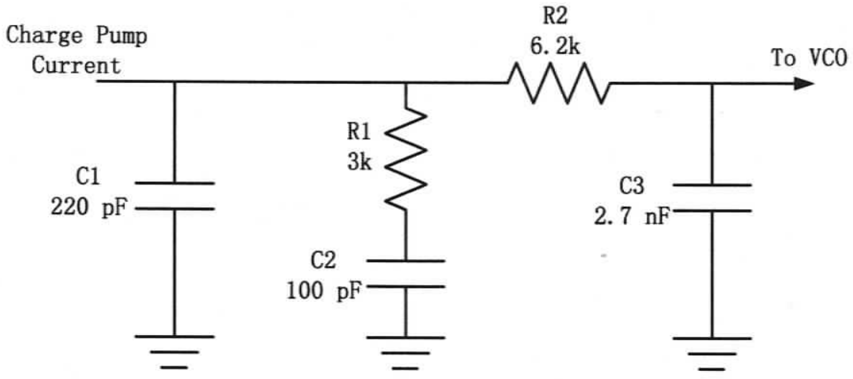

Figure 4.12: Low pass filter configuration.

coherence time of the channel, it is assumed that the channel responses to these two signals are identical. Thus the proposed receiver correlates the data signal with the reference to make use of all the energy of the data signal without requiring additional channel estimation and RAKE reception. The TRPC correlator block diagram is shown in Fig. 4.13.

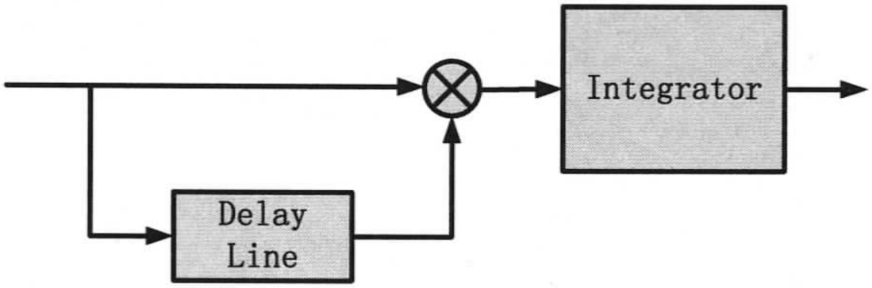

Figure 4.13: TRPC correlator block diagram.

The length of the delay line is a critical issue for those conventional TR-UWB receivers, since the length of the delay line required to generate the symbol level delay can be as long as tens of meters. It is not only bulky, but also extremely difficult to be made accurate for ultra-wideband signals. In TRPC, instead, we only need a pulse width delay time, leading to a 2 foot delay line in length. From our measurements, the electromagnetic wave transmission speed in the Mini-circuit SMA-SMA cable is 2×10^8 m/s, and the delay time is equal to 3 ns pulse width, thus we can easily get the cable length

$$l_{cable} = 2 \times 10^8 \times 3 \times 10^{-9} = 60 \text{ cm} \tag{4.21}$$

The waveform that is delayed and mixed is shown in Fig. 4.14 ("+1") and Fig. 4.15 ("-1"). Clearly, we can see that there are only 7 pulses here, and one pulse is "missing". That is because the original signal and the delayed copy are misaligned by one pulse width, which is generated by the 60 cm delay line.

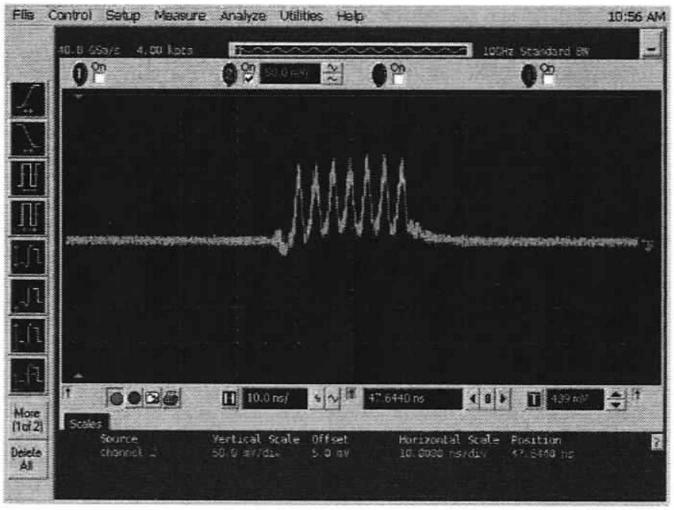

Source: channel 2
Vertical Scale: 50.0 mV/div
Offset: 5.0 mV
Horizontal Scale: 10.0000 ns/div
Position: 47.6440 ns

Figure 4.14: Delayed and mixed signal (positive).

The Op-amp is probably the most widely used components, and integrator is one of the typical Op-amp applications. Due to the ultra short pulse width of the UWB signal, a very fast and wide band Op-amp is needed. Fortunately, National Semiconductor's LMH6702 wideband Op-amp can meet our design specification very well. The integrator is shown in Fig. 4.16 and performs the mathematical operation of integration. This circuit is essentially a low-pass filter with a frequency response decreasing at 6 dB per octave (20 dB per decade).

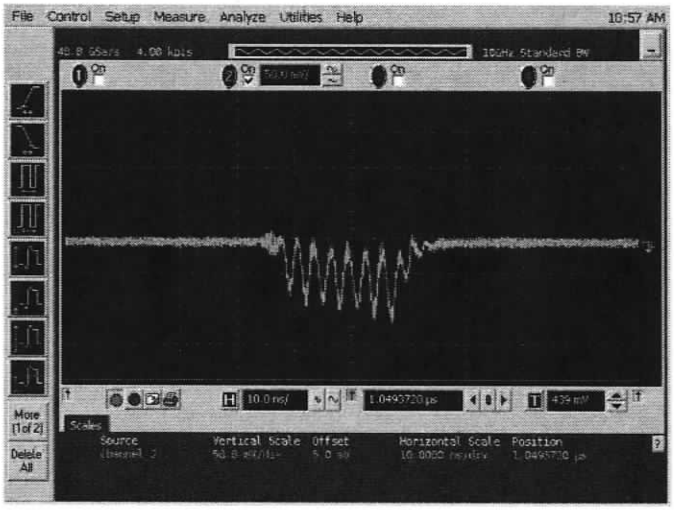

Source Channel 2
Vertical Scale 50.0 mV/div
Offset 5.0 mV
Horizontal Scale 10.0000 ns/div
Position 1.0493720 µs

Figure 4.15: Delayed and mixed signal (negative).

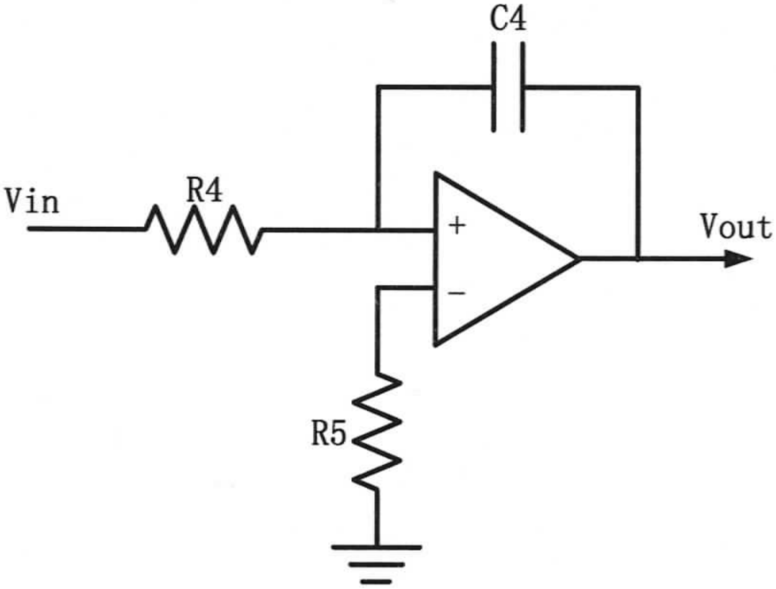

Figure 4.16: The integrator schematic.

The output of the integrator can be written as

$$V_{out} = \frac{1}{R_4 C_4} \int_{t_1}^{t_2} V_{in}(t)dt = \frac{1}{\tau} \int_{t_1}^{t_2} V_{in}(t)dt \tag{4.22}$$

where $\tau = R_4C_4$ is called time constant, which determines how fast the integrator integrates. Care should be taken on the selection of τ. Because the LMH6702 op-amp's maximum output is limited to 5 volts, if τ is too small, the op-amp output will saturate quickly before it integrates to time t_2, resulting in a highly distorted output waveform. So τ must satisfy this equation

$$\tau \geq | - \frac{1}{U_{omax}} \int_0^T U_{in}(t)dt| \tag{4.23}$$

where U_{omax} is the maximum output of the op-amp, and $U_{in}(t)$ is the input signal. In addition, R_5 must equal to R_4 for minimum error due to bias current.

Some computation should be made on the selection of R_4, R_5 and C_4. Integration time for our design is around 50 ns, which covers the whole cluster pulses and the majority of the resolvable multipaths. Suppose the input voltage is around 100 mV and let $R_4 = R_5 = 100\ \Omega$. Then we have

$$\tau = | - \frac{1}{U_{omax}} \int_0^T U_{in}(t)dt| = | - \frac{1}{5} \int_0^{50\times 10^{-9}} 0.1dt| = 10 \times 10^{-10} \tag{4.24}$$

$$C_4 = \frac{\tau}{R_4} = \frac{10 \times 10^{-10}}{100} = 10 \text{ pF}. \tag{4.25}$$

The waveform after integration is shown in Fig. 4.17. A cluster of seven pulses are integrated together in order to accumulate more power. Due to the character of low duty cycle, there is nothing but noise after the pulse cluster. So after the integration of the seven pulses, the integrator output reaches its peak, and then the capacitor C_4 begin to discharge, resulting in a drop of the output signal.

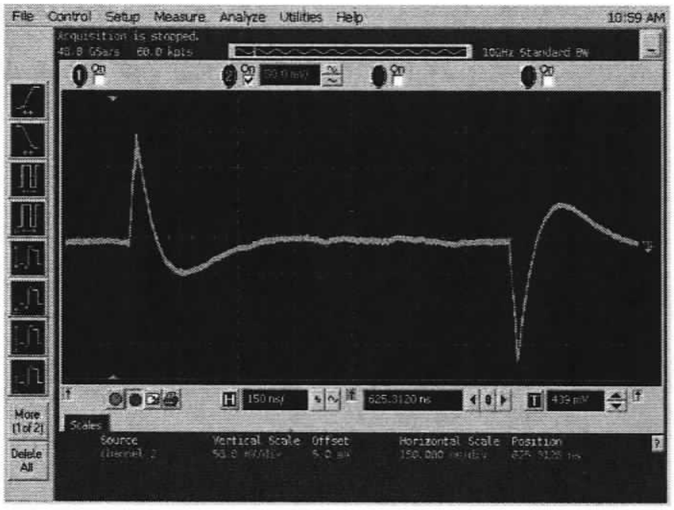

Figure 4.17: The signal after integration.

4.3.4 Detection

Outputs from the correlator are still pulse like waveforms, although the pulse width is larger than the transmitted 3 ns pulse, the duty cycle is still relatively low (about 5%). Therefore, how to determine the sampling time of the integrator output is still a big issue. As mentioned before, a comparator is used here to convert low duty cycle waveform to full duty cycle waveform in order to ease the sampling timing requirement.

The comparator used is Analog Device's high speed comparator ADCMP564, which features only 700 ps propagation delay and up to 1.5 GHz bandwidth. Moreover, an internal programmable hysteresis is a very useful element. The addition of hysteresis to a comparator is often used in a noisy environment. The transfer function for a comparator with hysteresis is shown in Fig. 4.18. Hysteresis is the difference in the threshold levels when the comparator turns on and off. A small amount of hysteresis added to the comparator reduces noise sensitivity of the comparator and helps the comparator to avoid oscillation. If the input voltage approaches the threshold from the negative direction, the comparator switches from 0 to 1 when the input crosses $+V_H/2$. The new switching threshold then becomes $-V_H/2$. The comparator remains in "1" state until the threshold $-V_H/2$ is crossed while coming from the positive direction. In this way, noise centered around 0 Volts does not cause the comparator to switch states unless it exceeds the region bounded by $\pm V_H/2$.

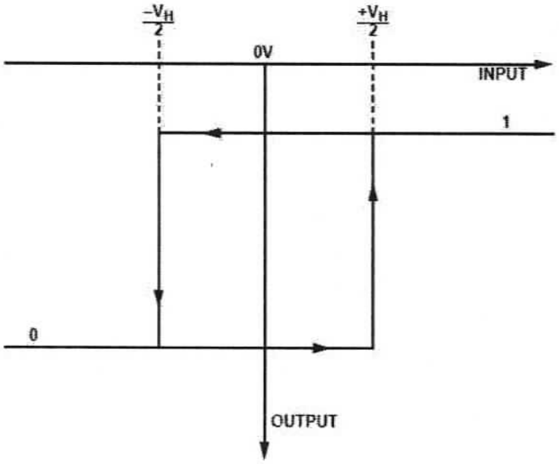

Figure 4.18: Comparator hysteresis transfer function.

The hysteresis range can be changed easily by adding a potentiometer between HYS pin and ground, which creates a current into the chip to generate hysteresis. Hysteresis generated in this manner is independent of output swing and is symmetrical around the trip point, which outperforms the hysteresis introduced by using positive feedback from the output back to the input. The hysteresis vs. resistance curve is shown in Fig. 4.19.

As long as the input pulse can exceed the threshold and the noise is below the threshold, a nice square wave is generated by the comparator, as shown in Fig. 4.20 and Fig. 4.21.

The last step is to convert analog signal to digital signal for post digital signal

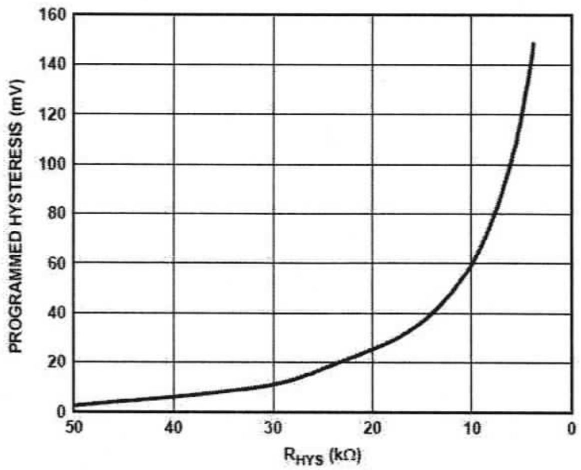

Figure 4.19: Comparator hysteresis vs. resistance [42].

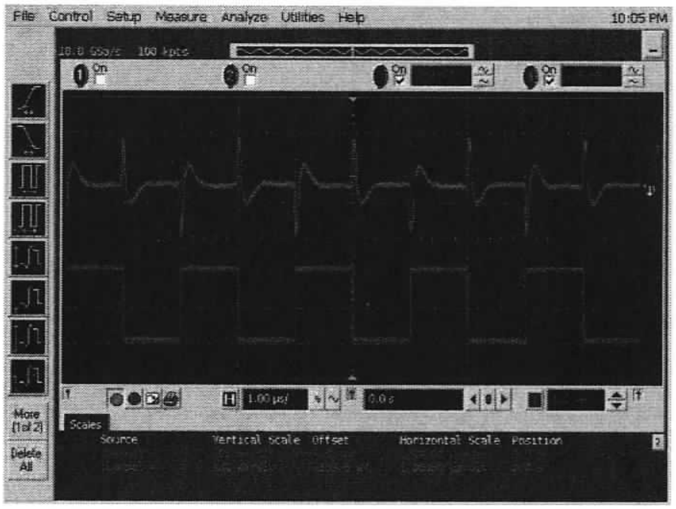

Figure 4.20: Input (pink) and output (purple) of the comparator ADCMP564 (through cable transmission).

processing, and the Texas Instruments' ADS8422 ADC fulfills this task. ADS8422 is a 16bit, 4MSPS, fully differential input ADC. The sample speed of the ADC can be controlled by a micro-controller, and this role is played by Texas Instruments' DSP TMS320C6416. The 5-6K interface board is used here to connect ADS8422 to

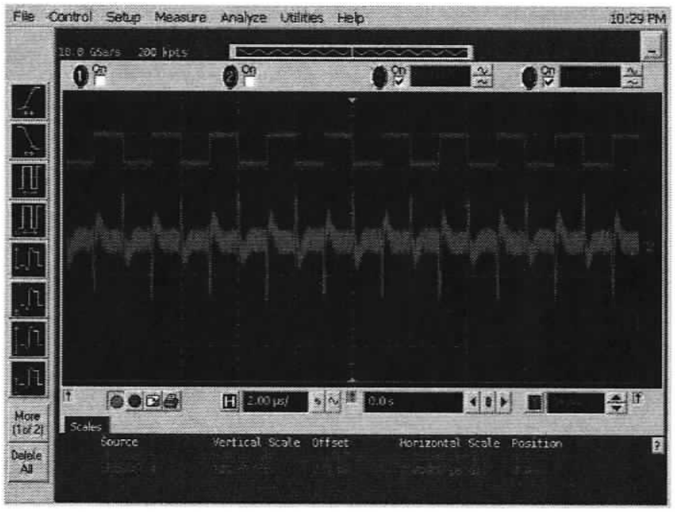

Figure 4.21: Input (pink) and output (purple) of the comparator ADCMP564 (through wireless channel transmission).

TMS320C6416 starter kits. The overall system is shown in Fig. 4.22 and Fig. 4.23 and the key components used are listed in Table 4.1.

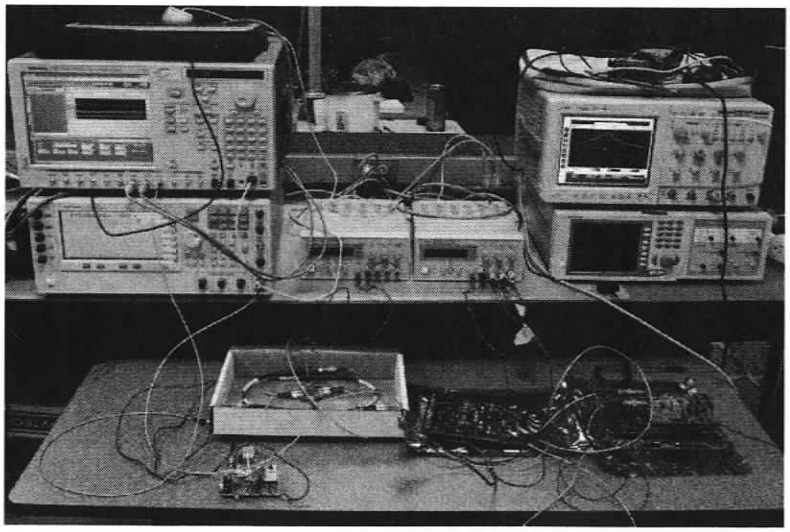

Figure 4.22: The overall system implementation.

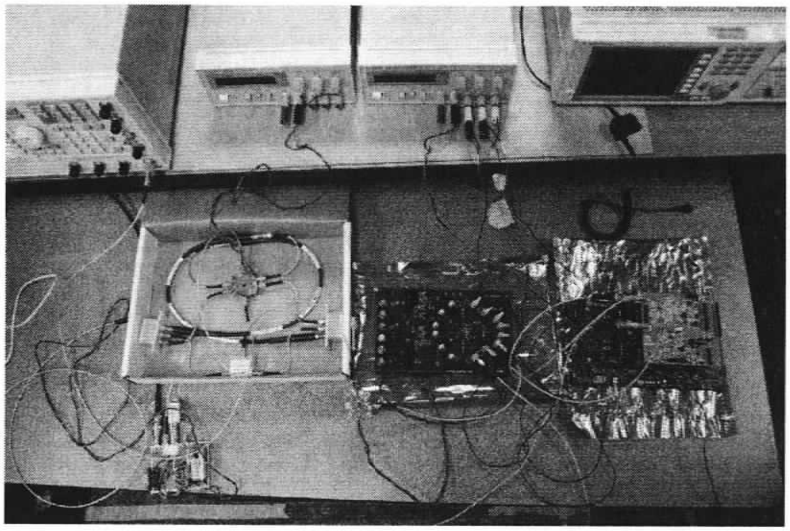

Figure 4.23: The overall system implementation.

Table 4.1: The list of the key components used

Component	Model	Manufacturer	Description
Antenna	EM-6865	Electro-Metrics	Omni-Directional Wideband Antenna (2-18 GHz)
Amplifier	83017A	Agilent	Microwave System Amplifier (0.5-26.5 GHz)
I/Q demodulator	HMC597LP4	Hittite	Direct conversion I/Q Demodulator (100-4000 MHz)
PLL	ADF4108	Analog Device	Frequency synthesizer
VCO	ZX 95-3605-S+	Mini-circuit	Linear tuning VCO (3300-3605 MHz)
Delay line	CBL-1.5FT-SMSM+	Mini-circuit	1.5 feet test cable (DC-18 GHz)
Mixer	ZLW-1W	Mini-circuit	Wideband frequency mixer (1-750 MHz)
Combiner	ZFSC-2-10G+	Mini-circuit	Wideband power splitter / Combiner
Operational Amplifier	LMH6702	National Semiconductor	Very wideband operational amplifier
DSO	81004A	Agilent	Oscilloscopes with 10 GHz bandwidth and 40 GS/s sample rate
VSG	E8267D	Agilent	Vector signal generator with I/Q modulation up to 44 GHz
AWG	AWG7052	Tektronix	Arbitrary waveform generator with sample rates of 5 GS/s

Table 4.2: The BER performance of the TRPC prototype

VSG output power	Number of errors out of 10^5 bits	BER
11 dBm	45755	45.755%
12 dBm	34876	34.876%
13 dBm	12959	12.959%
14 dBm	125	0.125%
15 dBm	7	0.007%
16 dBm	3	0.003%

To evaluate the performance of the TRPC prototype, we performed the test by setting the spacing of the Tx and Rx antenna to be 3 meters. The results are shown in 4.2, where the first column denotes the output power of the VSG (note the values are output power not SNR) and the third column is the corresponding BER. In order to estimate the SNR of the received signal, we employed the free space path loss model, which is given by [43]

$$P_t = P_r \left[\frac{4\pi d}{\sqrt{G_l}\lambda} \right]^2 \tag{4.26}$$

where P_t and P_r are the transmit power and receive power respectively, d is the spacing distance between Tx and Rx antenna, λ is the wavelength of the transmitted signal, and $\sqrt{G_l}$ is the product of the transmit and receive antenna field radiation patterns in the LOS direction. For nondirectional antenna, $G_l = 1$. To compute the SNR, we can derive the received signal power from the free space path loss model, and noise power from measurements. Finally, the BER vs. SNR curve is plotted in Fig. 4.24.

4.4 Summary

This chapter presents the detailed description of the implementation of the TRPC receiver. The commercial off-the-shelf components are used to build the prototype.

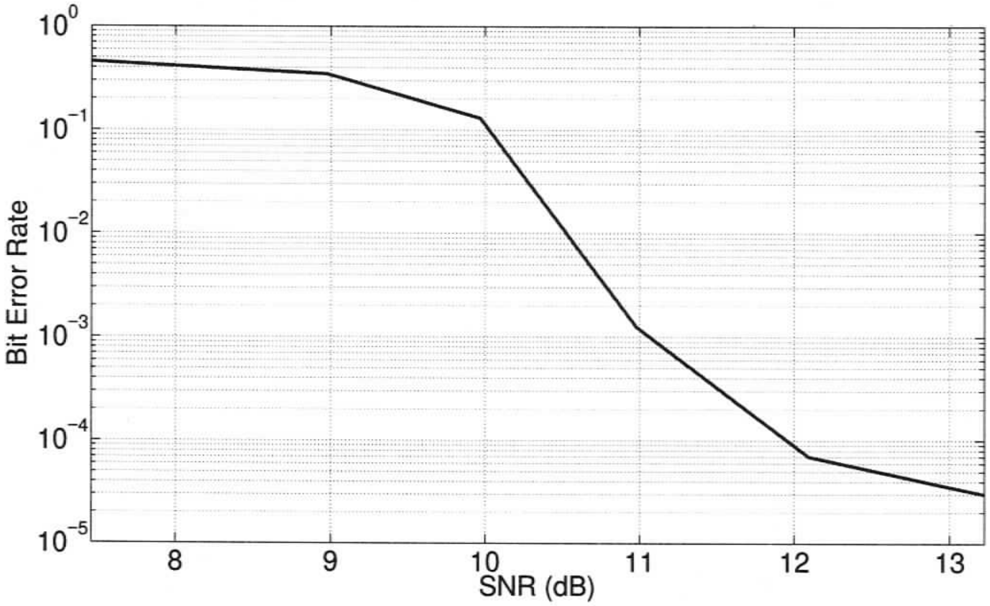

Figure 4.24: The BER performance of the TRPC prototype.

The four main parts of the system are antenna and amplification, down-conversion, correlation, and detection, are described in details. The components used to build each part of the system are carefully selected to meet the stringent requirement of the UWB system. The overall system works stably and robustly and this was verified through testing.

Chapter 5

Conclusions and Future Work

5.1 Conclusions

The UWB propagation channel can have a significant impact on system design and performance evaluation. Due to the ultra wide bandwidth, the ultra-short pulses traveling along different paths arrive at the Rx almost without overlapping. This property is much different from conventional narrow band wireless channels, thus much effort is required to fully develop an accurate UWB channel propagation model. In this thesis, several important aspects of the UWB indoor channel are investigated, including channel reciprocity, spatial characteristics, body shadow effect and the time variations of the channel. The study of these properties provides useful information for the receiver designs in terms of link budget estimation, receiver structure selection and performance evaluation. An implementation of the TRPC receiver prototype is also given in this thesis. It provides data rates from 1 Mbps to 4 Mbps, and is demonstrated to work stably and robustly.

In Chapter 2, comprehensive time domain measurements are performed to investigate the properties of channel reciprocity, spatial characteristics and body shadow effect. For reciprocity measurement, the center frequency of the UWB signal is shifted from 4 GHz to 8 GHz and the distance from 2 meters to 9 meters, the results show that the UWB channel reciprocity is distance independent and frequency independent. The study of the spatial characteristic shows the spatial correlation drops fast and monotonically within a small area centered at the reference point with a radius of one wavelength. In addition, one wavelength spacing between the MIMO antenna element can achieve a relatively low correlation (50%) and a small array size. The investigation of the body shadow effect points out that the body shadow faing for UWB systems is relatively low compared to the narrow band systems, and the shadowing statistics can be modeled by the Gaussian distribution. Moreover, the RMS delay spread is influenced by the body shadow effect as well, although the change is not large.

The temporal variation of the indoor UWB propagation channel is investigated in Chapter 3. Pulse based time domain measurements were carried out within the range of 3 GHz to 7 GHz band and the measurement campaign was conducted in diversified environments in a modern office building, consisting of office, hallway and cafeteria scenarios. Signal strength fluctuation, time correlation coefficients and Doppler spread are derived from the analysis of the measured data. The results reveal that the signal strength attenuation induced by the motion of people ranges within 5 dB, which is much smaller than is observed in a narrowband systems. Moreover, the analysis of the time correlation coefficients has shown that even when people moves in the vicinity of the transceiver, the correlation coefficients remains a relatively high value, i.e., mostly above 50% compared with the narrowband's below 20%.

Chapter 4 has described the details of the UWB TRPC receiver implementation. Commercial off-the-shelf components are used to implement the prototype of the TRPC receiver. A throughput of 1 Mbps to 4 Mbps can be achieved in an indoor environment.

5.2 Future Work

1. The measurement results in this thesis did not perform a deconvolution. On one hand, this greatly simplifies the data evaluation. However, on the other hand, the antenna effect on the channel can not be separated. Thus, the channel transfer function is the combination of the channel impulse response and the antenna transfer function, which depends on the specific antenna being used. One way to separate the antenna effect is to use the double directional channel model, in which angle of arrival (AOA) and angle of departure (AOD) are considered. Thus, it is worthwhile to use the deconvolution method in order to achieve a more accurate channel expression.
2. The spatial correlation can be affected by many parameters, such as AOA, antenna spatial structure, antenna mutual coupling and near field scatters. Design of systems with low spatial correlation requires a full investigation of the underlying parameters that strengthen spatial correlation. Among all these parameters, the AOA plays a decisive role in the spatial correlation, thus, it is of great importance to study the distribution of the AOA and its impact on the spatial correlation.
3. A complete communication system contains transmitter as well as the receiver. Although the prototype of the TRPC receiver has been implemented, much more effort should be addressed to improve the performance of the receiver, and to build a corresponding TRPC transmitter. The challenging part of the TRPC transmitter is the generation of a cluster of ultra narrow pulses, thus, further work should focus on this.

Bibliography

[1] L. M. M. Ghavami and R. Kohno, *Ultra Wideband Signals and Systems in Communication Engineering.* John Wiley and Sons, 2004.

[2] "First report and order: in the matter of revision of part 15 of the commission's rules regarding ultra-wideband transmission systems," Tech. Rep. 02-48, FCC, April 2002.

[3] "Devices using ultra-wideband (uwb)technology," Tech. Rep. RSS-220, Spectrum Management and Telecommunications, March 2009.

[4] E. O. W. M. A. B. B. Allen, M. Dohler and D. Edwards, *Ultra-wideband antennas and propogation for communications, radar and imaging.* West Sussex, England: John Wiley and Sons, 2007.

[5] A.F.Molisch, *Wireless communications.* John Wiley and Sons, 2005.

[6] "Ieee 802.15.4a channel model - final report," Tech. Rep. IEEE 802.15-04-0662-02-004a, A.F.Molisch et al., 2005.

[7] M. Win and R. Scholtz, "Characterization of ultra-wide bandwidth wireless indoor channels: A communication-theoretic view," *IEEE J. Selected Areas in Communications*, pp. 1613–1627, 12.

[8] D. M. B.M. Donlan and R. Buehrer, "The uwb indoor channel: large and small scale modeling," *IEEE Trans. Communications*, pp. 1786–1796, 10.

[9] W. R. W. T. S.S. Ghassemzadeh, R. Jana and V. Tarokh, "Measurement and modeling of an ultra-wid bandwidth indoor channel," *IEEE Trans. Communications*, pp. 2863–2873, 10.

[10] A. Molisch, "Ultrawideband propagation channels-theory, measurement, and modeling," *IEEE Trans. Vehicular Technology*, pp. 1528–1545, 9.

[11] "Wpan high rate alternative phy," Tech. Rep. www.ieee802.org/15/pub/TG3a.html, IEEE 802.15.3a Task Group.

[12] "Wpan high rate alternative phy," Tech. Rep. www.ieee802.org/15/pub/TG4a.html, IEEE 802.15.4a Task Group.

[13] R. Qiu and I. Lu, "Multipath resolving with frequency dependence for broadband wireless channel modeling," *IEEE Trans. Vehicular Technology*, pp. 273–285, 1.

[14] A. Salch and R. Valenzuela, "A statistical model for indoor multipath propagation," *IEEE J. Selected Areas in Communications*, vol. 5, pp. 128–137, Feb. 1987.

[15] Z. C. H. Arslan and M. Benedetto, *Ultra Wideband Wireless Communication.* John Wiley and Sons, 2006.

[16] M. B. H. Arslan, Z.N. Chen, *Ultra-wideband wireless communication.* New Jersey: John Wiley and Sons, 2006.

[17] R. Hoctor and H. Tomlinson, "Delay-hopped transmitted-reference rf communications," in *Proc. IEEE Conference on Ultra-wideband System and Technology (UWBST)*, pp. 265–269, May 2002.

[18] P. R. A. Derode and M. Fink, "Acoustic time-reversal through high-order multiple scattering," *IEEE Ultrasonics Symposium*, pp. 1091–1094.

[19] I. A. Khaleghi, G. El Zein, "Demonstration of time-reversal in indoor ultra-wideband communications: Time domain measurement," in *International Symposium on Wireless Communication Systems*, pp. 165–468, Oct 2007.

[20] W. Malik and D. Edwards, "Measured mimo capacity and diversity gain with spatial and polar arrays in ultrawideband channels," *IEEE Trans. Communications*, pp. 2361–2370, Dec.

[21] L. Zheng, "Diversity and multiplexing: a fundamental tradeoff in multiple-antenna channels," *IEEE Trans. Information Theory*, pp. 1073–1096, May.

[22] R. LaMaire and M. Zorzi, "Effect of correlation in diversity systems with rayleigh fading, shadowing, and power capture," *IEEE J. Selected Areas in Communications*, pp. 449–460, Apr.

[23] C. Oestges and B. Clerckx, *MIMO Wireless Communications.* Academic Press, 2007.

[24] W. Malik, "Spatial correlation in ultrawideband channels," *IEEE Trans. Wireless Communications*, pp. 604–610, Feb.

[25] H. Agus, J. Nielsen, and R. Davies, "Correlation analysis for indoor UWB channel," in *Proc. Wireless*, pp. 102–110, 2005.

[26] R. Ganesh and K. Pahlavan, "Statistics of short time and spatial variations measured inwideband indoor radio channels," *IEE Proceedings-H Microwaves, Antennas and Propagation*, pp. 297–302, Aug.

[27] Y. Shang, D. Wang, and D. Birru, "Performance Analysis of WiMedia UWB System for Medical Applications with Human Blockage," in *Computer Communications and Networks, 2008. ICCCN'08. Proceedings of 17th International Conference on*, pp. 1–5, 2008.

[28] A. Pradabphon, N. Kaewboonruean, M. Chamchoy, P. Supanakoon, and S. Promwong, "Experimental evaluation scheme of UWB propagation channel with human body," in *IEEE International Symposium on Communications and Information Technology, 2005. ISCIT 2005*, vol. 1, 2005.

[29] H. Hashemi, "A study of temporal and spatial variations of the indoor radio propagation channel," in *IEEE International Symposium on Personal, Indoor and Mobile Radio Communications*, pp. 127–134, Sept 1994.

[30] L. Talbi, "Human disturbance of indoor ehf wireless channel," in *Electronic Letters*, pp. 1361–1363, Oct 2001.

[31] S. M. R.J.C. Bultitude and W. Sulliva, "A comparison of indoor radio propagation characteristics at 910 mhz and 1.75 ghz," *IEEE J. Selected Areas in Communications*, pp. 20–30, Jan.

[32] R. Ganesh and K. Pahlavan, "Statistics of short time variations of indoor radio propagation," in *Proc. IEEE International Conference on Communications (ICC)*, pp. 1–5, June 1991.

[33] G. D. P. Marinier and C. Despins, "Influence of human motion on indoor wireless millimeter-wave channel characteristics," in *Proc. IEEE Vehicular Technology Conference (VTC)*, pp. 979–983, May 1997.

[34] P. Pagani and P. Pajusco, "Characterization and modeling of temporal variation on an ultrawideband radio link," in *IEEE Trans. Antennas and Propagation*, pp. 3198–3206, Nov 2006.

[35] P. Pagani and P. Pajusco, "Modeling the space and time variant ultra-wideband propagation channel," in *IEEE Conf. Ultra-Wideband*, pp. 201–206, Sept 2006.

[36] P. Pagani and P. Pajusco, "Experimental assessment of the uwb channel variability in a dynamic indoor environment," in *IEEE International Symposium on Personal, Indoor and Mobile Radio Communications*, pp. 2973–2977, Sept 2004.

[37] R. Ganesh and K. Pahlavan, "Statistics of short time and spatial variations measured inwideband indoor radio channels," in *IEE Proceedings H Microwaves, Antennas and Propagation*, vol. 140, pp. 297–302, 1993.

[38] X. Dong, L. Jin, and P. Orlik, "A New Transmitted Reference Pulse Cluster System for UWB Communications," *IEEE Transactions on Vehicular Technology*, vol. 57, no. 5, pp. 3217–3224, 2008.

[39] "Hmc597lp4 - sige wideband direct demodulator smt data sheet," Tech. Rep. www.hittite.com/content/documents/data_sheet/hmc597lp4.pdf, Hittite Microwave Corporation.

[40] "Phase locked loops for high frequency receivers and transmitters," Tech. Rep. Analog Dialogue Volume 33, Mike Curtin and Paul OBrien, 1999.

[41] "Adf4108 - pll frequency synthesizer data sheet," Tech. Rep. http://www.analog.com/static/imported-files/Data_Sheets/ADF4108.pdf, Analog Devices.

[42] "Adcmp564 - dual high speed ecl comparator data sheet," Tech. Rep. http://www.analog.com/static/imported-files/data_sheets/ADCMP563_564.pdf, Analog Devices.

[43] D. Parsons, *The Mobile Radio Propagation Channel.* Halsted Press, 1992.